A Study of the Semiconductor and Thermoelectric Properties of Sputtered Mixed Metal-Oxide Thin Films

by

Matthew G. McDowell

Submitted in partial fulfilment of the requirements
for the degree of Doctor of Philosophy

at

Dalhousie University
Halifax, Nova Scotia
June 2014

© Copyright Matthew G. McDowell, 2014

Table of Contents

List of Tables viii

List of Figures x

Abstract xviii

List of Abbreviations and Symbols Used xix

Acknowledgements xxiii

Chapter 1 Introduction 1

1.1 Semiconductor Background 1

1.2 Mixed Oxide Semiconductors 1

1.3 Thermoelectric Background 3

1.4 Mixed Oxide Thermoelectric Properties 5

1.5 Goals 6

Chapter 2 Theory 7

2.1 Field Effect Transistors 7

2.1.1 Field Effect Transistor Operation 7

2.1.2 Field Effect Mobility 8

2.1.3 Threshold Voltage, Sub-threshold Swing, On/Off Ratio 9

2.2 The Thermoelectric Figure of Merit 11

2.3 Electrical Conductivity 12

2.3.1 Sheet Resistance 13

2.3.2 van der Pauw Measurements 14

2.3.3 Hall Effect Mobility 17

2.3.4 Charge Carrier Density 19
2.4 Thermal Conductivity 20
2.4.1 The 3ω Method 20
2.4.2 Analysis of 3ω Data 23
2.4.3 Thermal Penetration Depth 25
2.4.4 Interfacial Thermal Resistance 26
2.5 The Seebeck Effect 26
2.6 Origin of the Thermoelectric Figure of Merit 27
2.7 The Wiedemann-Franz Law 31

Chapter 3 Sample Fabrication **32**

3.1 RF Sputtering 32
3.1.1 Theory 32
3.1.2 Sputtering Conditions Used 33
3.1.3 Deposition of Combinatorial Films 33
3.1.4 Stencil Masks 34
3.2 Annealing 36
3.3 Photolithography 37
3.3.1 Etching the Films 37
3.3.2 Lift-off Patterning of Metal 38
3.4 Deposition of Insulating and Metal Films 39
3.4.1 Al_2O_3 Films 39
3.4.2 Nickel Adhesion 40
3.4.3 Aluminum 41

Chapter 4 Physical Characterization **42**

4.1 Film Thickness 42
4.1.1 Profilometry 42
4.1.2 Ellipsometry 43

4.2 Film Stoichiometry 44
4.2.1 Electron Microprobe 45
4.2.2 Mass Disks 46
4.3 Film Structure 47
4.3.1 X-ray Diffraction 47

Chapter 5 Electrical and Thermal Characterization 49
5.1 Field Effect Transistors 49
5.1.1 Transistor Design 49
5.1.2 I-V Measurements 50
5.1.3 Noise Reduction and Light Sensitivity 51
5.2 Automated Thermal Conductivity Measurements 51
5.2.1 Photomask Design 52
5.2.2 Unintentional Joule-Heating 52
5.2.3 Enclosure and PCB 54
5.2.4 Switch Matrix 55
5.2.5 Lock-In Amplifier 55
5.2.6 AC Current Measurements 57
5.2.7 Temperature Coefficient of Resistance 58
5.2.8 3ω Measurement Process 59
5.3 Automated van der Pauw Measurements 59
5.3.1 Switch Matrix 60
5.3.2 4-wire Resistance Measurements 60
5.3.3 Manual Measurement for Very High Resistance 61
5.4 Manual Hall Effect Measurements 61
5.5 Seebeck Coefficient 62
5.5.1 Sample Preparation 62
5.5.2 Measurement of the Seebeck Coefficient 63

Chapter 6 Field Effect Transistor Studies **64**

6.1 Zinc Tin Oxide 64

6.1.1 Sample Fabrication 64

6.1.2 Physical Characterization 65

6.1.3 Field Effect Mobility vs. Stoichiometry 66

6.1.4 Threshold Voltage, Sub-Threshold Swing, On/Off Ratio 68

6.2 Zinc Indium Oxide 69

6.2.1 Sample Fabrication 69

6.2.2 Physical Characterization 70

6.2.3 Field Effect Mobility vs. Stoichiometry 72

6.2.4 Threshold Voltage, Sub-Threshold Swing, On/Off Ratio 73

6.2.5 X-ray Diffraction and Transparency 75

6.2.6 TFT Study Conclusions 76

Chapter 7 Thermal Conductivity of an SiO_2 Wedge **77**

7.1 Sample Fabrication 77

7.2 Substrate Thermal Conductivity 78

7.3 SiO_2 Film Thermal Conductivity 80

7.4 Interfacial Thermal Resistance 82

7.5 Temperature Dependence 83

7.6 SiO_2 Wedge Study Conclusions 84

7.6.1 3ω Data Point Selection Criteria 84

Chapter 8 Zinc Tin Oxide Thermoelectric Study **86**

8.1 90% Ar, 10% O_2 Sputtering Condition 86

8.1.1 Fabrication of 90% Ar, 10% O_2 Samples 86

8.1.2 Physical Characterization of 90% Ar, 10% O_2 Samples 87

8.1.3 Thermal Conductivity of 90% Ar, 10% O_2 Samples 90

8.1.4 Electrical Conductivity of 90% Ar, 10% O_2 Samples 95

8.1.5 Seebeck Coefficient of 90% Ar, 10% O_2 Samples 97

8.1.6 Thermoelectric Figure of Merit . . . 98
8.2 Effective Lorenz Number . . . 99
8.3 100% Ar Sputtering Condition . . . 100
8.3.1 Fabrication of 100% Ar Samples . . . 100
8.3.2 Physical Characterization of 100% Ar Samples . . . 101
8.3.3 Thermal Conductivity of 100% Ar Samples . . . 103
8.3.4 Electrical Conductivity of 100% Ar Samples . . . 106
8.3.5 Seebeck Coefficient of 100% Ar Samples . . . 111
8.3.6 Thermoelectric Figure of Merit . . . 111
8.4 Effective Lorenz Number . . . 113
8.5 Zinc Tin Oxide Thermoelectric Study Conclusions . . . 113

Chapter 9 Zinc Indium Oxide Thermoelectric Study 115
9.1 80% Ar, 20% O_2 Sputtering Condition . . . 115
9.1.1 Fabrication of 80% Ar, 20% O_2 Samples . . . 115
9.1.2 Physical Characterization of 80% Ar, 20% O_2 Samples . . . 116
9.1.3 Thermal Conductivity of 80% Ar, 20% O_2 Samples . . . 118
9.1.4 Electrical Conductivity of 80% Ar, 20% O_2 Samples . . . 123
9.1.5 Seebeck Coefficient of 80% Ar, 20% O_2 Samples . . . 125
9.1.6 Thermoelectric Figure of Merit . . . 126
9.2 Effective Lorenz Number . . . 127
9.3 100% Ar Sputtering Condition . . . 128
9.3.1 Fabrication of 100% Ar Samples . . . 128
9.3.2 Physical Characterization of 100% Ar Samples . . . 129
9.3.3 Thermal Conductivity of 100% Ar Samples . . . 131
9.3.4 Electrical Conductivity of 100% Ar Samples . . . 136
9.3.5 Seebeck Coefficient of 100% Ar Samples . . . 139
9.3.6 Thermoelectric Figure of Merit . . . 139
9.4 Effective Lorenz Number . . . 140

9.5 ZIO Thermoelectric Study Conclusions 141

Chapter 10 Conclusions and Future Work **143**

10.1 Future Work 147

References **150**

Appendix A Uncertainties **157**

A.1 Thermal Conductivity 157

A.2 Electrical Conductivity 159

A.3 Seebeck Coefficient 160

A.4 Carrier Concentration 160

A.5 Thermoelectric Figure of Merit and Effective Lorenz Number 160

Appendix B Publications **161**

Appendix C Copyright Permissions **162**

List of Tables

Table 8.1 Calculated dimensionless figures of merit for ZTO films sputtered under 10% oxygen and annealed at 300°C and 600°C under oxygen. A temperature of 300 K was used for all measurements. Calculated for $T = 300$ K. 99

Table 8.2 Calculated effective Lorenz numbers for ZTO films sputtered under 10% oxygen and annealed at 300°C and 600°C under oxygen. A temperature of 300 K was used for all measurements. Calculated for $T = 300$ K. 99

Table 8.3 Calculated dimensionless figures of merit for ZTO films sputtered under argon, both as-deposited and annealed at 600°C under O_2. Calculation of ZT for the argon-annealed films was not possible due to the problems encountered determining thermal conductivity. Calculated for $T = 300$ K. 112

Table 8.4 Effective Lorenz numbers for ZTO films sputtered under argon, both as-deposited and annealed at 600°C under O_2. Calculation of L_{eff} for the argon-annealed films was not possible due to the problems encountered determining thermal conductivity. Calculated for $T = 300$ K. 113

Table 9.1 Calculated dimensionless figures of merit for ZIO films sputtered under oxygen for $T = 300$ K. 126

Table 9.2 Calculated effective Lorenz numbers for ZIO films sputtered under oxygen for $T = 300$ K. 127

Table 9.3 Calculated dimensionless figures of merit for ZIO films sputtered under argon, calculated for $T = 300$ K. 140

Table 9.4 Calculated effective Lorenz numbers for ZIO films sputtered under argon, calculated for $T = 300$ K. 141

List of Figures

Figure 2.1 Cross section of a typical ZIO or ZTO device fabricated on a heavily doped silicon wafer. In this device the wafer acts as a gate contact, and the SiO_2 layer acts as the dielectric. 7

Figure 2.2 A typical saturation transfer characteristic for an enhancement mode, n-channel thin film transistor. 10

Figure 2.3 A current I passing through a square (i.e. $L = W$) of material of thickness d will be subject to the same resistance regardless of the value of $L = W$. 13

Figure 2.4 Geometry for van der Pauw sheet resistance (left) and Hall effect (right) measurements. 14

Figure 2.5 Semi-infinite plane with contacts at the boundary. Current flows in through A and out through B. 15

Figure 2.6 Cloverleaf structure with ideal (solid dot) and non-ideal (hollow dot) contact placement. 17

Figure 2.7 Geometry of a typical Hall effect measurement for an n-type material. 18

Figure 3.1 Design for stencil masks used to pattern the films during sputtering. The mask is ‘open’ in the black areas, resulting in film being deposited in those locations. A set of alignment markers can be seen around the perimeter of the design. A magnified cloverleaf is shown (inset). 35

Figure 3.2 Cross section after metal application, but before removal of the remaining resist. 38

Figure 5.1 Stencil mask used to pattern the semiconductor oxide during sputtering. Each 'pad' of sputtered oxide is electrically isolated from its neighbours, minimizing fringing effects and allowing the use of a common gate electrode for all devices. 49

Figure 5.2 Metal contact stencil masks for the TFT portion of the project. The thin strips of metal are for use in characterizing the contact resistance between the aluminum contacts and the semiconductor. 50

Figure 5.3 The photomask used to pattern the metal heaters, contact pads, sense lines, and current buses on samples used in the automated 3ω system. The label A indicates a set of 32 heaters which can be contacted 16 at a time using the contact pads on either side. Both groups of 16 heaters share a common, positive current bus between them. The structures under label B are 'manual' heaters that can be contacted using conductive probes. Label C indicates the metal contacts for a set of 'cloverleaf' structures used in van der Pauw sheet resistance measurements. 53

Figure 5.4 Original heater design at the edge of a heater group. Note the 'sharp' corner on the current injection line. It is speculated that the increase in resistance at this point created a hot spot that affected the measured temperature of the heater. Another possible problem is heating of the current injection line (oval). 54

Figure 5.5 Updated photomask, designed to minimize heat generated from current injection lines. 55

Figure 5.6 Exploded view of the entire assembly, with holder (blue), PCB (green) and wafer (red). 56

Figure 5.7 Schematic diagram of the experimental setup. Each heater has a single common contact (the positive AC out) and three switched contacts: the negative AC out, and two sense contacts connected to channels A and B of the lock-in amplifier. 58

Figure 6.1 Measured stoichiometry of the mixed zinc oxide/tin dioxide sputtered film. 66

Figure 6.2 A typical saturation transfer curve (V_{DS} = +25 V). The device in this figure has a composition of $x = 0.43$. 67

Figure 6.3 Mobility as a function of zinc oxide fraction across an entire wafer of devices. Note that the line serves as a guide to the eye only. 68

Figure 6.4 Threshold voltage and on/off ratio as a function of zinc oxide fraction across an entire wafer of ZTO devices. The sudden decrease in both threshold voltage and on/off ratio is due to the light sensitivity of these devices. 69

Figure 6.5 Measured stoichiometry of the mixed zinc oxide/tin dioxide sputtered film, comparing the original, measured stoichiometry and the same data corrected using Casino (solid line). . . . 71

Figure 6.6 A typical saturation transfer curve with V_{DS}=+25V. This figure shows the methods used to determine saturation mobility, threshold voltage and sub-threshold slope. The device has a channel stoichiometry corresponding to x=0.74. 72

Figure 6.7 Mobility as a function of channel stoichiometry for both 300°C and 600°C annealing conditions. 73

Figure 6.8 Sub-threshold slopes for 300°C and 600 °C annealing conditions as functions of molar ratio. 74

Figure 6.9 XRD example data for 600°C annealing conditions at a variety of film stoichiometries. It should be noted that XRD data were taken for different stoichiometries in steps of δx=0.02. For clarity, only selected stoichiometries are shown. 75

Figure 7.1 A representative set of data for a heater on the SiO_2 wedge. Third harmonic RMS voltage as a function of the frequency of the applied voltage is displayed for a number of applied RMS powers. This heater was on an SiO_2 film thickness of 98 nm. . . 79

Figure 7.2 Comparison of the apparent substrate thermal conductivity as a function of sputtered SiO_2 film thickness. Data calculated using equations (2.51) (imaginary) and (2.52) (real) are shown. 80

Figure 7.3 Temperature amplitude per unit power as a function of SiO_2 film thickness for all heaters on the SiO_2 wedge. 81

Figure 7.4 Film thermal conductivity as calculated for each heater on the SiO_2 wedge using two methods. To subtract the influence of the substrate and Al_2O_3, the temperature per unit power for a position with no SiO_2 was measured, and this value was subtracted from the data at each SiO_2 thickness. The dotted line indicates the error range for κ_f calculated using the slope in figure 7.3. 82

Figure 7.5 Silicon substrate thermal conductivity as a function of temperature for select devices on the SiO_2 wedge. 83

Figure 8.1 Measured thickness as a function of sputtering table position for ZTO films sputtered under 10% oxygen. Zinc oxide content increases with radial position. 88

Figure 8.2 Film mass and density as a function of sputtering table position for ZTO films sputtered under 10% oxygen. 88

Figure 8.3 Relative atomic fraction of Zn and Sn as a function of radial position on the sputtering table for ZTO films sputtered under 10% oxygen. 89

Figure 8.4 Thermal conductivity at room temperature as a function of zinc oxide fraction for ZTO films sputtered under 10% oxygen. Data for as-deposited, 300°C oxygen, and 600°C oxygen annealing conditions are presented. Note that the lines serve as a guide to the eye only. 90

Figure 8.5 X-ray diffraction data for as-deposited ZTO films sputtered under 10% oxygen at multiple zinc oxide fractions x. 91

Figure 8.6 Comparison of XRD data for selected zinc oxide fractions of ZTO films sputtered under 10% oxygen, for as-deposited, 300°C under oxygen and 600°C under oxygen annealing conditions. 92

Figure 8.7 XRD results for ZTO films deposited in 10% oxygen and annealed at 300°C under oxygen. 93

Figure 8.8 An optical image of the 'rough' area (left) and normal, 'smooth' area (right) on the 300°C annealed film for zinc oxide fractions of 0.7 < x < 0.85. The change in character is abrupt, occurring over a radial distance of less than 1 mm. 94

Figure 8.9 XRD results for ZTO films deposited in 10% oxygen and annealed at 600°C under oxygen. Three phases are visible across the range, one below $x = 0.5$, another around $x = 0.68$ and finally the ZnO phase observed earlier. A closer examination of these phases is shown in figure 8.6. 95

Figure 8.10 Electrical conductivity as a function of zinc oxide fraction, for ZTO films sputtered under 10% oxygen and annealed under oxygen at 300°C and 600°C. 96

Figure 8.11 Charge carrier concentration as a function of stoichiometry for the 600°C annealing condition of ZTO sputtered under 10% oxygen. 97

Figure 8.12 Seebeck coefficients for all ZTO films sputtered under 10% oxygen. The $x = 0.2$, 0.45 and 0.95 stoichiometries in the 300°C annealing condition all produced relatively high magnitude Seebeck coefficients, with $x = 0.45$ measured to be -250 μV/K. . 98
Figure 8.13 Measured thickness of ZTO films sputtered under argon as a function of radial position on the sputtering table. Zinc oxide content increases with radial position. 101
Figure 8.14 Film mass and density as a function of table position for ZTO films sputtered under argon. 102
Figure 8.15 Normalized atomic fractions of Zn and Sn as a function of radial position on the sputtering table for the 100% argon sputtering run. 103
Figure 8.16 Thermal conductivity at room temperature of ZTO films sputtered under pure argon, for the as-deposited and 600° oxygen annealing conditions, presented as a function of zinc oxide fraction. 104
Figure 8.17 XRD results for as-deposited ZTO films deposited in argon at a variety of zinc oxide fractions. 105
Figure 8.18 Larger plots of XRD data for ZTO films sputtered under argon for selected zinc oxide fractions, and all annealing conditions. 106
Figure 8.19 XRD results for ZTO films deposited in argon and annealed at 600°C under oxygen. 107
Figure 8.20 (Top Left) Thermal conductivity of films annealed at 600°C under argon, as a function of zinc oxide fraction. (Top Right) Temperature amplitude per watt for both the heaters on 600°C Ar-annealed films and their adjacent 'reference' heaters. (Bottom) For comparison, temperature amplitude per watt for both the heaters on as-deposited ZTO films sputtered under argon and their adjacent 'reference' heaters. 108

Figure 8.21 XRD results for ZTO films deposited in argon and annealed at 600°C under argon. 109
Figure 8.22 Electrical conductivity of ZTO films sputtered under argon as a function of zinc oxide fraction for all annealing conditions. . 110
Figure 8.23 Charge carrier concentration of ZTO films sputtered under argon, for all annealing conditions. 110
Figure 8.24 Seebeck coefficients for all ZTO films sputtered under argon. 112

Figure 9.1 Measured thickness of ZIO films sputtered under 20% oxygen as a function of radial position on the sputtering table. Zinc oxide content increases with radial position. 116
Figure 9.2 Film mass and density for ZIO films sputtered under 20% oxygen. 117
Figure 9.3 Normalized atomic fractions of Zn and In as a function of radial position on the sputtering table for the 80% argon, 20% oxygen sputtering run. 118
Figure 9.4 Thermal conductivity at room temperature of ZIO films sputtered in 20% oxygen as a function of zinc oxide fraction. . . . 119
Figure 9.5 XRD results for as-deposited ZIO films deposited in 20% oxygen. 119
Figure 9.6 XRD for selected stoichiometries of ZIO sputtered under 20% oxygen for all annealing conditions. 120
Figure 9.7 XRD results for 300°C oxygen-annealed ZIO films deposited in 20% oxygen. 121
Figure 9.8 XRD results for ZIO films deposited in 20% oxygen and annealed at 300°C under argon. 122
Figure 9.9 Electrical conductivity of ZIO films sputtered in 20% oxygen as a function of zinc oxide fraction. 123
Figure 9.10 Carrier density for ZIO films sputtered under 20% oxygen. . . 124

Figure 9.11 XRD results for all ZIO films sputtered under 20% oxygen. . 125
Figure 9.12 Measured thickness of ZIO films sputtered under argon as a function of radial position on the sputtering table. Zinc oxide content increases with radial position. 129
Figure 9.13 Film mass and density for ZIO films sputtered under argon. . 130
Figure 9.14 Normalized atomic fractions of Zn and In as a function of radial position on the sputtering table for the 100% argon sputtering run. 131
Figure 9.15 Thermal conductivity at room temperature of ZIO films sputtered in argon as a function of zinc oxide fraction. 132
Figure 9.16 XRD results for as-deposited ZIO films deposited in argon. . 133
Figure 9.17 XRD for selected values of x for argon-sputtered ZIO films. . 134
Figure 9.18 XRD results for ZIO films deposited in argon and annealed at 300°C under oxygen. 135
Figure 9.19 XRD results for ZIO films deposited in argon and annealed at 300°C under argon. 136
Figure 9.20 Electrical conductivity of ZIO films sputtered in argon as a function of zinc oxide fraction. 137
Figure 9.21 Charge carrier concentration in ZIO films sputtered under argon for all three annealing conditions. Of particular note is the lack of difference between the as-deposited and argon-annealed films, while annealing under oxygen significantly reduces carrier density for higher values of x, suggesting that oxygen vacancies in the films are the primary carrier source in zinc-rich ZIO films. 138
Figure 9.22 Seebeck coefficients for all ZIO films sputtered under argon. . 139

Figure A.1 Close up view of a standard heater. The horizontal line is the heater element, with a width of 25 μm. 159

Abstract

The effects of stoichiometric ratio, oxygen (both during sputtering and annealing), and annealing on the transistor and thermoelectric properties of zinc indium oxide (ZIO) and zinc tin oxide (ZTO) were studied. Thin films of $(ZnO)_x(In_2O_3)_{1-x}$ and $(ZnO)_x(SnO_2)_{1-x}$ were fabricated via combinatorial RF sputtering, nominally varying from $0 > x > 1$. The films were post-annealed under either argon or oxygen, or left as-deposited. Films sputtered under an argon/oxygen mixture were used in the construction of thin-film transistors. ZIO TFTs annealed under oxygen at 300°C exhibited field-effect electron mobilities of 30 cm^2/V·s around $x = 0.7$, with on/off ratios as high as 10^9, and inverse sub-threshold slopes of less than 1 V/dec. ZTO TFTs annealed at 600°C under oxygen exhibited mobilities of 10 cm^2/V·s at $x = 0.25$ and $x = 0.80$, with inverse sub-threshold slopes of 1.5 V/dec and on/off ratios of 10^6. For the determination of thermoelectric properties, a room-temperature value of ZT was calculated for each fabrication condition with all measurements from a single fabrication run. Films were post-annealed under either argon or oxygen. ZIO was found to be highly sensitive to oxygen during sputtering, with effective Lorenz numbers (L_{eff}) for un-annealed films four orders of magnitude lower when sputtered under argon, close to the ideal Lorenz number, indicating oxygen vacancies as the primary electron donor. Thermal conductivity was generally found to rise toward the edges of the stoichiometric range, with a low of 2 W/m·K. ZT was highest in ZIO at 0.02±0.01 for x near 0.5 in films sputtered under partial oxygen and annealed at 300°C under oxygen. Un-annealed ZTO films were also sensitive to oxygen during sputtering, but L_{eff} for argon-sputtered films was on the order of 10^{-4} W·Ω/K^2, indicating semiconductor-like behaviour, while partial-oxygen sputtered ZTO was highly resistive. Thermal conductivity was low (2 to 5 W/m·K) for most fabrication conditions except near the zinc-rich end of the range. For ZTO, the highest ZT was 0.004±0.002 for argon-sputtered, un-annealed films, at zinc-rich stoichiometries of $x > 0.9$.

List of Abbreviations and Symbols Used

α	Thermal diffusivity
α_S	Substrate thermal diffusivity
ΔT	Temperature difference
Δ	Polarization angle
η	Efficiency
κ	Thermal conductivity
κ_f	Film thermal conductivity
κ_n	n-type thermal conductivity
κ_p	p-type thermal conductivity
κ_s	Substrate thermal conductivity
λ	Wavelength
μ	Majority charge carrier mobility
μ_n	Electron mobility
μ_p	Hole mobility
∇T	Temperature gradient
∇V	Voltage gradient
ω	Angular frequency
$\overline{S}$	Combined Seebeck coefficient
ψ	Arctangent of the ratio of 'p' to 's' polarizations
ρ	Resistivity
σ	Electrical conductivity
σ_n	n-type electrical conductivity
σ_p	p-type electrical conductivity
Θ	Ratio of complex reflection coefficients
θ	Scattering angle
ζ	Empirically determined constant, near 1

A	Area
a-Si	Amorphous Silicon
A_C	Cauchy parameter
A_n	n-type leg cross-sectional area
A_p	p-type leg cross-sectional area
B	Magnetic field
b	Heater half-width
B_C	Cauchy parameter
C_C	Cauchy parameter
C_{ox}	Capacitance of transistor oxide insulator material
C_{RT}	Temperature coefficient of resistance
d	Thickness
d_f	Film thickness
d_l	Lattice plane spacing
d_t	Thermal penetration depth
E	Electric field
f	Frequency
I	Current
I_o	Current amplitude
i_{DS}^{lin}	Linear mode drain-source current
i_{DS}^{sat}	Saturation mode drain-source current
J	Current density
K	Combined FET properties
k	Boltzmann constant
L	Lorenz number
l	Length
l_n	n-type leg length
l_p	p-type leg length
L_{11}	Electric Field coefficient

L_{12}	Kinetic coefficient
L_{eff}	Effective Lorenz number
N	Complex index of refraction
n	Electron charge carrier density
N_{charge}	Total charge carrier density
N_{trap}	Trapped charge carrier density
P	Power
p	Hole charge carrier density
P_{in}	Power input
P_{out}	Power output
q	Fundamental charge
Q_joule	Heat produced due to Joule heating
Q_{flow}	Heat flow due to temperature gradient
Q_{pelt}	Heat absorbed due to Peltier cooling
R	Resistance
r	Radius
R_H	Hall coefficient
R_h	Heater resistance
R_L	Load resistance
R_p	'p' polarization complex reflection coefficient
R_S	Sheet resistance
R_s	's' polarization complex reflection coefficient
R_{in}	Internal resistance
S	Seebeck coefficient
s	Inverse sub-threshold slope
S_n	n-type Seebeck coefficient
S_p	p-type Seebeck coefficient
T	Temperature
T_s	Temperature amplitude at the substrate

$T_{2\omega}$	Temperature amplitude at 2ω
T_{meas}	Measured temperature amplitude
V	Voltage
v_d	Drift velocity
V_S	Seebeck voltage
V_T	Threshold voltage
$V_{1\omega}$	Applied RMS voltage
$V_{3\omega}$	RMS voltage at 3ω
V_{DS}	Drain-source voltage
V_{GS}	Gate-source voltage
W	Width
x	Zinc Oxide Fraction
Z	Thermoelectric figure of merit
ZT	Dimensionless thermoelectric figure of merit
GPIB	General Purpose Interface Bus
MISFET	Metal-Insulator-Semiconductor Thin Film Transistor
PCB	Printed Circuit Board
TFT	Thin Film Transistor
ZIO	Zinc indium oxide
ZTO	Zinc tin oxide

Acknowledgements

My thanks go out to my committee members Dr. Jeff Dahn and Dr. Mary Anne White, whose guidance and objectivity were essential in keeping both myself and the project on track and in focus. I would also like to thank Dr. Ted Monchesky and Dr. Daniel Labrie, both of whom provided essential technical and moral support.

I also owe much to Robbie Sanderson, Eric McCalla, Mark McArthur and Mike Johnson for their instruction and help regarding the wide variety of techniques needed for this project.

I want to thank my friends and family who also helped to make this possible, and in particular my fiancée Mel, without whose love, support, patience and encouragement I could never have finished this project.

Lastly, I would like to extend my deepest thanks and appreciation to Dr. Ian Hill, without whom this work would not have been possible. His input, guidance, encouragement and endless patience made it possible to bring this project to fruition. I consider his influence both during this project and during my undergrad to have been essential not just to this project, but to whom I have grown to be as a person. Thank you Ian.

Chapter 1

Introduction[1]

1.1 Semiconductor Background

A research focus regarding materials for use in consumer electronics devices has been in finding inexpensive, high-mobility semiconductors compatible with large-area substrates, generally for use in flat-panel displays. These materials would not only allow for less expensive manufacture (both in terms of materials and energy input) of efficient displays, but would also allow for the use of lightweight, and even flexible, substrate materials that are incompatible with the high temperature fabrication techniques required for the amorphous silicon (*a*-Si) that is currently used in this context. A significant portion of the research currently done on materials in this field is focused on oxide semiconductors. The recent interest in these materials was sparked by papers concerning zinc oxide (ZnO) in thin film transistors (TFTs)[1, 2], and has since expanded to cover combinations of oxides as well.

1.2 Mixed Oxide Semiconductors

In active matrix displays, the semiconductors used in thin-film transistors must have relatively high carrier mobility and, for use in flexible applications, be insensitive to bending as well. In large area applications such as flat panel displays, amorphous silicon (*a*-Si) is most commonly used. Other semiconductors are also being explored,

[1]Some sections of this chapter have been reprinted with permission from M. G. McDowell, R. J. Sanderson, and I. G. Hill, Combinatorial study of zinc tin oxide thin-film transistors, Applied Physics Letters, 92:013502, Copyright 2008, AIP Publishing LLC.

Some sections © 2009 IEEE. Some sections reprinted, with permission, from M. G. McDowell and Ian G. Hill, Influence of Channel Stoichiometry on Zinc Indium Oxide Thin-Film Transistor Performance, IEEE Transactions on Electron Devices, February, 2009.

for example the organic material pentacene[3]. These materials are generally limited to mobilities on the order of 1 $cm^2/V\cdot s$[1, 2, 4]. On the other hand, amorphous metal oxides and mixed metal oxides have been shown[5, 6, 7, 8, 9, 10, 11] to have high mobilities (up to 50 $cm^2/V\cdot s$). These materials are often transparent[12] and have the benefit of being very durable.

Among mixed metal oxides, zinc tin oxide (ZTO) has attracted attention, due to its high mobility and optical transmittance[7, 13, 14], which offer the possibility of high-performance transparent electronics for applications such as displays. When used in displays, transparent transistors offer an increase in backlight transmission and therefore power efficiency. ZTO is also interesting for use in flexible devices[15]. Transistors fabricated via sputtering of ZTO have achieved mobilities as high as 50 $cm^2/V\cdot s$ and on/off ratios of 10^7[7, 16]. These devices were primarily fabricated using pre-made sputtering targets, usually of a ZnO:SnO_2 molar mixture of 1:1 or 2:1. Due to the impracticality of fabricating separate targets for a large variety of different stoichiometries, only a limited number of these ratios had been explored. ZTO is known to be crystalline in the forms $ZnSnO_3$[17] (in an ilmenite-type structure[17]) and Zn_2SnO_4[18] (in both spinel and inverse spinel structures[19]). This makes the 1:1 and 2:1 ratios of zinc to tin that are most commonly tested seem to be the obvious choices, as it is often the case that the crystalline forms of a material have higher carrier mobilities. Despite this, the electronic properties of these films are not particularly well understood and a combinatorial study of ZTO-based thin-film transistor performance was necessary. To this end, a preliminary study[20] was conducted for $(ZnO)_x(SnO_2)_{1-x}$ devices at five different stoichiometries of $x = 0$, 0.33, 0.50, 0.67 and 1, examining mobility as a function of stoichiometry and annealing conditions. However, while this study found mobility to have a 'broad peak' with respect to stoichiometry with the highest electron mobility at $x = 0.50$, it was too coarse-grained to accurately describe the relationship between stoichiometry and electron mobility.

Zinc indium oxide (ZIO) also shows promise as a high-mobility transparent semiconductor. Research on this material has focused on two regimes: one of indium-rich

devices[21, 22, 23], and another of zinc-rich devices[24, 25, 26, 27]. While a great deal of work has been done to study structure[28], RF characteristics[27] and charge transport[29] in ZIO films, devices have only been fabricated for a small number of discrete molar ratios, due to the difficulties involved in preparing sputtering targets for individual stoichiometric ratios of interest. In the zinc-rich regime, the most successful of these was 2:1 (ZnO:In_2O_3), annealed at temperatures of 300°C and 600°C yielding field effect mobilities of $\sim$20 $cm^2/V{\cdot}s$ and $\sim$50 $cm^2/V{\cdot}s$, respectively[24]. While prior combinatorial work has been done for similar devices composed of indium, zinc and gallium oxides[30], the gallium content in these devices was never less than 10%, and therefore the pure ZIO range of stoichiometries has not yet been explored.

1.3 Thermoelectric Background

As concerns about climate change and energy generation continue to mount[31, 32], interest in alternative forms of power generation has intensified. This has reignited interest in the use of thermoelectric materials, for use not just as a primary means of energy generation (such as in a radioisotope thermoelectric generator, commonly used on spacecraft, such as the Voyager probes), but also in recovering waste heat from other means of energy production, such as the burning of fossil fuels, in which a substantial fraction of the chemical energy released is lost directly to heat. Thermoelectric generators also have the advantage of being relatively inexpensive to operate due to a lack of moving parts, and are environmentally friendly, producing no harmful bi-products while in operation. However, the efficiency of thermoelectric devices is still relatively low. Improvements to thermoelectric devices are therefore of significant interest to the scientific community at large.

Thermoelectric materials are generally evaluated using the thermoelectric figure of merit, Z, which is usually presented in a dimensionless form ZT. This figure takes the form[33, 34, 35]

$$ZT = \frac{S^2\sigma}{\kappa}T, \tag{1.1}$$

where S is the Seebeck coefficient, σ is the electrical conductivity, and κ is the thermal conductivity of the material in question, while T is the temperature at which these parameters were measured. A more detailed discussion of the origin of this figure of merit is presented in section 2.6. While at first glance it seems obvious that this value can be optimized by increasing S and/or σ and decreasing κ, these properties are not orthogonal. For example, σ could be significantly increased in a given material by increasing doping, thereby increasing the carrier concentration and resulting electrical conductivity. However, since charge carriers are capable of transferring heat as well as charge, an increase in doping will result in an increase in thermal conductivity as well. Similarly, a significant decrease in charge carrier density might decrease κ, but will also decrease σ.

There is a wide variety of different thermoelectric materials, the most common of which is bismuth telluride[32, 36], which has a dimensionless thermoelectric figure of merit of ~1 at room temperature[32, 36, 37]. While this value of ZT is considered 'good', and has resulted in application of Bi_2Te_3 in a variety of thermoelectric applications, a value of $ZT = 1$ only corresponds to approximately 10% of the theoretical maximum achievable efficiency, while a value of $ZT > 4$[32, 38] is generally considered to be required for thermoelectric materials to compete directly (in terms of efficiency) with other common forms of energy generation.

A primary strategy for increasing ZT is to decrease κ[32, 36] through manipulation of the structure of the thermoelectric material. Creation of nano-scale layers and structures in a material can significantly increase the density of phonon scattering sites, lowering thermal conductivity and subsequently increasing ZT[39]. The phonon-glass electron-crystal (PGEC) concept has also attracted recent attention[40, 32], the idea being that a material behaves largely like a crystalline semiconductor electrically, but is structured to maximize the scattering of phonons, reducing κ.

Clathrates are an example of this type of material system, in which a large unit cell with a significant void acts as a ‘cage’, with the void within it filled with a loosely-bound ‘rattler’ atom that acts as a scattering center for phonons[32, 41].

While these nano-structured materials are a promising line of research for maximizing ZT, the idea of a bulk thermoelectric material with high ZT is attractive from a cost and ease-of-manufacture perspective. Bulk oxide semiconductors such as zinc oxide and associated mixtures with other oxides are therefore attractive candidates as thermoelectric materials. Semiconductors are generally excellent candidates for thermoelectric materials, as they tend to develop the largest Seebeck coefficients and have carrier concentrations that produce relatively high electrical conductivity, without thermal conductivity being dominated by charge carrier transport[32].

1.4 Mixed Oxide Thermoelectric Properties

Besides features such as high mobility and transparency, the semiconductors ZTO and ZIO discussed above also tend to be largely amorphous when deposited via sputtering. In general, amorphous materials will have poor thermal conductivity due to high phonon scattering. Even when annealed and found to be poly-crystalline, thermal conductivity may remain low due to scattering at grain boundaries. The combination of a high-mobility semiconducting properties with a largely amorphous structure makes these materials interesting in a thermoelectric context. Most of the interest in ZIO and ZTO has focused on use in semiconductors. In general, for any application of these materials in devices it is also useful to have an understanding of their thermal transport properties as well. Zinc oxide has generated a great deal of interest for use as a thermoelectric material[42, 43, 44], and is often doped with other materials[45, 46, 47, 48, 49] or nanostructured as part of the fabrication process[50, 51]. The effect of annealing gas and temperature is often studied as part of the fabrication process for these materials[52, 53, 54]. As an example, ZIO has attracted interest as a thermoelectric material[55, 56, 57, 58, 59]. However, studies

are generally focused on fixed stoichiometric ratios and/or oxygen conditions, or are conducted for high temperature fabrication techniques that make them incompatible with inexpensive or flexible applications. Some combinatorial studies of ZTO[60], discussing the oxygen sensitivity of electrical conductivity, and ZIO[61], discussing electrical conductivity and Seebeck coefficient, have been conducted. However, these combinatorial studies neglect to determine thermal conductivity, generally due to the relative difficulty in measuring the thermal conductivity of sputtered films. In particular, the relationship between oxygen during sputtering and annealing, and thermal conductivity and Seebeck coefficient, has not been explored. It is the purpose of the present study not just to determine the thermoelectric properties of the films of interest for a range of stoichiometric ratios, but to use a variety of sputtering and annealing gas conditions to shed light on the physics of both electrical and thermal transport within them as well.

1.5 Goals

This study seeks to examine the role of stoichiometric ratio, oxygen content during sputtering and annealing, and annealing temperature on the semiconductor and thermoelectric properties of sputtered mixtures of zinc oxide and tin oxide, as well as mixtures of zinc oxide and indium oxide. These data will be collected from single samples, with all relevant parameters measured on films created in a single fabrication run. This information will allow identification of optimal fabrication conditions for potential applications of these materials in either transistor or thermoelectric applications. The goal is to provide a framework for understanding the physics of how these fabrication parameters influence the performance of these materials, and to provide a framework that can be used to predict the performance of similar materials in the future.

Chapter 2

Theory

2.1 Field Effect Transistors

In the early stages of this study, the materials presented were characterized for use in thin-film field effect transistors. The results of these experiments are presented in chapter 6. The results of the transistor experiments suggested that the materials studied may be interesting in thermoelectric applications.

2.1.1 Field Effect Transistor Operation

In a metal-insulator-semiconductor field effect transistor (MISFET), the electric field from a gate contact (which is separated from the semiconductor by a dielectric film), causes a build-up of mobile charge carriers in a few atomic layers of the semiconductor adjacent to the dielectric. This high concentration of charge carriers creates a conductive channel which allows current to flow between drain and source electrodes deposited in direct contact with the film.

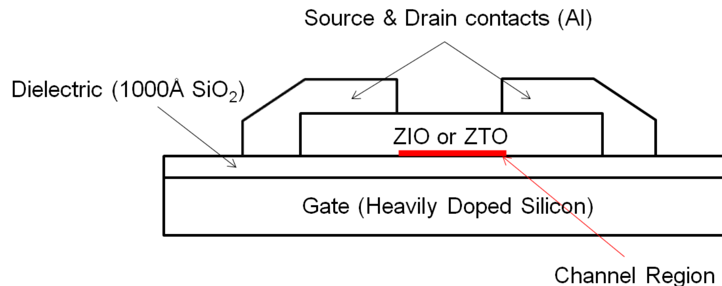

Figure 2.1: Cross section of a typical ZIO or ZTO device fabricated on a heavily doped silicon wafer. In this device the wafer acts as a gate contact, and the SiO_2 layer acts as the dielectric.

There are two possible types of metal oxide field effect transistor, known as enhancement mode and depletion mode, based on the operation of the device with a drain-source voltage, but no gate voltage, applied. In an enhancement mode device, the device is normally off, and an applied gate voltage creates a channel through which current can flow from source to drain. In a depletion mode device the channel is conductive at zero gate voltage, and the gate voltage creates a carrier-depleted region in the semiconductor, preventing conduction from source to drain.

2.1.2 Field Effect Mobility

Carrier mobility in the channel can be determined using the ideal field effect transistor equations

$$K = \frac{1}{2}\mu C_{ox}\frac{W}{l}, \tag{2.1}$$

$$i_{DS}^{sat} = K(V_{GS} - V_T)^2, \quad V_{DS} > V_{GS} - V_T, \tag{2.2}$$

and

$$i_{DS}^{lin} = 2K(V_{GS} - V_T)V_{DS} - V_{DS}^2, \quad V_{DS} < V_{GS} - V_T. \tag{2.3}$$

Here μ is the field effect mobility, W and l are the width and length of the semiconductor film between the source and drain contacts, C_{ox} is the capacitance of the oxide per unit area, i_{DS}^{sat} is the saturation mode drain current, i_{DS}^{lin} is the linear mode drain current, and V_{GS}, V_{DS} and V_T are the gate, drain and threshold voltages, respectively.

However, these equations only yield the carrier mobility for films in which the drain current is modulated by the gate voltage, which excludes a large stoichiometric range of the materials studied, which are too highly conductive to make functional transistors. In this range, it is common that films are highly conductive, and are only minimally affected by the applied gate voltage. In films where the charge carrier density is so high that conduction from source to drain contacts is not modulated

entirely by the gate voltage, the above equations are not useful. Since high electrical conductivity is ideal for achieving a high thermoelectric figure of merit, it is likely that films that fail to satisfy these equations will need to be examined. Therefore, the charge carrier density and mobility in these films were determined using the Hall effect (section 2.3.3).

It should be noted that the mobility determined by either of the above means will be an average mobility, and will therefore take into account the mobility of any charge carriers trapped in the film (zero). In field effect transistor experiments done so far, the inverse sub-threshold slope was used to determine the density of trapped charges. The inverse sub-threshold slope (s) is the gate voltage change required for a given increase in drain current, usually measured in volts per decade. Using devices with the lowest apparent trap density (these correspond to the lowest inverse sub-threshold slopes), the areal trapped charge carrier density of states can be shown to be[62]

$$N_{trap} = \left(\frac{qs \cdot log(e)}{kT} - 1\right)\frac{C_{ox}}{q}. \tag{2.4}$$

The total areal charge carrier density is simply

$$N_{charge} = (V_{GS} - V_T)C_{ox}. \tag{2.5}$$

In devices that exhibit the lowest inverse sub-threshold slopes the ratio of $N_{trap} \cdot q \cdot (V_{GS} - V_T)$ to N_{charge} is approximately $\frac{1}{2}$, providing a lower bound to trap density that suggests the field effect mobility obtained in experiments so far is at most only one-half the mobility of a free charge carrier.

2.1.3 Threshold Voltage, Sub-threshold Swing, On/Off Ratio

Transistor performance is typically characterized using the threshold voltage, sub-threshold swing, on/off ratio and field effect mobility. These metrics are determined using an I-V transfer characteristic, in which the gate-source voltage is 'swept' over a range of values while the drain-source current is recorded, and the drain-source

voltage is held constant. An example I-V characteristic is shown in figure 2.2.

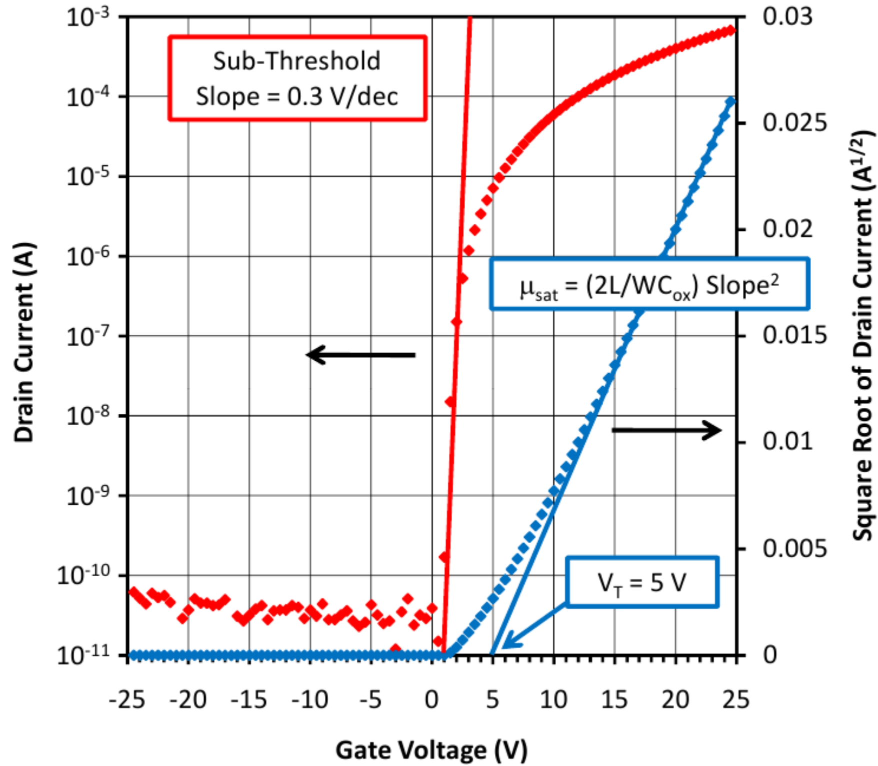

Figure 2.2: A typical saturation transfer characteristic for an enhancement mode, n-channel thin film transistor.

The threshold voltage (V_T) is defined as the point at which a complete 'channel' has formed at the semiconductor/dielectric interface, and is determined using the x-axis intercept of the square root of the source-drain current, when plotted against the gate-source voltage. For an n-channel transistor, the threshold voltage will be positive in an enhancement mode device, and negative in a depletion mode device. In a p-type device these are the reverse. A depletion mode I-V characteristic might look very similar to figure 2.2, but with all features shifted to the left on the gate-source voltage axis.

The sub-threshold swing is a measure of the difference in gate-source voltage necessary to create an order of magnitude increase in drain-source current, for a fixed drain-source voltage. The value reported is usually the highest value of the

inverse sub-threshold slope on a log-scale plot, and this tends to be found just as the device begins to turn on, as indicated in figure 2.2. Smaller sub-threshold swings are associated with better performance, as they indicate a a smaller change in voltage is necessary to change the device from off to on, or vice versa. This metric also provides information about the electronic structure of the semiconductor near the dielectric interface. A larger change in gate voltage is required to overcome 'trapped' charges. These are charge carriers with zero mobility that are physically confined by a defect in the structure of the semiconductor near the dielectric interface.

The on/off ratio is the ratio of the source-drain current when the device is fully 'on' (at some gate voltage greater than the threshold voltage) and when it is off (the smallest recorded source-drain current).

2.2 The Thermoelectric Figure of Merit

Determination of the thermoelectric figure of merit as a function of a variety of fabrication parameters was a primary goal of this study. The thermoelectric figure of merit helps to predict the thermodynamic efficiency of a thermoelectric device employing the material in question. The figure depends on the Seebeck coefficient of the material S, as well as its electrical conductivity σ, and its thermal conductivity κ. Put generally, a device employing materials with larger figures of merit will produce more power from a given temperature gradient than a similar device under the same conditions employing materials with lower figures of merit. Z takes the form[33, 34, 35]

$$Z = \frac{S^2\sigma}{\kappa}. \tag{2.6}$$

The components of the thermoelectric figure of merit are determined independently of one another. This value is usually reported in a dimensionless form, ZT, where T is the temperature at which the value of Z was measured, as

$$ZT = \frac{S^2\sigma}{\kappa}T. \tag{2.7}$$

For reference, the best bulk thermoelectric materials tend to have values for ZT of 1 - 2, with the highest reported being above 2.2[63].

In this study, determining Z required independent measurements of σ, S and κ.

2.3 Electrical Conductivity

The electrical conductivity of a material σ is a measure of that material's ability to conduct current. The conductivity of a material is a function of three parameters: the majority charge carrier mobility μ, the charge carrier concentration n or p (for the case where electrons or holes are the majority carrier, respectively), and the charge of each carrier q. For n and p type materials, respectively, the conductivity is expressed as

$$\sigma = \mu n q \tag{2.8}$$

and

$$\sigma = \mu p q. \tag{2.9}$$

It is often the case that the concentration of the majority carrier type renders the contribution from the other type negligible, and the conductivity is typically expressed using one of equations 2.8 or 2.9. However, for a material in which both electrons (n) and holes (p) contribute significantly to conductivity, the conductivity is simply the sum of the contributions of the two carrier types as in equation 2.10. Note that the two types of carriers have different mobilities (μ_n and μ_p) in addition to different concentrations. The combined equation is

$$\sigma = (\mu_n n + \mu_p p)q. \tag{2.10}$$

In the case of the thin films studied in this experiment, the conductivity of a given

film was determined using a sheet resistance measurement and a measurement of the film thickness to determine the resistivity of the film $\rho = \frac{1}{\sigma}$.

2.3.1 Sheet Resistance

Any square of uniform thickness of a homogeneous material will, regardless of size, have the same resistance (figure 2.3). For a given sample, any increase in length (assuming the current flows along the length) will result in a proportional increase in the resistance, while an increase in width will result in an inversely proportional decrease in resistance. Therefore any increase in both the length and width by a common factor will result in a sample of the same resistance. The resistance of a square of material of uniform thickness is the sheet resistance, and is measured in ohms (Ω) per square. The sheet resistance R_s of a material is a function of the resistivity ρ, the length L, the width W, and the thickness d, and is expressed as

$$R = \rho \frac{L}{A} = \frac{\rho}{d} \cdot \frac{L}{W} = R_S \frac{L}{W}. \tag{2.11}$$

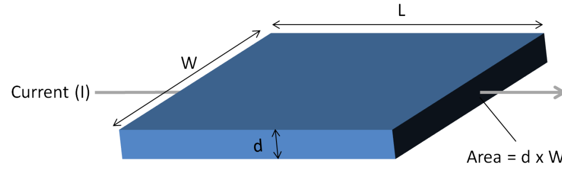

Figure 2.3: A current I passing through a square (i.e. $L = W$) of material of thickness d will be subject to the same resistance regardless of the value of $L = W$.

In this case $A = d \times W$ refers to the cross-sectional area. Rearranging equation 2.11, one can relate conductivity σ ($\frac{1}{\rho}$) with the sheet resistance and the thickness to get

$$\sigma = \frac{1}{\rho} = \frac{1}{R_S d}. \tag{2.12}$$

While σ can be used to calculate the thermoelectric figure of merit directly, it

is also useful to examine the components of σ (the charge carrier mobility μ and concentration n or p) to gain an understanding of the mechanisms of conduction in the film of interest. Finding these parameters can be accomplished using two van der Pauw measurements, one to determine conductivity, the other using the Hall effect to determine charge carrier density.

2.3.2 van der Pauw Measurements

When measuring the electrical properties of a material, it is not always possible to fabricate a sample in such a way that its dimensions are precisely known, nor is it always possible to tightly control the location and size of electrical contacts on that sample. The van der Pauw technique allows one to conduct sheet resistance and Hall effect measurements to determine the electrical properties of a sample of arbitrary shape, provided that the thickness of the sample is controlled.

While this technique is highly flexible with regard to the two dimensional shape, the sample must be simply connected (i.e. it should have no holes in it) and should be of uniform thickness. Additionally, the contacts should be as small and as close to the sample edge as possible.

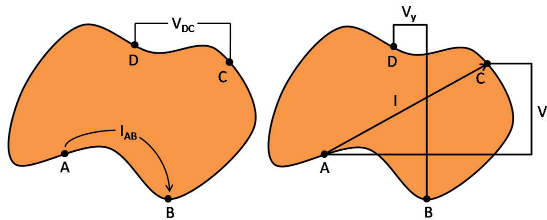

Figure 2.4: Geometry for van der Pauw sheet resistance (left) and Hall effect (right) measurements.

In a sheet resistance measurement, two resistances ($R_{AB,CD} = \frac{V_{CD}}{I_{AB}}$ and $R_{BC,DA} = \frac{V_{DA}}{I_{BC}}$) are first measured, in two perpendicular orientations, as in figure 2.4. To see how these can be used to find the sheet resistance, equate the current in the sample to the current flowing along the edge of a semi-infinite plane (figure 2.5).

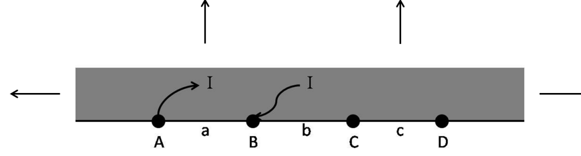

Figure 2.5: Semi-infinite plane with contacts at the boundary. Current flows in through A and out through B.

The potential difference between points C and D can be calculated using the current density (J) at a point in this solid due to the current (I) flowing in through point A. To find the current density at a distance from a current source at the edge of this solid, consider the current I distributed over a surface a distance r from point A. In a semi-infinite slab of material with a thickness d, at a distance $r >> d$, that surface area is πrd and the current density at r is[64]

$$J = \frac{I}{\pi rd}. \tag{2.13}$$

Note the factor of only π and not 2π since the plane is only semi-infinite. Substituting Ohm's law for current density ($J = \sigma E = \frac{E}{\rho}$) into equation 2.13, an expression can be derived for the electric field in the solid, due to a current I at point A and $-I$ at point B. Considering both the current in and current out, the electric field at a distance r from point A is found to be[64]

$$E = (J_A - J_B)\rho = \frac{I\rho}{\pi rd} - \frac{I\rho}{\pi(r-a)d}. \tag{2.14}$$

The potential difference between points C and D can be found by integrating the electric field between them which yields[64]

$$
\begin{aligned}
V_{CD} &= \int_D^C E \cdot dr \\
&= \frac{I\rho}{\pi d}\int_D^C \Big(\frac{1}{r} - \frac{1}{r-a}\Big)dr \\
&= \frac{I\rho}{\pi d}\Big[ln(a+b) - ln(b) - ln(a+b+c) + ln(b+c)\Big] \\
&= \frac{I\rho}{\pi d} ln\Big(\frac{(a+b)(b+c)}{b(a+b+c)}\Big).
\end{aligned} \tag{2.15}
$$

One can divide by the current I_{AB} to express equation 2.15 as the resistance $R_{AB,CD}$

$$
R_{AB,CD} = \frac{V_{CD}}{I_{AB}} = \frac{\rho}{\pi d} ln\Big(\frac{(a+b)(b+c)}{b(a+b+c)}\Big). \tag{2.16}
$$

Substituting $R_S d$ for ρ, results in

$$
-\frac{\pi R_{AB,CD}}{R_S} = ln\Big(\frac{b(a+b+c)}{(a+b)(b+c)}\Big). \tag{2.17}
$$

Applying a similar process to find $R_{BC,DA}$ yields

$$
-\frac{\pi R_{BC,DA}}{R_S} = ln\Big(\frac{ac}{(a+b)(b+c)}\Big). \tag{2.18}
$$

Eliminating the natural logarithms and adding the equations yields the final result[64] of

$$
e^{(\frac{-\pi R_{AB,CD}}{R_S})} + e^{(\frac{-\pi R_{BC,DA}}{R_S})} = 1. \tag{2.19}
$$

It is possible to generalize the solution in equation 2.19 by 'wrapping' the semi-infinite plane to form a closed shape. Unfortunately equation 2.19 cannot be solved for R_S, so no analytical solution exists for finding the sheet resistance from these two measured resistances. The original paper[64] detailing this technique provided a plot that could be used as a 'lookup table' for finding R_S based on the ratio of $R_{AB,CD}$ to

$R_{BC,DA}$. For the purposes of this study, a computerized, iterative approach was used to calculate R_S.

The accuracy of the van der Pauw technique can be compromised if the contacts are significant in size and/or are far from the sample edge. However it will not always be possible to satisfy these requirements in full. To this end, a cloverleaf sample shape (figure 2.6) helps to minimize this error, by minimizing the influence of current paths flowing from within the sample to the sample edge[64]. Automated electrical conductivity measurements in this study were conducted using this cloverleaf structure. Any manual measurements were done using films deposited on glass rectangles. Note that manual measurements were only done on highly resistive samples, where the errors that the cloverleaf structure is designed to minimize are negligible.

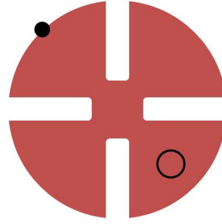

Figure 2.6: Cloverleaf structure with ideal (solid dot) and non-ideal (hollow dot) contact placement.

2.3.3 Hall Effect Mobility

The Hall effect describes the generation of a potential difference (via the Lorentz force) in a material along an axis that is perpendicular to both a current flow through the material, and an applied magnetic field. The Hall effect can be used to calculate charge carrier density for materials where the ideal field effect transistor equations cannot be used. The Hall effect is usually characterized using the Hall coefficient, R_H, which takes the form[64]

$$R_H = \frac{E_y}{J_x B_z}. \tag{2.20}$$

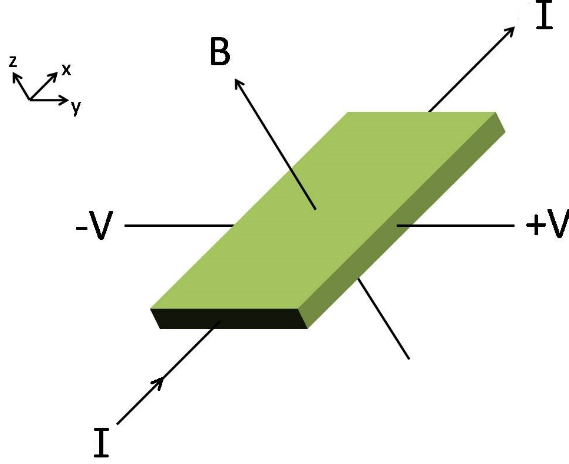

Figure 2.7: Geometry of a typical Hall effect measurement for an n-type material.

Here, E_y is the electric field created due to the current density J_x and magnetic field B_z along three mutually perpendicular axes. For a material in which there may be both holes and electrons acting as charge carriers, R_H takes the form

$$R_H = \frac{-n\mu_n^2 + p\mu_h^2}{q(n\mu_n + p\mu_e)^2}. \tag{2.21}$$

Here, n and p are the electron and hole concentrations, μ_n and μ_p are their mobilities, respectively, and q is the elementary charge. Previous studies[65] indicated that the materials studied here are doped primarily by oxygen vacancies, meaning that the majority mobile charge carriers are electrons. Therefore, the mixed metal oxides to be studied in this project are n-type. Making the assumption that $n >> p$, and combining equations (2.20) and (2.21) then

$$\frac{E_y}{J_x B_z} = \frac{-n\mu_n^2}{qn^2\mu_n^2} = \frac{-1}{nq} \tag{2.22}$$

and

$$n = \frac{-J_x B_z}{qE_y}. \tag{2.23}$$

Taking the current density J_x and the electron concentration n, the drift velocity v_d is

$$\frac{J_x}{n} = v_d. \tag{2.24}$$

Using the definition of mobility (the drift velocity achieved for a given electric field), the carrier concentration found earlier, the drift velocity and the applied electric field that yields J_x (the applied voltage over the length of the sample), one can find

$$v_{d_x} = \mu_n E_x, \tag{2.25}$$

and

$$\mu_n = \frac{J_x}{nE_x} = \frac{-qE_y}{B_z E_x}. \tag{2.26}$$

Using this, the carrier mobility can be determined for films at most stoichiometries, assuming the sample is conductive enough for a current to be applied. This technique is useful in samples for which the field effect mobility cannot be determined.

2.3.4 Charge Carrier Density

In the case of materials where conductivity is not modulated by an applied gate voltage, the Hall effect mobility may be combined with the resistivity obtained via a sheet resistance measurement. Using the thickness of the film d_f and the equation for electrical conductivity

$$\sigma = \mu n q, \tag{2.27}$$

the sheet resistance and Hall mobility can be substituted to give

$$\frac{1}{R_S d_f} = \mu_n n q. \tag{2.28}$$

Solving for the carrier concentration n yields

$$n = \frac{\mu R_S d_f}{q}. \tag{2.29}$$

By comparing samples annealed under oxygen, it is possible to observe the extent to which oxygen vacancies contribute to the conductivity of the materials.

2.4 Thermal Conductivity

For materials that can be fabricated into large, free-standing structures, measurement of thermal conductivity can be relatively simple. In previous work that examined thermal conductivity as a function of stoichiometry in ZIO, the samples were individually sintered ceramic (i.e. large) solids[66, 67]. However, since this project is centered around the creation of sputtered thin-films, and the resulting material will be of a different internal physical structure than the sintered samples, a different relationship between stoichiometry and the thermal and electrical characteristics of the material is expected. Since the thermal conductivity as a function of fabrication parameters will need to be determined, but the material in question is composed of films only a few thousand Angstroms thick, an indirect approach to thermal conductivity determination is necessary.

2.4.1 The 3ω Method

While there are new techniques such as thermoreflectance[68, 69] being explored for the measurement of thermal conductivity in thin films, the most common and accurate method used is known as 3ω[70]. This technique involves the fabrication of a thin metal strip on the surface of the film, to which an AC current is applied. This strip acts not only as a heater but also as a thermometer, by measuring the voltage at two points along this strip and observing the amplitude of the first and third harmonics using a lock-in amplifier.

A time-varying current is applied to the heater strip, of the form

$$I(t) = I_o cos(\omega t). \tag{2.30}$$

The temperature of the heater will vary with the applied power

$$P = I^2 R, \tag{2.31}$$

and using the resistance of the heater R_h, the temperature T will vary as

$$\Delta T \propto I_o^2 R_h cos^2(\omega t). \tag{2.32}$$

This can be rewritten in terms of constant and time-varying components, using a trigonometric identity

$$\Delta T \propto \frac{I_o^2 R_h}{2} + \frac{I_o^2 R_h cos(2\omega t)}{2}. \tag{2.33}$$

The temperature will depend on a DC component and an AC component at frequency 2ω, and is expressed as

$$\Delta T = \Delta T_{DC} + T_{2\omega} cos(2\omega t). \tag{2.34}$$

The resistance of the heater is temperature dependent, and will take the form

$$R_h = R_o(1 + C_{RT}\Delta T), \tag{2.35}$$

where R_o is the resistance with no heating and C_{RT} is the temperature coefficient of resistance. Using ΔT in equation (2.34) and substituting it into the equation for the resistance of the heater, one obtains

$$R_h(t) = R_o + R_o C_{RT}(\Delta T_{DC} + T_{2\omega} cos(2\omega t)) \tag{2.36}$$

and, expanded

$$R_h(t) = R_o + R_oC_{RT}\Delta T_{DC} + R_oC_{RT}T_{2\omega}cos(2\omega t). \tag{2.37}$$

The voltage measured across the strip will depend on R_h(t) and I(t) such that

$$V(t) = I(t)R_h(t) \tag{2.38}$$

$$V(t) = [I_ocos(\omega t)][R_o + R_oC_{RT}\Delta T_{DC} + R_oC_{RT}T_{2\omega}cos(2\omega t)] \tag{2.39}$$

$$V(t) = I_oR_ocos(\omega t) + I_oR_oC_{RT}\Delta T_{DC}cos(\omega t) + I_oR_oC_{RT}T_{2\omega}cos(2\omega t)cos(\omega t) \tag{2.40}$$

and finally

$$V(t) = I_oR_o[cos(\omega t) + C_{RT}\Delta T_{DC}cos(\omega t) + C_{RT}T_{2\omega}cos(2\omega t)cos(\omega t)]. \tag{2.41}$$

Applying

$$cos(A)cos(B) = \frac{cos(A-B) + cos(A+B)}{2} \tag{2.42}$$

to equation (2.41), $V(t)$ is found to be[71]

$$V(t) = I_oR_o\left[cos(\omega t) + C_{RT}\Delta T_{DC}cos(\omega t) + C_{RT}T_{2\omega}\frac{cos(\omega t)}{2} + C_{RT}T_{2\omega}\frac{cos(3\omega t)}{2}\right]. \tag{2.43}$$

The voltage of the heater therefore has 1ω and 3ω components. Since the 1ω voltage will vary due to the applied current, the effect on voltage from the temperature amplitude will not be apparent. However, the 3ω component can be isolated using a lock-in amplifier. Looking only at the 3ω component yields

$$V_{3\omega} = \frac{I_oR_oC_{RT}T_{2\omega}}{2} = \frac{V_{1\omega}C_{RT}T_{2\omega}}{2}. \tag{2.44}$$

Solving for the temperature amplitude at 2ω results in a simple expression of the

form[71]

$$T_{2\omega} = \frac{2V_{3\omega}}{C_{RT}V_{1\omega}} = T_{meas}. \tag{2.45}$$

2.4.2 Analysis of 3ω Data

For a heater on a semi-infinite slab with thermal conductivity κ_s, the temperature measured will be T_s[71], and will take the form

$$T_s = \frac{P}{\pi l \kappa_s}\left[0.5ln\left(\frac{\alpha}{b^2}\right) - 0.5ln(2\omega) + \zeta\right] - i\frac{P}{4l\kappa_s}. \tag{2.46}$$

Here, α is the thermal diffusivity of the substrate, b is the half-width of the heater strip, l is the length of the heater, P is the applied RMS AC power, and ζ is an empirically determined value close to 1[71, 72]. This equation consists of a frequency-dependent in-phase component and a frequency-independent out-of-phase component.

If there is a thin film of thickness d_f between the heater and the substrate, and the heater has a width that is significantly greater than the thickness of the film, then there will be an in-phase, frequency-independent increase in the temperature amplitude which is inversely proportional to the film thermal conductivity κ_f, and the resulting measured temperature will be[71]

$$T_{meas} = T_s + \frac{Pd_f}{2bl\kappa_f}. \tag{2.47}$$

It is convenient to express the power in terms of $V_{1\omega}$ and the heater resistance R. Substituting $P = \frac{V_{1\omega}^2}{R}$ and combining equations (2.46) and (2.47) yields

$$V_{3\omega} = \frac{C_{RT}V_{1\omega}^3}{2R\pi l\kappa_s}\left[0.5ln\left(\frac{\alpha}{b^2}\right) - 0.5ln(2\omega) + \zeta\right] - i\frac{C_{RT}V_{1\omega}^3}{8Rl\kappa_s} + \frac{C_{RT}V_{1\omega}^3 d_f}{4Rbl\kappa_f}. \tag{2.48}$$

It is clear that both the real and imaginary components of $V_{3\omega}$ are linearly related to $V_{1\omega}^3$. This relationship serves as a useful tool for eliminating the influence of any

systematic errors in the measurement system. To do this, the derivative of $V_{3\omega}$ with respect to $V_{1\omega}^3$ gives

$$\frac{dV_{3\omega}}{dV_{1\omega}^3} = \frac{C_{RT}}{2R\pi l\kappa_s}\left[0.5ln\left(\frac{\alpha}{b^2}\right) - 0.5ln(2\omega) + \zeta\right] - i\frac{C_{RT}}{8Rl\kappa_s} + \frac{C_{RT}d_f}{4Rbl\kappa_f}. \quad (2.49)$$

It is convenient at this point to express the slope in terms of a temperature per unit power, so devices with different R and C_{RT} can be compared. Multiplying the slope by $\frac{2R}{C_{RT}}$ yields an equation equivalent to the combination of equations (2.46) and (2.47), giving a result of

$$\left(\frac{2R}{C_{RT}}\right)\frac{dV_{3\omega}}{dV_{1\omega}^3} = \frac{1}{\pi l\kappa_s}\left[0.5ln\left(\frac{\alpha}{b^2}\right) - 0.5ln(2\omega) + \zeta\right] - i\frac{1}{4l\kappa_s} + \frac{d_f}{2bl\kappa_f} = \frac{T_{meas}}{P}. \quad (2.50)$$

There are two options for finding a value for the substrate thermal conductivity κ_s. The simplest is to look only at the out-of-phase component of the $V_{3\omega}$ signal, using the relation

$$\kappa_s = \frac{C_{RT}}{8Rl\left(i\frac{dV_{3\omega}}{dV_{1\omega}^3}\right)}. \quad (2.51)$$

The accuracy of κ_s when determined using this method tends to be poor, as the imaginary component of the $V_{3\omega}$ signal is very small. The original 3ω publication[70] also reports unreliability using this method.

The other method for determining the substrate thermal conductivity is examining the linear relationship between $\frac{dV_{3\omega}}{dV_{1\omega}^3}$ and $ln(2\omega)$ where

$$\frac{d^2V_{3\omega}}{dV_{1\omega}^3 dln(2\omega)} = -\frac{C_{RT}}{4R\pi l\kappa_s} \quad (2.52)$$

and solving for κ_s yields

$$\kappa_s = -\frac{C_{RT}}{4R\pi l\frac{d^2V_{3\omega}}{dV_{1\omega}^3 dln(2\omega)}}. \quad (2.53)$$

If the thickness of the film being studied is known and measurements can be taken at multiple thicknesses, one can take advantage of this known variation in film thickness to increase the accuracy of any measurement of that film's thermal conductivity. It is possible to solve for κ_f by taking the derivative of equation (2.50) with respect to the film thickness d_f which gives

$$\frac{d}{d_f}\left(\frac{R}{C_{RT}}\frac{dV_{3\omega}}{dV_{1\omega}^3}\right) = \frac{1}{4bl\kappa_f} \quad and \quad \kappa_f = \frac{1}{2bl\frac{d}{dd_f}\left(\frac{T_{meas}}{P}\right)}. \tag{2.54}$$

Additionally, by subtracting the zero-thickness intercept of $\frac{d}{dd_f}\left(\frac{T_{meas}}{P}\right)$ from $\frac{T_{meas}}{P}$, the influence of the substrate, interfaces, and any additional films can be removed. However, in experiments that use a combinatorial range of stoichiometries, taking a derivative with respect to d_f will not be possible. In these cases data from two identical heaters, one with the film of interest and one without, will be compared.

2.4.3 Thermal Penetration Depth

Use of the 3ω method in the manner described requires that certain conditions be met. To increase the accuracy of equation (2.46), the thermal penetration depth in the substrate, d_t, should be several times larger that the heater half width. For the substrate to be considered 'semi-infinite', the substrate should be several times thicker than d_t.[71] The thermal penetration can be calculated using[71]

$$d_t = \sqrt{\frac{\alpha_S}{2\omega}}, \tag{2.55}$$

where α_S is the thermal diffusivity of the substrate and ω is the first harmonic frequency of the applied AC signal. These conditions constrain the choice of heater width, the choice of substrate, and the frequency range over which measurements can reliably be taken.

2.4.4 Interfacial Thermal Resistance

The flow of heat from one material to another is impeded by a thermal resistance at the interface between the two materials. This interfacial resistance usually behaves as a fixed thermal resistance, and can be modelled in the same manner as a layer, introducing a fixed, in-phase increase in the measured temperature amplitude. It is often observed[73, 74, 75, 72] that the measured thermal conductivity of thin films tends to decrease at low film thicknesses. However, it has been shown both here and in other studies[75] that this might also be explained for some materials by using equation (2.47) by assuming a constant film thermal conductivity, and a fixed thermal resistance R under the film of interest. For a system with a single film between heater and substrate, this relation takes the form[71]

$$T_{meas} = T_s + \frac{Pd_f}{2bl\kappa_f} + \frac{RP}{2bl}. \tag{2.56}$$

2.5 The Seebeck Effect

Having measured the electrical conductivity σ and the thermal conductivity κ, the final component of the thermoelectric figure of merit is the Seebeck coefficient. This describes the ratio between the potential and temperature gradients in a material and is usually expressed as

$$S = \frac{\nabla V}{\nabla T} = \frac{E}{\nabla T}. \tag{2.57}$$

A temperature gradient results in a majority of phonons in the material travelling from the hot side to the cold side of the sample. The interaction between phonons and free carriers in the material (phonon drag) results in the movement of mobile charge carriers in the same direction. Therefore, in an n-type material there will be an excess of electrons on the cold side, resulting in an electric field pointing from hot to cold. The direction of this electric field will be reversed in the case of a p-type

device, where phonon drag causes a buildup of holes. At equilibrium, the current due to phonon drag will be equal and opposite to the current due to the electric field. More explicitly, the absolute thermopower of a material is[76]

$$S = \frac{-L_{12}}{qTL_{11}}. \tag{2.58}$$

Here L_{12} is the kinetic coefficient describing the interaction between charge carriers in a material and a temperature gradient in that material, while L_{11} describes the relationship between those charge carriers and a potential gradient[76]. A stronger interaction between phonons and free charge carriers (larger L_{12}) in a material will result in a higher current at equilibrium, and a larger Seebeck coefficient.

Typically, the Seebeck coefficient is measured directly, by determining the temperature difference between two points on a sample as well as the voltage between those two points. However, this measurement is complicated by the need to remove the influence of the Seebeck effect of the materials in the instrument used to take the measurement.

2.6 Origin of the Thermoelectric Figure of Merit

The thermodynamic efficiency of any device can be described as the the ratio of power output of the device to the power input. Specifically, the efficiency is

$$\eta = \frac{P_{out}}{P_{in}}. \tag{2.59}$$

The power generated by a thermoelectric device can be described using the current flow I, and the resistance of the load R_L to yield

$$P_{out} = I^2 R_L. \tag{2.60}$$

It should be noted that a thermoelectric generator will employ both n and p-type 'legs', arranged (electrically) in series. Therefore the total Seebeck voltage is the sum

of the Seebeck effect in both types of material. For example, the total Seebeck voltage (V_S) for a device with n and p legs will be

$$V_S = S_p \Delta T + S_n(-\Delta T) = \Delta T(S_p - S_n) = \Delta T\overline{S}. \tag{2.61}$$

For the purposes of calculating Seebeck voltages in a thermoelectric device employing both n and p materials, it is useful to consider this combined Seebeck coefficient $\overline{S} = S_p - S_n$.

The power into the device is the heat flux at the hot side of the device. There are three components to consider: heat flow due to the applied temperature gradient (Q_{flow}), the heat absorbed to offset the cooling produced at the junction between the n and p materials due to the Peltier effect (Q_{pelt}), and the heat generated in the device due to Joule heating (Q_{joule}). The heat flow can be described using ΔT, the thermal conductivity of the n and p materials, their cross sections A_n and A_p, and their lengths l_n and l_p. The flow is then described by

$$Q_{flow} = \Delta T\left(\frac{\kappa_n A_n}{l_n} + \frac{\kappa_p A_p}{l_p}\right). \tag{2.62}$$

The Peltier effect describes cooling at the interface between two conducting materials between which a current is flowing. Heat generated at the junction in this case is $I(\Pi_p - \Pi_n)$ where I flows from the p leg to the n leg. The Peltier coefficient Π of a material is equivalent to the product of that material's Seebeck coefficient and the temperature, so $\Pi = TS$. Heat produced due to the Peltier effect is then

$$Q_{pelt} = I(S_p - S_n)T = I\overline{S}T. \tag{2.63}$$

The Joule heating in the device can be described using the internal resistance R_{in} and the current. Half of this heat will flow out through the hot side of the device, introducing a negative term in the flux which yields

$$Q_{joule} = -\frac{1}{2} I^2 R_{in}. \tag{2.64}$$

Now P_{in} can be expressed as

$$P_{in} = Q_{flow} + Q_{pelt} + Q_{joule} = \Delta T \left(\frac{\kappa_n A_n}{l_n} + \frac{\kappa_p A_p}{l_p} \right) + I\overline{S}T - \frac{1}{2} I^2 R_{in}. \tag{2.65}$$

Using this, the efficiency η can be determined to be

$$\eta = \frac{I^2 R_L}{\Delta T(\frac{\kappa_n A_n}{l_n} + \frac{\kappa_p A_p}{l_p}) + I\overline{S}T - \frac{1}{2} I^2 R_{in}} = \frac{I R_L}{\frac{\Delta T}{I}(\frac{\kappa_n A_n}{l_n} + \frac{\kappa_p A_p}{l_p}) + \overline{S}T - \frac{1}{2} I R_{in}}. \tag{2.66}$$

It is useful to express the internal resistance R in terms of the individual resistances of the n and p components, using their conductivities σ_n and σ_p as well as their cross-sectional areas (A_n and A_p) and thicknesses (l_n and l_p), resulting in

$$R = R_{in} + R_L = \frac{l_n}{\sigma_n A_n} + \frac{l_p}{\sigma_p A_p} + R_L. \tag{2.67}$$

To get maximum power to the load, the internal resistance of the thermoelectric device should be equal to the load resistance, allowing R and R_L to be rewritten as

$$R_L = R_{in} = \frac{R}{2} = \frac{l_n}{\sigma_n A_n} + \frac{l_p}{\sigma_p A_p}. \tag{2.68}$$

The current can then be written as

$$I = \frac{V}{R} = \frac{\Delta T \overline{S}}{2 R_L} = \frac{\Delta T \overline{S}}{2(\frac{l_n}{\sigma_n A_n} + \frac{l_p}{\sigma_p A_p})}. \tag{2.69}$$

Substituting this into equation (2.66), the efficiency is

$$\eta = \frac{\frac{\Delta T\overline{S}}{2}}{\frac{2\Delta T\left(\frac{l_n}{\sigma_n A_n}+\frac{l_p}{\sigma_p A_p}\right)\left(\frac{\kappa_n A_n}{l_n}+\frac{\kappa_p A_p}{l_p}\right)}{\Delta T\overline{S}} + \overline{S}T - \frac{1}{4}\Delta T\overline{S}} = \frac{\Delta T}{4\frac{\left(\frac{\kappa_n}{\sigma_n}+\frac{l_n\kappa_p A_p}{\sigma_n A_n l_p}+\frac{l_p\kappa_n A_n}{\sigma_p A_p l_n}+\frac{\kappa_p}{\sigma_p}\right)}{\overline{S}^2} + 2T - \frac{1}{2}\Delta T}. \tag{2.70}$$

Is it clear that for maximum power to the load, the efficiency will be maximized with respect to the dimensions of the n and p legs when these physical dimensions are selected to minimize the left-hand term in the denominator. This condition is satisfied for the relation[34]

$$\frac{l_n A_p}{l_p A_n} = \sqrt{\frac{\sigma_n\kappa_n}{\sigma_p\kappa_p}}. \tag{2.71}$$

Applying this relation to the efficiency, η is found to be

$$\eta = \frac{\Delta T}{4\frac{\left(\frac{\kappa_n}{\sigma_n}+2\sqrt{\frac{\kappa_p\kappa_n}{\sigma_p\sigma_n}}+\frac{\kappa_p}{\sigma_p}\right)}{\overline{S}^2} + 2T - \frac{1}{2}\Delta T} = \frac{\Delta T}{4\frac{\left(\sqrt{\frac{\kappa_n}{\sigma_n}}+\sqrt{\frac{\kappa_p}{\sigma_p}}\right)^2}{\overline{S}^2} + 2T - \frac{1}{2}\Delta T} = \frac{\Delta T}{\frac{4}{Z} + 2T - \frac{1}{2}\Delta T}. \tag{2.72}$$

At any given temperature T the efficiency of a thermoelectric device will be maximized by increasing ΔT and Z. The thermoelectric figure of merit given here is a combined value for both n and p materials, namely

$$Z = \frac{\overline{S}^2}{(\sqrt{\frac{\kappa_n}{\sigma_n}} + \sqrt{\frac{\kappa_p}{\sigma_p}})^2} = \frac{(S_p - S_n)^2}{(\sqrt{\frac{\kappa_n}{\sigma_n}} + \sqrt{\frac{\kappa_p}{\sigma_p}})^2}. \tag{2.73}$$

When considering only a single type of material, a similar figure of merit for a single material is used,

$$Z = \frac{S^2\sigma}{\kappa}. \tag{2.74}$$

2.7 The Wiedemann-Franz Law

The electrical conductivity and thermal conductivity of a given material are not independent of one another, due to the fact that the thermal conductivity κ is in fact the sum of heat conducted by charge carriers (κ_e) and by phonons (κ_p), meaning

$$\kappa = \kappa_p + \kappa_e. \tag{2.75}$$

In an electrical insulator, κ is dominated by κ_p as carrier concentrations and/or mobility are too low for a significant amount of heat to be transported by charge carriers. In a metal however, the carrier concentration is very high, and κ_e tends to dominate with most heat carried by charge carriers. In this case, the amount of heat transported by a charge carrier is dependent only on temperature, and the amount of charge transported by the carrier is fixed. In the 'ideal metal' extreme, heat is assumed to only be carried by these charge carriers (i.e. $\kappa \approx \kappa_e$) and the ratio of the thermal conductivity to the electrical conductivity is a function of only temperature, so[77]

$$\frac{\kappa}{\sigma} = LT, \tag{2.76}$$

where L is the Lorenz number which, in this ideal case, is 2.45 x 10^{-8} $\frac{W\Omega}{K^2}$[77]. Calculation of the Lorenz number (i.e. using κ and σ to find an effective Lorenz number L_{eff}) generally results in a number near this value for metals. Since κ is generally greater than κ_e in semiconductors, however, L_{eff} is often significantly higher and semiconductors fail to conform to the Wiedemann Franz law. However, the effective Lorenz number is nevertheless a useful empirical value, as it provides a means for describing the degree to which a given material is behaving (thermally and electrically) like a metal.

Chapter 3

Sample Fabrication

3.1 RF Sputtering

All of the materials of interest in this study were thin films created using RF sputtering. Sputtering is commonly used for the deposition of thin films[78], and a system for the combinatorial deposition of thin films was available for use via the Institute for Research in Materials.

3.1.1 Theory

Sputtering is an event in which an atom or atoms are ejected from the surface of a bulk sample of material (a 'target') due to a relatively high-energy collision between a particle and the sample. Sputtering can be used for etching, in which the bulk material is eroded by repeated collisions, and for deposition, in which material ejected from the target is deposited onto a nearby substrate.

Sputtering is conducted under partial vacuum, with a chosen sputter gas introduced to the vacuum chamber at a pressure on the order of 1 mTorr. The target material is placed over a charged electrode, the electric field from which accelerates ions in the sputter gas toward the target surface, while free electrons are accelerated away from the target surface. Collisions involving these electrons serve to further ionize the gas. However, in the electrode-only configuration, they can also collide with the nearby substrate, damaging the deposition surface (or newly-sputtered material). The use of a magnetron, in which permanent magnets are coupled with the electrode, helps to mitigate this problem. Magnetic field lines with a vector component parallel to the plane of the target surface cause the path of electrons moving away from the

target to curve, trapping them near the target surface. This also results in greater ionization of the gas near the target, increasing the sputtering rate. As ions impact the target surface, material is ejected and deposited onto a substrate placed nearby. If the target material is conductive, a constant DC field from the magnetron can be used. However, for insulating films an RF supply can be used to power the magnetron. The oscillating field prevents a buildup of charge on the target that would serve to repel ions and lower the sputtering rate.

3.1.2 Sputtering Conditions Used

50 mm diameter targets of zinc oxide and indium(III) oxide (both purchased from Kurt J. Lesker Co.) and of tin(IV) oxide (purchased from Williams Advanced Materials) were used as sputtering sources in this experiment. These were mounted to copper plates which were the fixed over the magnetrons. In some conditions the gas used was 100% argon, while others used a 10% or 20% partial pressure of oxygen as well. The sputter gas pressure was 5 mTorr for all conditions.

The sputtering rates varied significantly between the three targets used, and they were also strongly affected by the presence of oxygen in the sputter gas. Powers applied varied from 40 W to 110 W depending on the combination of targets chosen and all sputtering was done using RF supplies at 13.56 MHz.

3.1.3 Deposition of Combinatorial Films

In order to create films whose composition varies as a function of position, a combinatorial sputtering technique[79] was used in which the sample substrates are affixed to a circular rotating 'table'. The rotation of the table results in a 75 mm toroidal 'track' of sputtered material, and allows the substrates to pass by multiple sputtering targets, ideally with only a sub-monolayer amount of material deposited on each pass. This ensures an intimate mixing of the target materials on the substrate surface.

In order to modulate the deposition rate as a function of position on the sample,

an aluminum 'tunnel' was placed over each target, with the target at one end and an aluminum 'mask' at the other, whose opening varies as a function of radial position relative to the table. A 'linear out' mask, for example, will have a narrow opening near the inner edge of the track, and a wide opening near the outer edge of the track. On the other hand, a 'linear in' mask will have the opposite arrangement. The edges of these openings are not linear, but rather are designed such that a substrate passing by the target will have a 'wedge' of material deposited it that varies in thickness as a function of radial position. Specifically, the shapes ensure that the fraction of time each radial distance on the table is 'exposed' to the sputtering target varies linearly (or inversely, in the case of 'linear in' masks) with radial position. The shape also compensates for the known variation in deposition rate across the surface of a sputtering target.

In most conditions the zinc oxide target was masked 'linear out', while the tin oxide or indium oxide target was masked 'linear in'.

3.1.4 Stencil Masks

For both the transistor and thermoelectric portions of the experiment, it was necessary to pattern the sputtered films. It was initially hoped that this patterning could be accomplished post-sputtering using the wet-etch process detailed in section 3.3.1. However, this method caused a number of problems and all data reported here were derived from samples that were patterned using laser-cut stainless steel stencil masks.

For thin-film transistors this mask was relatively simple, consisting only of a large number of rectangular openings. Transistors were created using the resulting rectangular pads of sputtered material. Electrically isolating each device in this way served to improve yields and eliminate 'fringing' effects where current paths through the semiconductor are available outside the physical 'channel' between the drain and source contacts of the device. These extra conduction paths serve to lower the accuracy of any use of the ideal field effect transistor equations, as the equations depend on precise measures of channel width and length.

For the thermoelectric portion of the study the mask design in figure 3.1 was used. There are three types of ‘opening’. The ‘cloverleaf’ shapes were used for van der Pauw sheet resistance and Hall effect measurements. The column of small, rectangular openings was used for individual, ‘manual’ 3ω measurements, while the large rectangular column was used for automated 3ω measurements. The blank area next to the large rectangular opening provides a ‘reference’ area. Data from 3ω heaters on the film were compared to data for 3ω heaters in this blank area, and the difference in temperature amplitude between these heaters was taken to be due to the presence of the sputtered film.

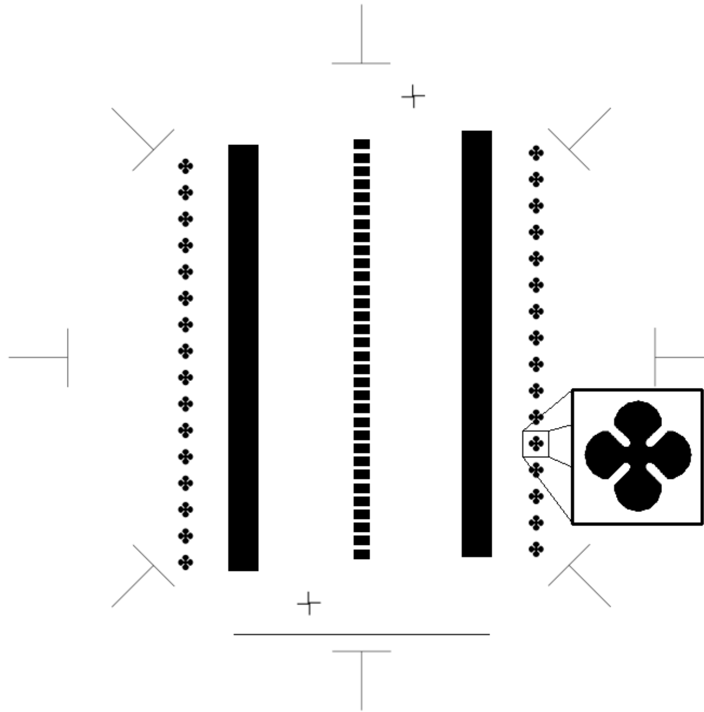

Figure 3.1: Design for stencil masks used to pattern the films during sputtering. The mask is ‘open’ in the black areas, resulting in film being deposited in those locations. A set of alignment markers can be seen around the perimeter of the design. A magnified cloverleaf is shown (inset).

To ensure that unintentional sputtering of the mask material was not contaminating the sputtered films, WDS mode electron microprobe measurements (section

4.2.1) of films sputtered through the stainless steel stencil masks were made. These measurements revealed no detectable presence of iron in the films.

3.2 Annealing

Films were annealed using a Modular Process Technology RTP-600S rapid thermal annealer. This system allowed for computer-controlled regulation of temperature, temperature ramp rate and gas flow rate during annealing. While a number of different gases and temperatures were used, there were a number of elements common to all annealing steps.

Samples, whether silicon wafers, silicon strips or glass, were placed on a 150 mm silicon wafer. Using 0.5 cm tall glass cylinders, a second 150 mm wafer was placed above the first. These were placed in the chamber on the tips of three quartz glass arms. The temperature was measured using a thermocouple in direct contact with the bottom of the lower wafer.

Prior to heating, the chosen gas was flushed through the annealing chamber at a rate of 10 sccm for ten minutes. Once annealing began, this rate was lowered to 2 sccm for the remainder of the annealing process. A temperature ramp rate of 5°C/s was used regardless of the eventual plateau temperature chosen. Once reached, this plateau temperature was maintained for 30 minutes, after which all heating was removed and the sample was allowed to cool. The sample was not removed from the chamber until the temperature was below 30°C, usually taking at least fifteen minutes.

It should be noted that only silicon substrates were used for samples annealed at 600°C, as glass samples were found to soften significantly at this temperature. This softening posed a risk of contamination not only to the film on the glass, but also to nearby samples due to potential outgassing of unknown materials in the glass.

3.3 Photolithography

3.3.1 Etching the Films

Individual sputtered 'pads' of the films of interest were created for the transistor part of this project using a stainless steel stencil mask that was fixed over the silicon wafers during sputtering using copper tape. While this method produced acceptable results, it was hoped that a fully photolithographic patterning method could be used in the thermoelectric part of the project. The wafers would be fully covered in sputtered film, which would then be patterned using a positive photoresist (positive photolithogrpahy[80]) and a wet etch. This would produce 'sharper' edges than stencil masks.

MicroChem Megaposit SPR-220 positive photoresist was used in a pattern similar to figure 3.1. To etch the films a number of combinations of etchants were tried, including hydrochloric acid and Transene TE-100, a commercial tin-oxide etchant. It was found that the zinc oxide-rich area of the films tended to etch extremely quickly, requiring less than ten seconds in 3% HCl to fully etch 200 nm of sputtered film. However, at the tin oxide-rich end of the sample the etch rates were two to three orders of magnitude lower. This resulted in significant over-etching (under-cutting) in some areas, while others remained largely un-patterned. While indium oxide was found to etch at a rate that was more compatible with that of zinc oxide, the over-etching of zinc oxide-rich films was still present, albeit to a lesser degree.

A two-step etching process was tested to address this problem. Zinc oxide was etched in very dilute (0.1%) HCl. The photoresist was then removed, and the wafer was patterned again, with the areas that had been previously etched covered entirely by photoresist. While this method produced useable results across most of the sample, films at the 'transistion' between the two regions provided unreliable results. It was decided that stencil masks would result in more reliable, if less precise, patterning of the films.

3.3.2 Lift-off Patterning of Metal

To pattern the metal contacts, heaters, sense lines and current buses in both the transistor and thermoelectric parts of the project, a lift-off photolithography procedure[80] was used.

Lift-off involves the application of photoresist to an entire sample, prior to the application of the material to be patterned. It is exposed through a photomask with a 'positive' print of the desired design. The sample is then immersed in a developer that removes any unexposed resist, leaving the surface below the photoresist exposed. Material is then applied to the entire surface. When the sample is placed in a resist remover, the photoresist dissolves, lifting off any material that had not adhered directly to the sample.

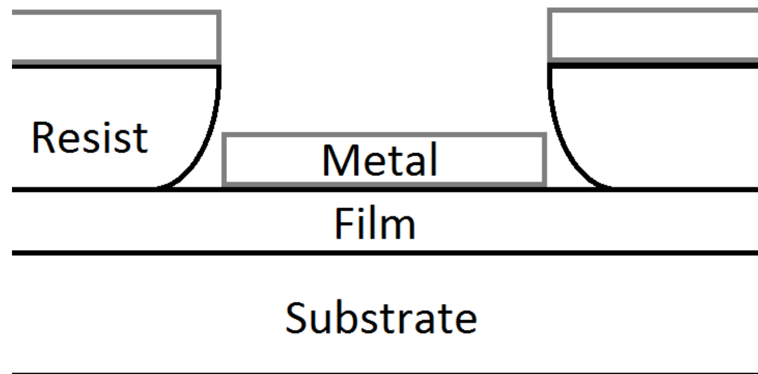

Figure 3.2: Cross section after metal application, but before removal of the remaining resist.

Futurrex NR9-1000PY photoresist was used in this experiment. This resist is designed to create a 're-entrant profile' (visible in figure 3.2) when exposed and developed, creating a vertical gap between metal deposited on the resist and metal deposited on the substrate. This creates sharper edges in the final pattern, as well as making the lift-off process faster.

3.4 Deposition of Insulating and Metal Films

Insulating Al_2O_3 films, as well as the metal used for the heaters, sense lines, contact pads and current buses, were deposited using electron beam evaporation. This was done using an MDC Vacuum e-Vap Mighty Source evaporator, and film thicknesses were monitored using a Sycon quartz crystal monitor.

While most films were deposited using e-beam evaporation, some aluminum films were thermally evaporated using a tungsten filament. It was found that aluminum in the e-beam evaporator tended to damage the crucible liner very quickly, jeopardizing the evaporator itself.

3.4.1 Al_2O_3 Films

99.99% Al_2O_3 source material was acquired from Kurt Lesker, in the form of ∼2 mm sized pieces. Al_2O_3 was selected due to its relatively high thermal conductivity (50 W/m·K in single crystal form[81]), minimizing the contribution of the insulating film to the measured temperature amplitude of heaters deposited on it, as well as its compatibility with electron beam deposition.

Prior to application of the insulating film, each group of 'cloverleaf' sputtered film structures were covered with a strip of aluminum foil which was affixed to the back of the wafer using double-sided copper tape.

During evaporation, the sample was rotated to reduce the likelihood of the creation of pinhole defects in the insulating film through which the metal structures might electrically connect to the sputtered films. Evaporation was done at a rate of approximately ∼0.1 nm/s, to a total thickness of 400 nm. It was found that application of the electron beam to the Al_2O_3 source material caused a gradual rise in pressure, and it was therefore necessary to complete the deposition in stages, during which the pressure would rise to close to 5×10^{-6} Torr, as ∼100 nm of film was deposited. Upon reaching this pressure the beam current (and therefore the deposition rate) was reduced and the pressure was allowed to drop back to below 10^{-6} Torr. To

ensure a consistent rate of deposition and ensure that all material in the crucible was being used, the electron beam was ‘scanned’ over the source material in the crucible in an approximately circular pattern.

It should be noted that it was not generally necessary to break vacuum between the various stages of Al_2O_3 deposition, and it is therefore assumed that an un-contaminated surface of Al_2O_3 was present at the beginning of each subsequent deposition stage and that no interfacial thermal resistance exists between adjacent Al_2O_3 layers.

3.4.2 Nickel Adhesion

Both nickel and aluminum are commonly used metals for 3ω experiments. Early samples in this study were made with aluminum, as this was the metal used in the transistor phase of the experiment. However, third harmonic voltage measurements were affected by a non-ohmic contact resistance between the aluminum and both the tungsten probes and ‘zebra’ connectors used to contact the wafer in early versions of the combinatorial measurement system. Nickel was chosen to replace aluminum as it eliminated this contact problem.

Nickel generally adheres poorly to oxides, and would often peel away from the substrate during the removal of the lift-off resist. To combat this problem a number of samples were made using a 5 nm thick chromium adhesion layer between the nickel and the substrate. This layer served to help bind the nickel to the underlying oxide. While this method was successful in preventing the nickel from delaminating from the substrate, it also made the resulting 3ω data somewhat unreliable. Specifically, while the relationship between $V_{3\omega}$ and $ln(2f)$ was linear for all heaters, and produced values for the substrate thermal conductivity that matched literature, this was only true for relatively small applied powers ($\leqslant$10 mW). For higher powers of $\sim$30 mW, the scatter in substrate thermal conductivity was greatly increased, with an average value that was low by $\sim$50% (i.e. at 10 mW substrate thermal conductivity was calculated to be within 10% of the literature value for silicon of 142 W/m·K[82], while at 30 mW

the substrate thermal conductivity was calculated to be 70-80 W/m·K, when using nickel with a chromium binding layer.)

In order to promote nickel adhesion to the substrate without the use of a chromium binding layer, samples were allowed to sit in atmosphere post-nickel-deposition for an extended period of time to allow nickel to bind to the surface. This effect has been demonstrated[83] in the literature. It was also discovered that if the sample was not allowed to cool slowly, differential contraction while cooling would cause the film to 'buckle' on the surface of the wafer. Therefore samples were allowed to cool for at least four hours in vacuum before being removed to atmosphere, where they were allowed to sit for at least 16 hours prior to further fabrication steps.

3.4.3 Aluminum

While some of the data reported here were taken using nickel heaters (none of which had the chromium binding layer underneath), a number of samples were made using aluminum; the switch from 'zebra' connectors to pogo pins for contacting the wafer made the use of nickel unnecessary, as the gold-plated pogo pins made contact with the aluminum contact pads without the non-ohmic contact resistance observed when using zebra connectors. Switching to aluminum also eliminated the need for the long cooling phase and atmospheric exposure phases, greatly reducing sample fabrication time.

Chapter 4

Physical Characterization

4.1 Film Thickness

The measured thickness of the films is necessary for the calculation of electrical and thermal conductivity. The thickness can also be used in concert with mass disk data (section 4.2.2) to calculate the bulk density of the sputtered film. This information, relative to the bulk density of the source materials, can help shed light on the structure of sputtered films. Thickness is also useful when analyzing the on/off ratio of transistors using the films as a semiconductor, as leakage currents when 'off' will generally increase with film thickness.

4.1.1 Profilometry

In both the transistor and thermoelectric parts of these experiments, a Dektak profilometer was used to determine film thickness. This device drags a needle of a given size and downward force across the surface of the sample, and records the film thickness as a function of position.

This measurement was typically done on films sputtered onto silicon strips. Part of each strip was masked with a piece of copper tape, creating a 'step' from film onto bare silicon that extended over the entire width of the sputtering track. Measurements were taken across this step, and the step height was measured and recorded as a function of radial position on the table.

4.1.2 Ellipsometry

Data collected using profilometry tended to produce results with a large amount of scatter, as much as $\pm$ 50 nm for a step height of as little as 250 nm. By comparison, scatter using ellipsometry for films with thicknesses on the order of a few hundred nm was less than 10%. Ellipsometry is a technique in which light of a known polarization is incident on a surface, and the intensity and polarization of the specularly reflected light is recorded. This measurement is typically recorded by taking individual intensity measurements through a linear polarizer in a number of different orientations, providing the necessary information to reconstruct the elliptical polarization of the reflected light.

The angle between the polarizations of the reflected light relative to the incident light (Δ), and the ratio of the intensity of the parallel 'p' polarization to the perpendicular 's' orientation ($\frac{|R_p|}{|R_s|} = tan(\psi)$[84]) yields the complex reflection coefficients for the interface from which the light was reflected. This ratio is equivalent to the ratio of the Fresnel reflection coefficients. Since these coefficients are complex numbers, their ratio is as well, giving both amplitude and phase information. The output of any ellipsometric measurement at a given wavelength is generally expressed in the form of a complex ration of the reflection coefficients[84]

$$\Theta = \frac{R_p}{R_s} = tan(\psi)e^{-i\Delta}. \tag{4.1}$$

In spectroscopic ellipsometry this information is collected for a variety of wavelengths. This information can be used to refine the model used to fit the data, as well as to provide more detailed information about the index of refraction of the materials involved as a function of wavelength.

It is not generally possible to analytically compute the complex indices of refraction or layer thicknesses of the materials involved directly from ψ and Δ. Instead, the interface system (potentially consisting of many layers of unknown thicknesses and refractive indices) is modeled with varying parameters of d (thickness) and complex

N (index of refraction) until the expected ψ and Δ converge on the measured values.

The ellipsometer used in this experiment was a J. A. Woollam Co. M-2000. Measurements were made at an incident angle of 65-75°, for a period of 1 second. To simplify the modelling process and improve the precision of film thickness measurements, the films used for these measurements were directly deposited onto strips of silicon. Using silicon as the substrate and including a 1 nm thick layer of native oxide, the film layer at each point was fit to the collected data using a Cauchy simulation (equation (4.2)), whose initial thickness was set according to values determined using profilometry, simulating the complex index of refraction N, of the form[84]

$$N(\lambda) = A_C + \frac{B_C}{\lambda} + \frac{C_C}{\lambda^2}. \tag{4.2}$$

The data were fit using wavelengths (λ) of 500 - 1000 nm, and the Cauchy parameters A_C, B_C, C_C, and the thickness were all allowed to vary. Wavelengths below 500 nm were not considered due to absorption effects. Specifically, the band gap of ZnO of 3.4 eV[85] corresponds to a wavelength of $\sim$365 nm. Surface roughness was not included in the calculation as it did not significantly change the calculated film thickness for films with thicknesses on the order of 100 nm.

4.2 Film Stoichiometry

Many factors affect the deposition rate for a given material during sputtering, including the specific target and magnetron in use, the pressure and composition of gasses in the chamber, and the specific 'tunnels' used to create the variation in deposition rate with respect to table position. It is therefore necessary to directly determine the stoichiometric ratio of the sputtered materials as a function of position relative to the center of the sputtering chamber.

4.2.1 Electron Microprobe

The main method used to determine the composition of the films was WDS mode electron microprobe. A JEOL JXA-8200 Electron Probe Microanalyzer was available for use, which is capable of both wavelength-dispersive (WDS) mode and energy-dispersive (EDS) mode measurements.

Electron microprobe measurements involve bombarding the material of interest with electrons of energy high enough to promote electrons in the 'inner' K or L shells of the sample atoms. Upon returning to ground state these electrons emit X-rays at wavelengths that are ideally unique to the atom involved. Detecting these X-rays yields information about the atomic composition of the sample.[86]

In the simpler EDS mode, X-rays of a number of energies are detected simultaneously using an energy-sensitive detector, producing a spectrum of intensity vs. X-ray energy. This mode is most useful when the constituent atoms of a sample are unknown, as it can provide an overview of all elements making up a significant portion of the sample. While the relative peak heights at different energies can give an approximate measure of the ratio of elements in the material of interest, EDS mode lacks precision relative to WDS mode where atomic fraction and detection of trace elements are concerned.

WDS mode is more complex, and uses a crystal to separate X-rays of different energies. Intensity is measured only at a single specific X-ray energy. Prior to measurement, a 'standard' of pure material is used to calibrate the count rate of each detector. In the case of this experiment multiple detectors were used, and the Zn, In and Sn detectors were calibrated against the sputtering target used to create the film to be studied. WDS produces much more precise measurements of the relative composition of a sample compared to EDS.

WDS mode is therefore the method of choice for finding film stoichiometry, as well as checking for contaminants. The microanalyzer was configured to detect the oxygen K_α, silicon K_α, zinc L_α, and indium L_α or tin L_α transitions, depending on

the sample. An accelerating voltage of 5 kV was used. A strong silicon signal would indicate that a significant portion of the emitted X-rays are from the layers under the film in question, and not from the film itself. While data where this occurs are still useful, it is necessary to apply a correction for the different penetration depths of the materials being studied. All data presented as a function of film stoichiometry use the zinc fraction. The zinc oxide fraction x of zinc-tin oxide ($(ZnO)_x(SnO_2)_{1-x}$) was taken to be equivalent to the ratio of atomic percentages from the WDS microprobe data. Molar zinc oxide fraction was calculated using

$$Zn\ Fraction = \frac{\%Zn}{\%Zn + \%Sn}. \tag{4.3}$$

A similar calculation was used to find the zinc oxide fraction for zinc-indium oxide ($(ZnO)_x(In_2O_3)_{1-x}$) using

$$Zn\ Fraction = \frac{\%Zn}{\%Zn + \frac{\%In}{2}}. \tag{4.4}$$

The value x is used to refer to this zinc oxide fraction, as measured by electron microprobe, for all data presented in the thesis. Microprobe measurements were taken as a function of position on silicon strips that had been arranged radially with their inner edges at a fixed distance from the table center. Therefore film compositions could be mapped to radial positions on the table, and therefore to any film thickness, mass or device measurements.

4.2.2 Mass Disks

Mass disks were 1.5 cm diameter punched disks of aluminum foil included on the sputtering table, each at a different radial position. These disks were cleaned with methanol and weighed prior to sputtering, and then weighed again afterward. Using the change in mass of each disk and its area, an areal film density was determined. These data were combined with the measured thickness of the film at that radial distance, and the result was used to determine the average film density over the area

of each disk.

These data convey information about the structure of the sputtered material, as a difference in bulk density with respect to known values speaks to the porosity of the sputtered films. It is also useful for identifying potential errors in the microprobe data, if one assumes that the materials sputter with a bulk density that approximates known values for the individual materials.

The mass disk data was also used in combination with the known deposition profiles of the masks over the sputtering targets to help verify the microprobe data. To do this, an 'expected' profile of the atomic data was calculated using the molar mass of the target materials and the known deposition profile (with respect to radial table position) of the masks. This profile was a function of the deposition rates of the two targets. The deposition rates were then varied to find a best fit to both the mass disk and microprobe data.

4.3 Film Structure

X-ray diffraction was used to shed light on the structure of the sputtered films, as well as the degree to which that structure was affected by the various annealing conditions used. By relating changes in crystallinity to changes in electrical conductivity and thermal conductivity, it is possible to gain insight into the relative contributions of phonons and charge carriers to the thermal conductivity.

4.3.1 X-ray Diffraction

X-ray diffraction (XRD) measurements involve bombarding a material with X-rays of a known, specific wavelength, typically those of the copper K_α transition. In the glancing angle X-ray diffraction used in this study, these X-rays are incident upon the sample at 1° or 2° relative to the sample surface. As these X-rays are scattered by the internal structure of the sample, they will constructively interfere at angles relative to the incident beam (θ) that correspond to spacing between planes in a

crystallographically ordered sample (d_l) in a manner described by Bragg's law, given as[87]

$$n\lambda = 2d_l sin(\theta). \quad (4.5)$$

All X-ray diffraction data reported in this project were collected using a small incident angle ('glancing angle') and a curved, multi-angle detector. Glancing angle XRD is useful for thin films as the low angle of incidence increases the relative contribution of the film of interest by increasing the path length of the incident beam through the material of interest.[87]

Both the Inel and Bruker D8 Discover systems used here employ curved-angle detectors that record intensity as a function of a number of angles simultaneously. A peak recorded at a given angle indicates that the corresponding interatomic spacing is common in the sample material.

The films studied in XRD measurements were deposited onto single-crystal silicon, typically onto the (100) surface, which acts as a 'zero background' holder for the films. All peaks visible in the X-ray diffraction data were therefore taken to be due to the films.

Chapter 5

Electrical and Thermal Characterization

5.1 Field Effect Transistors

5.1.1 Transistor Design

The transistors used in this project were of a top contact design, using a heavily doped silicon substrate as a gate electrode and thermally grown oxide as the dielectric. A cross section of this configuration is shown in figure 2.1. Semiconductor films were sputtered through a stainless steel stencil mask with the design shown in figure 5.1. Contacts were made of aluminum, and were thermally evaporated in vacuum using a

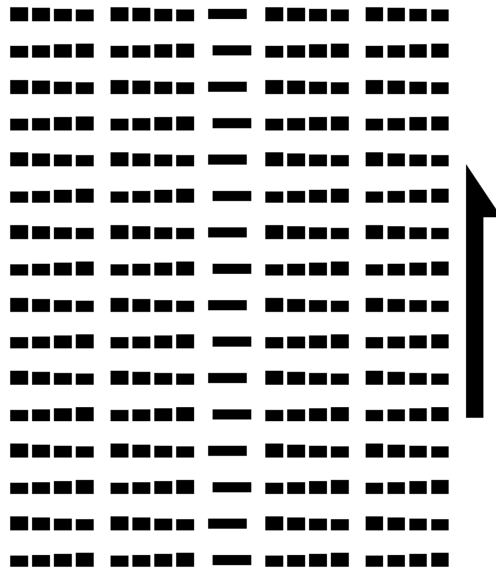

Figure 5.1: Stencil mask used to pattern the semiconductor oxide during sputtering. Each 'pad' of sputtered oxide is electrically isolated from its neighbours, minimizing fringing effects and allowing the use of a common gate electrode for all devices.

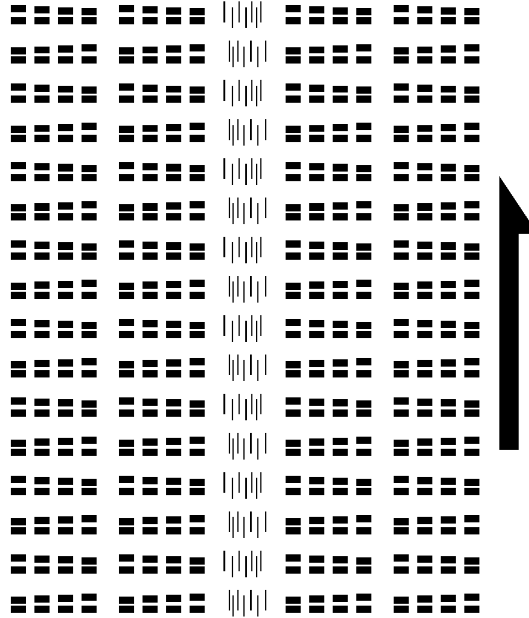

Figure 5.2: Metal contact stencil masks for the TFT portion of the project. The thin strips of metal are for use in characterizing the contact resistance between the aluminum contacts and the semiconductor.

tungsten filament at ∼0.1 nm/s through a stainless steel stencil mask of the design in figure 5.2.

5.1.2 I-V Measurements

Source and drain contacts for each device were contacted individually using tungsten probes. Contact was made to the heavily doped silicon substrate by scratching through the thermal oxide, and contacting the bare wafer with a probe. The substrate acted as a common gate for all devices on the wafer.

Gate and drain current measurements were made for each applied gate-source voltage and drain-source voltage using two Keithley 236 Source-Measure Units. These measurements were divided into three phases. First, a linear mode source-drain voltage (equation (2.3)) was applied, and the source-drain current (linear transfer curve)

was recorded as the gate voltage was swept between specified values in both directions. A saturation mode source-drain voltage (equation (2.2)) was then applied, and the source-drain current (saturation transfer curve) was recorded for the same range of gate voltages. Finally, the source-drain current was recorded as a function of source-drain voltage for a series of gate voltages (output characteristic).

5.1.3 Noise Reduction and Light Sensitivity

'Off' current measurements, some of which were as low as 10^{-14} A, are highly sensitive to electrical noise. The I-V characteristics were also found to be sensitive to light, with significant rises in 'off' current observed after brief exposure to visible light. Some devices exhibited decay times for this effect in excess of 24 hours. More details of this effect are discussed in chapter 6.

To combat light exposure and electromagnetic interference in these measurements, an aluminum foil-lined box with an opaque curtain was placed over the entire probe-station assembly. When moving probes from one device to another, the samples were lit using a low-intensity red LED flashlight. A brief series of tests determined that the light from these LEDs did not noticeably affect the I-V characteristics of the transistors.

5.2 Automated Thermal Conductivity Measurements

Taking manual 3ω measurements on individual heaters was found to be very slow. In order to get an accurate value for the temperature coefficient of resistance, each individual heater would need to be warmed and then slowly cooled prior to 3ω measurements, causing a measurement on a single heater to take one to two hours. In order to characterize a large number of locations on a sample quickly, it was necessary to develop automation for implementing the 3ω method. Ideally the equipment developed for implementing this method would also be used to characterize the electrical conductivity as well. To accomplish this, photomasks, PCBs and an enclosure were

developed to allow connection of metallic structures on the surface of a silicon wafer to the various pieces of equipment necessary for the measurements.

5.2.1 Photomask Design

Initially, the photomask was designed to route current through all 16 heaters in a group in series, and was configured to use 'zebra' connectors to make contact with the PCB. However, it was found that the current source used (5 V_{rms} with a 50 Ω output impedance, the output of the built-in oscillator on a Stanford Research Systems 810 DSP Lock-In Amplifier) did not provide sufficient power for a reliable third harmonic reading when that power was split among 16 heaters. It was also found that 'zebra' connectors did not maintain a reliable, low resistance contact between the PCB and the wafer after the repeated mechanical cycling of removing and replacing the PCB. This unreliability created artifacts at the third harmonic that swamped the experimental signal.

The final revision for the metal photomask is shown in figure 5.3. In this design, only a positive current bus is shared among all heaters. The voltage sense lines and negative current bus are all switched for each heater. Each group of sixteen heaters is contacted by a set of 50 pogo pins, using the square contact pads indicated in the figure. The resistance of the entire current path for any individual heater is a function of the thickness of the deposited metal. However, since the output impedance of the current source was 50 Ω, the thickness of the metal was selected such that the current path for all heaters was also approximately 50 Ω, maximizing the available power, and subsequent third harmonic voltage signal, for those heaters.

5.2.2 Unintentional Joule-Heating

An important consideration in 3ω measurements is ensuring that the heat generated by the linear heater is the only periodic heat source in the vicinity of the measurement. In early mask designs (figure 5.4) the effects of other heat sources in the area were

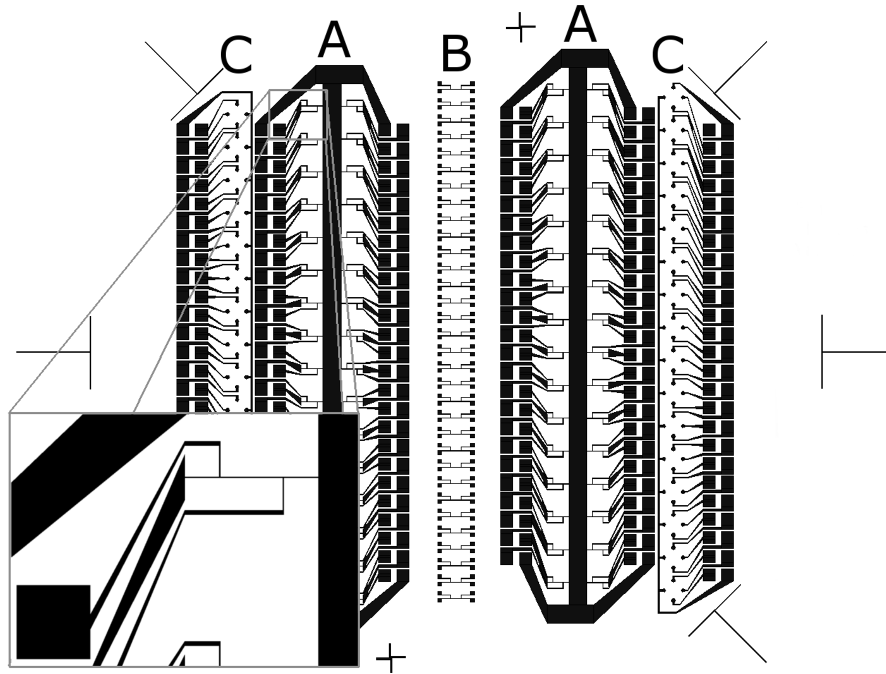

Figure 5.3: The photomask used to pattern the metal heaters, contact pads, sense lines, and current buses on samples used in the automated 3ω system. The label A indicates a set of 32 heaters which can be contacted 16 at a time using the contact pads on either side. Both groups of 16 heaters share a common, positive current bus between them. The structures under label B are 'manual' heaters that can be contacted using conductive probes. Label C indicates the metal contacts for a set of 'cloverleaf' structures used in van der Pauw sheet resistance measurements.

not considered. The effects of this unexpected heating resulted in reported substrate thermal conductivities that were far in excess of literature values, typically over 200 W/m·K, compared to a literature value of 142 W/m·K[82]. There was a qualitative relationship between the injection line/heater angle and the error in the reported substrate thermal conductivity. Manually lowering the resistance of the current lines with silver paint resulted in reported substrate thermal conductivities that were much closer to literature. The updated design in figure 5.5 was used in all subsequent testing and eliminated this effect. All 3ω data reported here were taken using this more recent design.

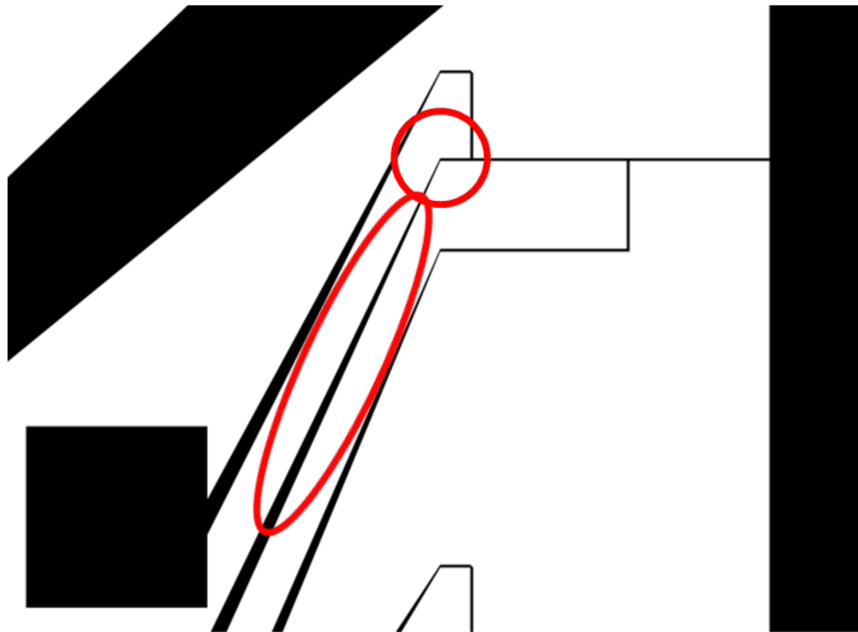

Figure 5.4: Original heater design at the edge of a heater group. Note the ‘sharp’ corner on the current injection line. It is speculated that the increase in resistance at this point created a hot spot that affected the measured temperature of the heater. Another possible problem is heating of the current injection line (oval).

5.2.3 Enclosure and PCB

A printed circuit board was used to make the connection from the pogo pins to 50-pin ribbon cable headers. To keep the board and wafer aligned, an aluminum enclosure was designed. The wafer sits within a 0.5 mm deep cavity in the bottom half of the enclosure, with the wafer flat aligned against one edge. The PCB fits over alignment posts in the holder, as seen in figure 5.6.

The top half of the enclosure also aligns along these posts, providing holes through which the ribbon cable headers are exposed. The two halves are held together using thumbscrews, with stops set to apply the appropriate amount of pressure on the pogo pins. This entire assembly can be heated, allowing for measurements to be taken as a function of temperature. Unfortunately, plastic components in the pogo pins and ribbon cable headers prevent heating beyond ∼100°C.

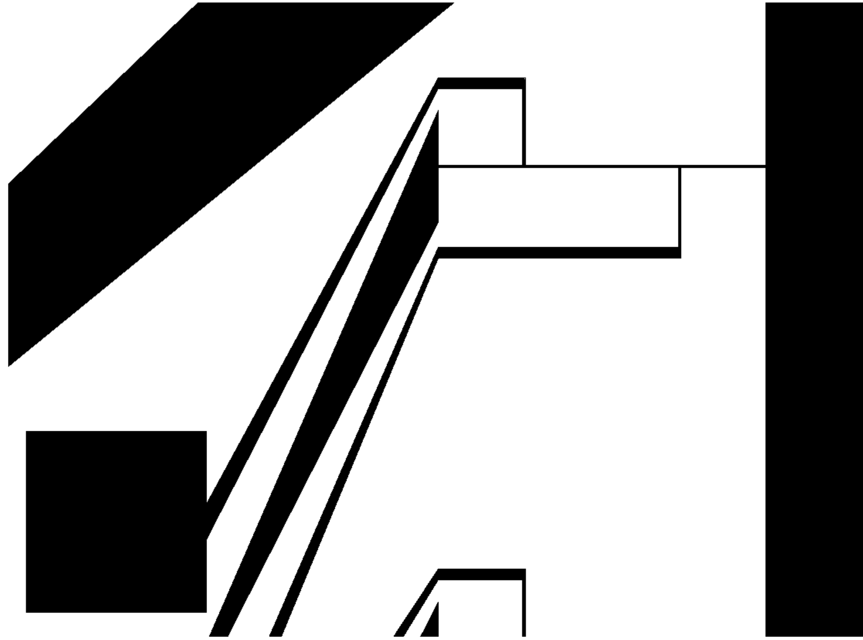

Figure 5.5: Updated photomask, designed to minimize heat generated from current injection lines.

5.2.4 Switch Matrix

A Keithley 7001 Switch Mainframe with a Keithley 7011-S Switch Card was used to switch between heaters in a given 16-heater group. The 50-conductor ribbon cable from the PCB connects to a manually soldered PCB that then connects, via four 20-conductor ribbon cables, to the switch matrix. The voltage sense lines for all sixteen heaters are addressed using channels 1-16 on the card, while the negative current lines are switched using the positive pole of channels 20-36. The switch mainframe was controlled via GPIB.

5.2.5 Lock-In Amplifier

In 3ω measurements, the third harmonic signal is approximately three orders of magnitude smaller than the applied voltage at 1ω. As a result, it is not possible to directly measure the third harmonic voltage from the raw signal taken from the voltage sense

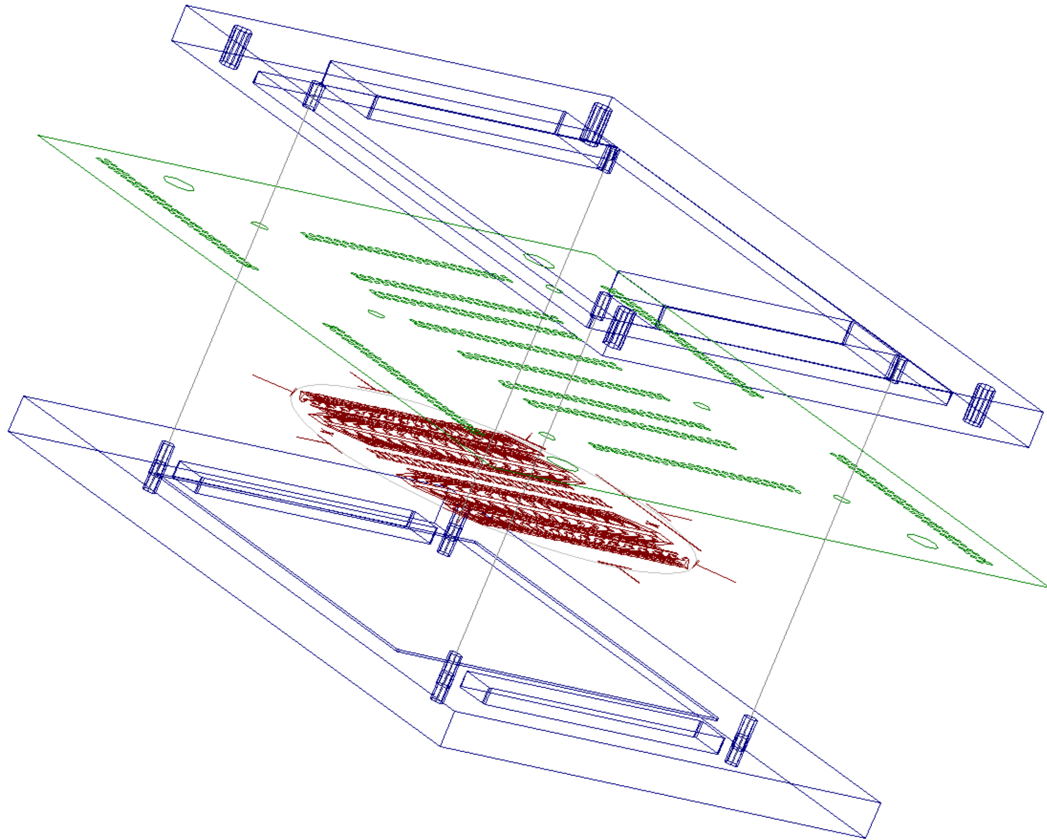

Figure 5.6: Exploded view of the entire assembly, with holder (blue), PCB (green) and wafer (red).

leads on a heater. While it is possible to observe the third harmonic component using a Fourier transform of the signal, the most precise method for isolating the third harmonic is a lock-in amplifier.

In its simplest form, a lock-in measurement depends on the idea that an experiment driven at a known frequency ω will have an output that is also at ω, or some multiple of ω. By multiplying the experiment's output by a reference signal $n\omega$ that is in-phase with the nth harmonic of the driving signal, and integrating the result over many periods, all components of the experimental output that are not at $n\omega$ will average to zero.

3ω measurements in this project were made using a Stanford Research Systems 810

DSP lock-in amplifier. In early 3ω experiments[72, 88], the analog lock-in amplifiers used required that a reference signal at the third harmonic of the driving signal be generated externally. However, when using a digital lock-in amplifier, the reference signal at $n\omega$ is digitally generated, at effectively arbitrarily large n.

In general, the interval of integration is a time that is at least three times the period of the driving signal. In practice, an integration time much longer than this is necessary to produce acceptable results. For most measurements in this experiment, driving frequencies in the range of 300-1000 Hz were used, with an integration time of 300 ms. Differential measurements were made in AC mode at frequencies that were evenly spaced in $ln(2f)$ over the specified range. No filtering was done to eliminate line frequencies, but frequencies were selected to avoid multiples of 60 Hz. It was found that the built-in filters for 60 and 120 Hz produced artifacts in the data for frequencies below ~300 Hz.

The frequency range of 300-1000 Hz was chosen to satisfy the thermal penetration depth requirements outlined in section 2.4.3. The half-width of the heaters used for all 3ω data reported was 12.5 μm, and all 3ω measurements were conducted on substrates of silicon with a thickness of 0.5 mm. Silicon has a thermal diffusivity of approximately 0.8 cm^2/s [89] at room temperature. At 300 Hz, the thermal penetration depth is ~150 μm, well below the 500μm thickness of the substrate. At 1000 Hz the depth is ~80 μm, well above the 12.5 μm half-width of the heaters.

The lock-in amplifier used was a dual-phase model, meaning that it was able to simultaneously isolate signals that were both in-phase and 90° out of phase with the reference signal. The lock-in amplifier was controlled via GPIB.

5.2.6 AC Current Measurements

Measurement of the AC current was a necessary step for calculating the power dissipated in the heater strip, as well as the resistance of that strip. A Keithley 2700 Digital Multimeter was used to measure the AC current. The negative current line coming from channels 20-36 of the switch matrix was passed through the ammeter

inputs of the DMM prior to connecting back to the negative pole of the oscillator output on the lock-in amplifier. The Keithley 2700 was connected via GPIB.

A schematic diagram of the entire group of devices and connections used for automated 3ω measurements is shown in figure 5.7.

Figure 5.7: Schematic diagram of the experimental setup. Each heater has a single common contact (the positive AC out) and three switched contacts: the negative AC out, and two sense contacts connected to channels A and B of the lock-in amplifier.

5.2.7 Temperature Coefficient of Resistance

A type K thermocouple was attached directly to the wafer, and was monitored using an Omega temperature controller, connected to a computer via RS485.

Using the $V_{1\omega}$ signal, the AC current, and the temperature from the thermocouple, the resistance for each heater was determined as a function of temperature. This was accomplished by heating the entire holder/PCB/wafer structure to approximately

35°C and allowing it to cool. Resistance measurements were taken continuously during cooling by switching through the sixteen connected heaters. A linear fit to these data was used to compute the temperature coefficient of resistance (C_{RT} in equation (2.45)) for each device. These resistance values were also used in the calculation of substrate and film thermal conductivities.

5.2.8 3ω Measurement Process

For 3ω measurements, a range of frequencies and number of steps were specified, as well as a range of powers and a number of steps. These powers and frequencies were applied to each connected device. As each device was connected via the switch matrix, a resistance measurement was performed, and the necessary applied voltage was calculated for a series of voltages that would be evenly spaced when expressed as $V_{1\omega}^3$, facilitating the best possible fit for $\frac{dV_{3\omega}}{dV_{1\omega}^3}$. $V_{1\omega}$ was then recorded by the lock-in amplifier for each of these powers at the lowest specified frequency, followed by a $V_{3\omega}$ measurement for all frequencies at each specified power. Frequencies in the specified range were chosen so that they were evenly spaced in $ln(2\omega)$.

This apparatus allowed for automated characterization of the thermal conductivity of sixteen combinatorial library positions in an amount of time limited only by the cooling time needed for the calculation of C_{rt}. With four groups of sixteen heaters, a library of 96 different positions could be tested very quickly with minimal manual intervention.

5.3 Automated van der Pauw Measurements

For automated sheet resistance measurements, the 50-conductor cabling and switch matrix configuration were identical to those used in 3ω measurements. However, the only piece of measurement instrumentation used was the Keithley 2700 DMM.

5.3.1 Switch Matrix

The positive and negative of channels 1-16 of the switch matrix were connected in turn to the negative 'source' and 'sense' terminals used for 4-wire resistance measurements on the Keithley 2700. This connected these two leads to two opposing contacts on the connected van der Pauw structure. The positive 'source' terminal was connected to one of the ribbon cable conductors that lead to a single 'bus' contact that was common to all 16 van der Pauw structures in a group, and was analogous to the large shared current bus in the 3ω structures. The positive pole of channels 20-36 were switched simultaneously with channels 1-16, respectively, connecting to the positive 'sense' terminal on the DMM.

5.3.2 4-wire Resistance Measurements

The Keithley 2700 was set to a slow, autoranging 4-wire resistance measurement. Software communicating via GPIB switched through the sixteen connected van der Pauw structures and recorded a 4-wire measurement for each. The negative source and sense terminals on the DMM were then manually swapped, and another sixteen measurements were taken. Swapping opposing contacts allowed for a second resistance measurement in an orientation that was orthogonal to the first, permitting the use of the van der Pauw sheet resistance calculation outlined in section 2.3.2.

In some films the resistance was too high for the Keithley 2700 to take an accurate 4-wire resistance measurement. In these cases a single Keithley 236 Source-Measure Unit was used in remote sense mode. The SMU was connected in a similar way, with the negative source and sense leads on channels 1-16, the positive source lead on the common conductor and the positive sense lead connected to channels 20-36. A source current was specified, and software recorded the sensed voltage.

5.3.3 Manual Measurement for Very High Resistance

If a 4-wire measurement was not possible due to a given film being too resistive, a manual measurement was necessary. In this case a two wire measurement was performed on film on a 0.5 cm x 1 cm piece of glass, cut from a strip included in the sputtering run. The sheet resistance of the square was calculated using the dimensions of the glass. Since this process is only used for highly resistive films, it was assumed that resistance of leads and contacts was negligible. The sheet resistance R_S was calculated from the 2-wire resistance and the length L and width W of the sample, as

$$R_S = \frac{L}{W} R_{2-wire}. \tag{5.1}$$

5.4 Manual Hall Effect Measurements

Hall effect measurements of charge carrier density were carried out using the same cloverleaf structures used for the sheet resistance measurements. The wiring was similar to that in section 5.3.2, save that the 'source' contacts were configured such that current flowed between opposing contacts on each cloverleaf, with the 'sense' leads connected on either side of the current path.

The entire wafer/PCB/holder assembly was placed between the poles of a large electromagnet, arranged such that the field lines were perpendicular to the plane of the wafer. For a given applied current, the voltage between the 'sense' leads was recorded for several magnetic field strengths between 0 and 3000 gauss. These measurements were repeated for the orthogonal current direction. Differences in the sensed voltage between different applied field strengths were taken to be the Hall voltage. The Hall voltage can be expressed as the film thickness d, charge carrier density n, fundamental charge q, applied current I and applied magnetic field B, in the form

$$V_H = \frac{-IB}{ndq}. \tag{5.2}$$

To use the change in sensed voltage for a given change in field strength, it is convenient to differentiate V_H with respect to B to get

$$\frac{dV_H}{dB} = \frac{-I}{ndq}. \tag{5.3}$$

Using the slope of V_H as a function of B, along with the applied current and measured film thickness, the charge carrier density in the measured films was calculated. Using this density, the equation (2.27), and the measured electrical conductivity of each film, a Hall mobility was also calculated.

5.5 Seebeck Coefficient

Any measurement of the Seebeck coefficient requires that the thermoelectric properties of the components used in the apparatus be well understood. This is because measurement of the Seebeck voltage will yield the sum of the contributions from the Seebeck effect in the material being measured, as well as in the materials used to contact the sample. However, if the thermoelectric behaviour of the material used to contact the sample is well understood, it can be predicted and subtracted from the measured voltage.

Seebeck measurements were conducted using a Quantum Design Physical Properties Measurement System 9T (PPMS).

5.5.1 Sample Preparation

Two gold-plated copper leads were affixed to the film side of a square of glass cut from strips included on the table during sputtering. Leads were affixed to the sample using Epotek H-20E silver epoxy. The samples were heated to 80°C for 30 minutes to cure the epoxy. A 'shoe' containing both a voltage sense wire and a LakeShore Cryotronics Cernox 1050 temperature sensor were attached to each lead. One lead was also connected to a heating element, while the other was connected directly to the sample 'puck', which acted as a heatsink. The puck was then inserted into the

PPMS using the measurement probe.

Since the sample of sputtered film is not free-standing, it is assumed for these measurements that there is no contribution to the Seebeck voltage from the glass substrate.

5.5.2 Measurement of the Seebeck Coefficient

Once a given sample was inserted into the system the chamber was purged with helium gas and then pumped down to $\sim 10^{-5}$ Torr. The system temperature was set to 300 K. A fixed power was applied to the heating element for four minutes, and the sample was allowed to come to equilibrium. After reading the resulting temperature, the power was automatically adjusted to allow the sample to approach a temperature difference between the 'hot' and 'cold' leads of 3%, or 9°C. Once this temperature difference was achieved and was stable over a period of several minutes, a differential voltage measurement was taken.

The PPMS was calibrated and configured to automatically remove the contribution of the leads used to contact the sample to the Seebeck voltage. The resulting Seebeck voltage divided by the temperature difference is the Seebeck coefficient.

It should be noted that while this is a relatively simple measurement, its manual nature precluded testing the entire combinatorial library of a given sample. Additionally, samples with very low ($\sim$1 S/m) electrical conductivity were excluded from Seebeck measurements due to the difficulty in measuring the Seebeck voltage in these samples.

For the purposes of screening the combinatorial libraries, a selection of five library positions, approximately evenly spaced over the entire combinatorial range, was selected.

Chapter 6

Field Effect Transistor Studies[1]

6.1 Zinc Tin Oxide

6.1.1 Sample Fabrication

Transistors were fabricated on 100 mm, heavily n-doped (arsenic, $< 0.005\ \Omega\cdot$cm) <100> prime grade silicon wafers with a 100 ± 2 nm thermally grown SiO_2 layer, acquired from Silicon Quest International. Prior to being placed in the sputtering chamber, each wafer was oxygen-plasma cleaned in a reactive ion etcher at a power density of 0.08 W/cm^2 in 150 mTorr of O_2. 50 mm ZnO (99.999%) and SnO_2 (99.9%) targets were purchased from Kurt J. Lesker and Williams Advanced Materials, respectively.

ZnO and SnO_2 targets were sputtered at powers of 108 W and 43 W, respectively, with a sputter gas pressure of 5 mTorr consisting of 90% Ar and 10% O_2. The substrates were nominally at room temperature. The sources were masked such that ZnO had a deposition rate of 0.4 nm/sec at the outer edge of the track and this rate decreased linearly to 0 at the inner edge of the track, while the SnO_2 target had approximately the same rates, but decreasing from the inner to the outer edge. The table was rotated quickly with respect to the deposition rate (15 rpm) such that the thickness of ZnO deposited per rotation was less than a monolayer, varying between 0 and 0.04 nm. This resulted in intimate mixing of the sputtered materials and, ideally,

[1] Some sections of this chapter have been reprinted with permission from M. G. McDowell, R. J. Sanderson, and I. G. Hill, Combinatorial study of zinc tin oxide thin-film transistors, Applied Physics Letters, 92:013502, Copyright 2008, AIP Publishing LLC.
Some sections © 2009 IEEE. Some sections reprinted, with permission, from M. G. McDowell and Ian G. Hill, Influence of Channel Stoichiometry on Zinc Indium Oxide Thin-Film Transistor Performance, IEEE Transactions on Electron Devices, February, 2009.

a continuum of stoichiometries of the form $(ZnO)_x(SnO_2)_{1-x}$ ranging approximately linearly from $x = 0$ at the inner edge, to $x = 1$ at the outer edge.

To avoid large leakage currents resulting from the increased sensitivity to pinholes and fringing effects inherent in samples having many transistors using a single, large area semiconductor layer, the deposited metal oxides on each wafer were patterned using a stainless steel stencil mask (shown in figure 5.1) during the sputtering process, such that each transistor had an electrically isolated active channel. To eliminate possible unintentional doping of the semiconductor due to oxygen deficiencies, the wafers were post-annealed in O_2 for 30 minutes at temperatures of 550, 600, 650 and 700 °C. Aluminum source and drain contacts were then vacuum vapor deposited through the stencil mask in figure 5.2. Devices had width/length ratios varying from 4 to 16, with channel lengths varying from 125 to 500 μm and there were a total of 256 devices per wafer.

6.1.2 Physical Characterization

The stoichiometry of the films was determined using microprobe, as described in section 4.2.1. The sputtered semiconductor layer was revealed to have a relative atomic fraction of 85% Sn, 15% Zn at one extreme and 5% Sn, 95% Zn at the other (figure 6.1), varying approximately linearly between the two. The ratio of oxygen to zinc and tin signals was consistent with a film consisting primarily of ZnO and SnO_2 (tin (IV) oxide), as opposed to SnO (tin (II) oxide). There was some initial concern that the use of shadow masks in direct contact with the wafer would result in contamination of the deposited film due to secondary sputtering of the stainless steel mask. However, the film yielded no iron signal when tested using the electron probe.

Using a Dektak profilometer, the deposited film was found to be approximately 50 nm thick at all positions within the sputtered track. Initial test samples were annealed under argon[14] at 300°C , but these were found to be conductive while off, exhibiting poor on/off ratios particularly in regions of high SnO_2 concentration. However, another set of devices that was annealed under O_2 had vastly improved on/off

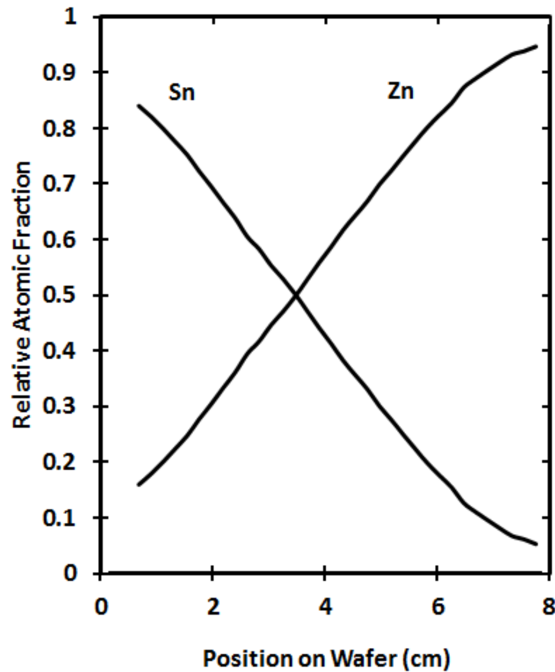

Figure 6.1: Measured stoichiometry of the mixed zinc oxide/tin dioxide sputtered film.

ratios compared to this original set. This difference in off current is consistent with as-deposited films containing a high density of oxygen vacancies that heavily dope the semiconductor and limit gate-induced modulation of active channel conductivity. Of the four annealing temperatures studied, devices annealed at 600°C exhibited the highest performance and lowest rate of defects (annealing temperatures of 550, 600, 650, and 750 °C were tested).

6.1.3 Field Effect Mobility vs. Stoichiometry

I-V characteristics were collected using the method described in section 5.1.2, and analyzed using the ideal field effect transistor equations in section 2.1.2. A typical saturation transfer curve is shown in figure 6.2. Electron mobilities were found to vary from 2 to 12 $cm^2/V{\cdot}s$ across the available range of stoichiometries. While mobilities for sputtered ZTO devices have been reported to be as high as 50 $cm^2/V{\cdot}s$[7], these were reported for devices fabricated using indium tin oxide (ITO) instead of aluminum

for the source and drain contacts. It is likely that the higher contact resistance for devices with Al source and drain contacts limits the observed mobilities in these devices[16].

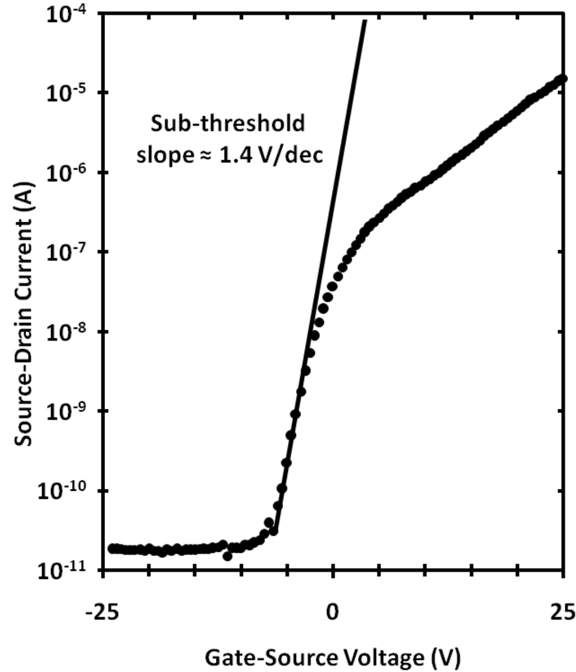

Figure 6.2: A typical saturation transfer curve (V_{DS} = +25 V). The device in this figure has a composition of $x = 0.43$.

Two peaks in mobility are obvious in the data (figure 6.3), with one at a ZnO fraction of 0.25 ± 0.03 and another at 0.80 ± 0.05. The first of these peaks exhibits the highest mobility at 10-12 $cm^2/V{\cdot}s$, while the second is slightly lower at 8-11 $cm^2/V{\cdot}s$. A trough is also visible, centered around the 1:1 point. These results contradict the conclusions in previous work by R. L. Hoffman[20], in which a broad peak is seen around $x = 0.5$, with these results showing what appears to be a trough in mobility at $x = 0.50$. It should be noted that with the exception of the mobilities, the data otherwise given in the preliminary study coincide with the data presented in this paper[20]. For example, the relationship between threshold voltage and stoichiometry and the poor sub-threshold behaviour in devices with high SnO_2 content are both consistent with Hoffman's results. The coarse-grained stoichiometric study

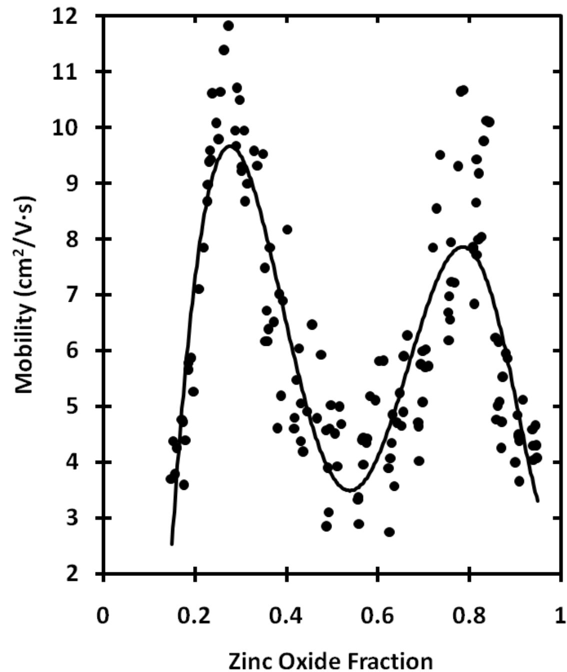

Figure 6.3: Mobility as a function of zinc oxide fraction across an entire wafer of devices. Note that the line serves as a guide to the eye only.

done by Hoffman likely 'misses' the relatively narrow peaks in mobility with respect to stoichiometry.

6.1.4 Threshold Voltage, Sub-Threshold Swing, On/Off Ratio

Threshold voltages varied from -8 V to +18 V (figure 6.4), with the largest of these being in the regions of lowest mobility.

These data suggest that the electrical properties of these films are quite sensitive to stoichiometry and are not optimized at the 1:1 or 2:1 stoichiometries. While the V_{GS} = 25 to -25 sweep generally yielded very slightly higher source-drain currents (for $V_{GS} > V_T$) than the reverse, there was no significant hysteresis visible in the saturation transfer curves. On/off ratios were on the order of 10^6 (figure 6.4) and the best sub-threshold slopes were 1.4 V/decade (figure 6.2) independent of stoichiometry, when tested with no prior light exposure. However, ZnO fractions ≤ 0.33 were found

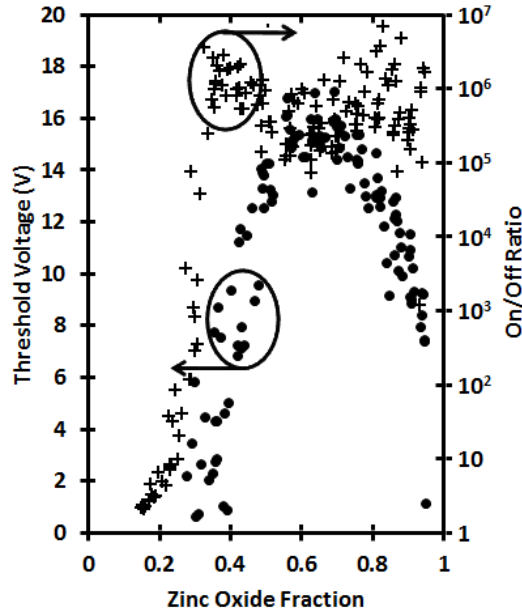

Figure 6.4: Threshold voltage and on/off ratio as a function of zinc oxide fraction across an entire wafer of ZTO devices. The sudden decrease in both threshold voltage and on/off ratio is due to the light sensitivity of these devices.

to be highly light-sensitive, exhibiting changes in on/off ratio of as much as 10^5 for light vs. dark conditions. Mobility was not affected by light exposure.

6.2 Zinc Indium Oxide

6.2.1 Sample Fabrication

Substrates in this experiment were heavily doped silicon (n-type, arsenic, < 0.005 $\Omega\cdot$cm) with a 100 ± 2 nm thermally grown SiO_2 layer, acquired from Silicon Quest International. Prior to sputtering each wafer was oxygen-plasma cleaned at a power density of 0.08 W/cm^2 at a pressure of 150 mTorr for four minutes. Two 50 mm sputter targets were used, one of ZnO (99.999%) at a power of 40 W and the other of In_2O_3 (99.99%) at 90 W, both purchased from Kurt J. Lesker Co. A preliminary study found films sputtered under 10% O_2 and 90% Ar to be highly conductive and other work[65] has shown the conductivity of sputtered ZIO films to be highly

sensitive to the oxygen content of the sputter gas, probably as a result of doping due to oxygen vacancies in the resulting film. Therefore, sputtering took place in 20% oxygen and 80% argon, at a total pressure of 5 mTorr. In initial studies the sources were masked such that the amount of ZnO deposited rose linearly from the inner to the outer edge of the sputtering 'track', while In_2O_3 deposition increased from the outer to the inner edge. This resulted in a film of the form $(ZnO)_x(In_2O_3)_{1-x}$, varying linearly from x=0 to x=1. However, in later sputtering runs the sources were masked such that the amount of ZnO deposited was constant for all radii within the track, and In_2O_3 was sputtered such that the amount deposited varied linearly from a molar amount equal to ZnO at the inner edge of the track to zero at the outer edge, resulting in a film varying from x=0.5 to x=1. A maximum of 0.02 nm of material was deposited on each rotation, ensuring intimate mixing of the two oxides, for a total film thickness of 80 nm at the inner edge of the track to 40 nm at the outer edge. This film thickness was verified post-deposition using Dektak. The ZIO on each wafer was patterned using a stainless steel stencil mask (figure 5.1). To reduce unintentional doping due to oxygen vacancies, the wafers were annealed under oxygen for one hour at either 300°C or 600°C or left as-deposited. Aluminum source and drain contacts were patterned via thermal deposition through stainless steel stencil masks, for a total of 256 devices per wafer. W/L ratios varied between 16 and 4, with channel lengths of 125 to 500 μm.

6.2.2 Physical Characterization

Again, the stoichiometry of the films was determined using the microprobe. The presence of a detectable silicon signal across most positions in the sputtering track indicated that the films used in this device were thin enough that the incident electrons were penetrating through the sputtered film. Using the detection geometry and measured film mass and thickness data, Casino[90] (v2.42) was used to model differences in the interaction volumes for the production of L_α X-rays from indium and zinc. Due to the limited thickness of the films, the results of this modeling were

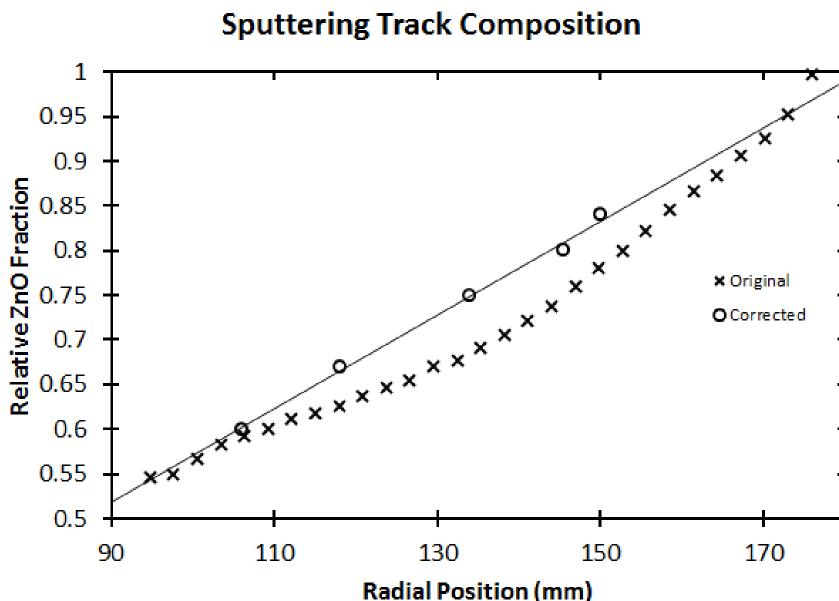

Figure 6.5: Measured stoichiometry of the mixed zinc oxide/tin dioxide sputtered film, comparing the original, measured stoichiometry and the same data corrected using Casino (solid line).

needed to make corrections to the Zn:In ratios derived from the WDS data. Corrections were made at several table positions by varying the simulated mixture ratio at the measured film thickness until the simulated output matched the reported microprobe data. This simulated mixture ratio was then taken to be the true value. Stoichiometry (expressed as $(ZnO)_x(In_2O_3)_{1-x}$) was found to vary linearly from $x = 0.55$ to $x = 1.0$ across the sample (figure 6.5). All films used in subsequent parts of this study were sputtered for a longer duration to avoid the need for any more corrections.

The crystalline structure of the oxide under each annealing condition was examined with glancing angle X-ray diffraction using a curved multi-angle detector (~6° incident angle using Cu $K_{\alpha 1,\alpha 2}$ X-rays). Additionally, transparency was examined for films on glass using an Ocean Optics USB2000 spectrometer and an incandescent light source. Transparency was defined as the ratio of transmitted light through the glass/film system to transmitted light with no glass or film. No corrections were made

for reflections at the interfaces.

6.2.3 Field Effect Mobility vs. Stoichiometry

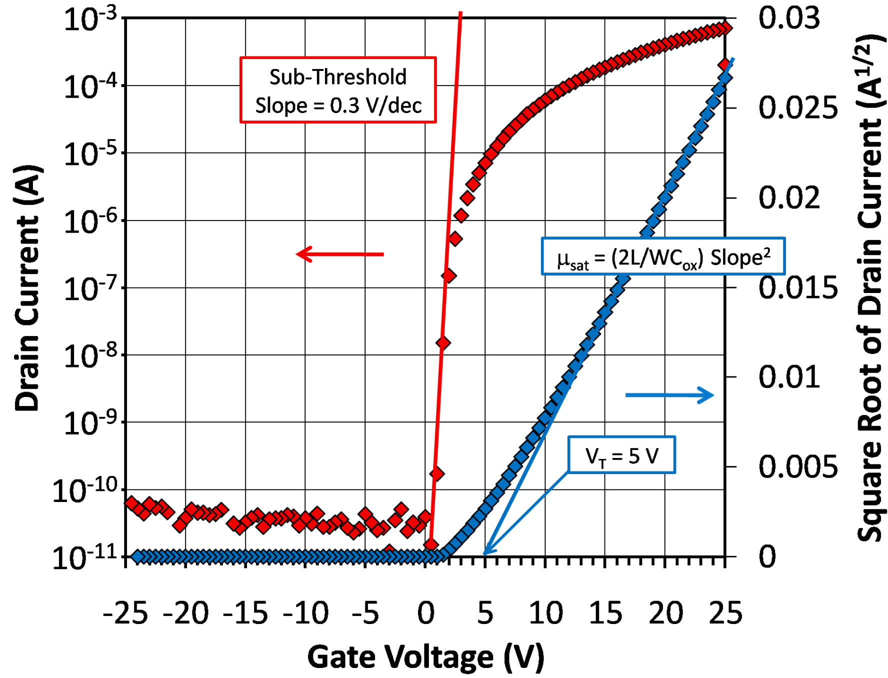

Figure 6.6: A typical saturation transfer curve with V_{DS}=+25V. This figure shows the methods used to determine saturation mobility, threshold voltage and sub-threshold slope. The device has a channel stoichiometry corresponding to x=0.74.

A typical saturation transfer curve for a device annealed at 300°C is shown in figure 6.6. Using these curves, devices annealed at 300°C and 600°C were found to exhibit saturation mobilities of up to 40 and 20 cm^2/V·s, respectively (figure 6.7). Linear mobilities were similar to saturation mobilities for 300°C annealed films, but were up to 30 cm^2/V·s for films annealed at 600°C, likely due to a reduced effect contact resistance between the annealed film and the aluminum contacts during linear mode testing. On/off ratios for $x > 0.6$ varied between 10^6 and 10^9, and are highest for 0.6 $< x <$ 0.75. Below x = 0.6, on/off ratios fell dramatically (to as low as 10), making mobilities impossible to determine using the ideal transistor equations. All devices exhibited an upward trend in mobility with increasing In_2O_3 content for $x > 0.60$,

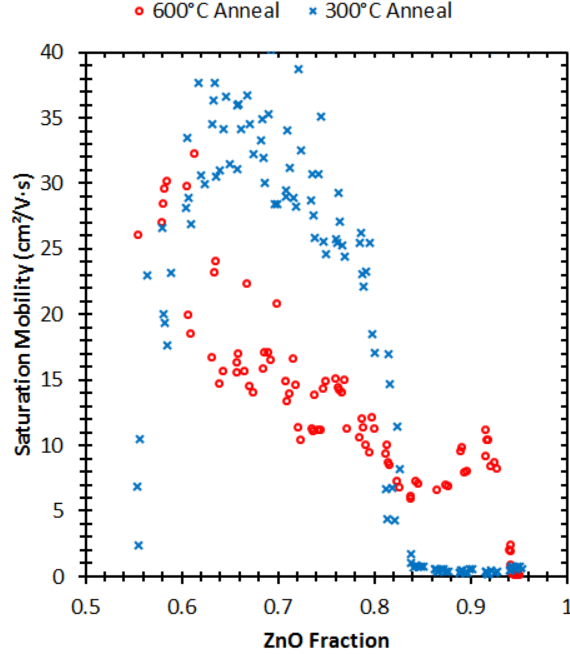

Figure 6.7: Mobility as a function of channel stoichiometry for both 300°C and 600°C annealing conditions.

with peak mobilities at a zinc oxide fraction of 0.67 ± 0.02 for 300°C devices, and 0.60 for 600°C.

6.2.4 Threshold Voltage, Sub-Threshold Swing, On/Off Ratio

Inverse sub-threshold slopes reached a minimum of 0.3 and 0.5 V/dec (for 300°C and 600°C), turn-on voltages (taken to be the voltage at which an exponential increase in source-drain current is observed) were near 0 V and threshold voltages were ∼5 V for $x = 0.75 \pm 0.02$, while mobilities at this ratio are only 10-20% below the highest mobilities. It can therefore be argued that devices at this ratio of 3:1 ZnO:In_2O_3 exhibit 'peak performance'. Inverse sub-threshold slopes were found to be strongly dependent on both the stoichiometry and annealing conditions (figure 6.8).

During testing no significant hysteresis was observed between the on-off and off-on sweeps. Devices using as-deposited films were found to be insulating with drain currents on the order of 10^{-10} A for all gate voltages in the sweep, independent of

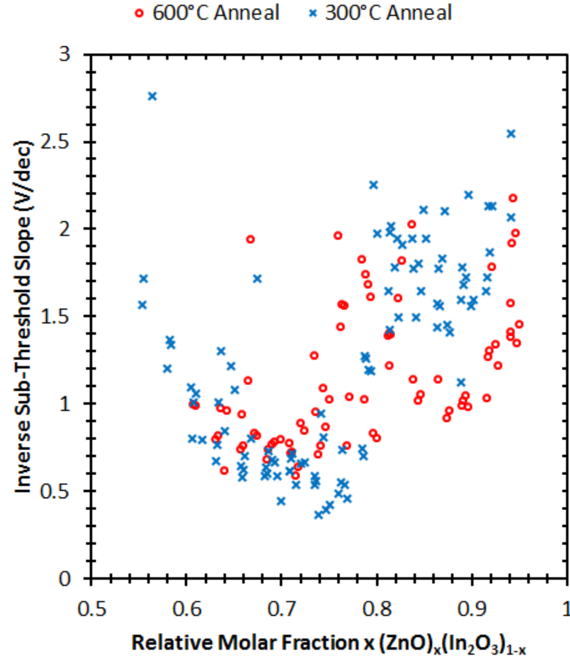

Figure 6.8: Sub-threshold slopes for 300°C and 600 °C annealing conditions as functions of molar ratio.

stoichiometry. Mobility was found to be independent of W/L (4, 4/3, 8, 16) within the experimental scatter of ∼10% at a given stoichiometry. Other work[21, 91] has shown a relationship between ZIO semiconductor thickness (from 15nm to 60nm) and mobility. This relationship was very pronounced at the thin end (∼15 nm) of their tested range, but mobility did not appear to change significantly over the range tested here (40 nm to 80 nm), and no relationship between performance and thickness was apparent. Devices were tested in air over a period of several days, during which time no change in behavior due to atmospheric exposure was observed. However, a single set of devices was briefly re-examined after approximately seven months of storage in air. This set showed reductions in both mobility (on the order of 10%) and threshold voltage (∼-10V).

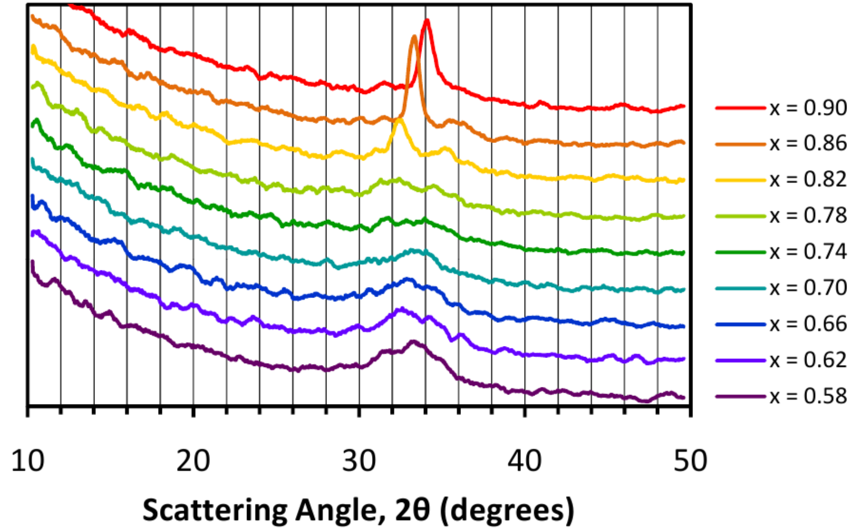

Figure 6.9: XRD example data for 600°C annealing conditions at a variety of film stoichiometries. It should be noted that XRD data were taken for different stoichiometries in steps of δx=0.02. For clarity, only selected stoichiometries are shown.

6.2.5 X-ray Diffraction and Transparency

Glancing-angle XRD (figure 6.9) showed a peak at $2\theta = 34°$ for $x = 0.86$ for films annealed at 600°C, but no peak is visible for the 300°C films. The intensity of the sharp peak decreased with increasing In_2O_3 content, and was no longer visible for x<0.82. The angle of the peak also decreased to 32° at a stoichiometry of $x = 0.82$. This crystalline phase appears to have a significant positive impact on transistor performance; where $x > 0.82$, devices made under the 600°C annealing conditions were found to have mobilities of 10 cm^2/V·s, threshold voltages of ∼8V and sub-threshold slopes of 1 V/decade, while films annealed at 300°C at these stoichiometries yielded only 0.5 cm^2/V·s, with threshold voltages between -5 and -15 V and inverse sub-threshold slopes of 1.5V/dec. However, all annealing conditions showed only a very broad peak from 31° to 36° for $x < 0.82$. This broad peak is consistent with the work of Dehuff, et al.[24] for low annealing temperatures, but our films were not observed to crystallize under high temperature annealing, even at 700°C. This may be due to differences in annealing conditions or relative uncertainties in annealing

temperature. The crystalline structure of similar films is discussed in greater detail in the thermoelectric portion of the study.

6.2.6 TFT Study Conclusions

The transistor study revealed that the two studied mixtures of metal oxides had relatively high carrier mobilities of 10 $cm^2/V{\cdot}s$ in ZTO and 40 $cm^2/V{\cdot}s$ in ZIO, while simultaneously being largely amorphous in structure. This made these materials interesting from the point of view of a thermoelectric study, since high carrier mobility could lend itself to high electrical conductivity under ideal sputtering and annealing conditions, while the amorphous structures of the films suggested relatively low thermal conductivity. The lack of available Seebeck data notwithstanding, high electrical conductivity coupled with low thermal conductivity in a given material suggests the possibility of a high thermoelectric figure of merit. This possibility led to the thermoelectric studies presented in chapters 8 and 9.

Chapter 7

Thermal Conductivity of an SiO_2 Wedge[1]

Prior to the use of the thermal conductivity measurement system outlined in chapter 5 for ZTO or ZIO films, a study on a well-characterized thin film material was done to demonstrate the accuracy and validity of the method. Instead of varying film composition as a function of position on the wafer, a silicon dioxide film of varying thickness was used. In this experiment the substrate thermal conductivity was determined using two methods, and the film thermal conductivity was determined using three methods and both are compared to the literature. This experiment also allowed for a brief examination of thermal resistances at film interfaces, as well as the temperature dependence of the thermal conductivity of silicon.

7.1 Sample Fabrication

A silicon dioxide wedge, ranging from zero to 250 nm in thickness, was RF-sputtered using two, 50 mm silicon dioxide targets (99.995%, acquired from Kurt J. Lesker) in 1 mTorr of argon at 200 W per target. The wedge was sputtered onto a 100 mm, 500 μm thick, heavily doped Si <100> wafer. Several strips of silicon were also included with one edge masked along the main axis of the wedge to allow for film thickness measurements by profilometry. Film thickness was also determined using ellipsometry. All substrates were attached to a water cooled table that was maintained at 15°C during sputtering.

Due to the low resistivity of the wafer (determined via a van der Pauw measurement to be 2.6×10^{-5} $\Omega \cdot$cm) it was necessary that any electrical structures built on

[1]Some sections of this chapter have been reprinted with permission from M. G. McDowell and I. G. Hill, Review of Scientific Instruments, 84:053906, Copyright 2013, AIP Publishing LLC.

the wafers be electrically isolated from the silicon substrate itself. This was achieved with the application of a 450 nm aluminum (III) oxide film which was electron-beam deposited at approximately 0.1 nm/s at a pressure of approximately 10^{-6} Torr. Demonstrating this as part of the sample fabrication procedure was vital, as this film would also be of particular importance in combinatorial studies on electrically conductive sputtered films.

Heaters, contact pads, current buses, and voltage sense lines were patterned via lift-off photolithography using Futurrex NR9-1000PY resist. Aluminum was then deposited via e-beam deposition at approximately 0.1 nm/s, for a total film thickness of 150 nm. The thickness of aluminum was chosen such that the total resistance for each heater/lines/contacts element was approximately equal to the output resistance of the AC source used in the 3ω measurements, maximizing the available power from that source. Due to the long deposition time and the high temperatures necessary for evaporation of aluminum, some heating of the substrate during deposition was observed. However, the temperature immediately after removal of the wafer from vacuum indicated that the wafer temperature likely did not exceed 100°C during deposition. The wafers were allowed to cool before removal from the vacuum chamber. Lift off was then performed in Futurrex RR-5 resist remover, taking approximately thirty minutes. Finally, the wafer was rinsed in de-ionized water and blown dry with compressed air.

7.2 Substrate Thermal Conductivity

Analysis began with an examination of substrate thermal conductivity. This is a necessary step for validating any thin-film data, and for identifying any systematic issues with the measurement system. Using equations (2.51) and (2.52), the substrate thermal conductivity was calculated from data such as those presented in figure 7.1 and the results for all heaters on the wafer presented are figure 7.2.

The result was close to but slightly lower than the generally accepted value for

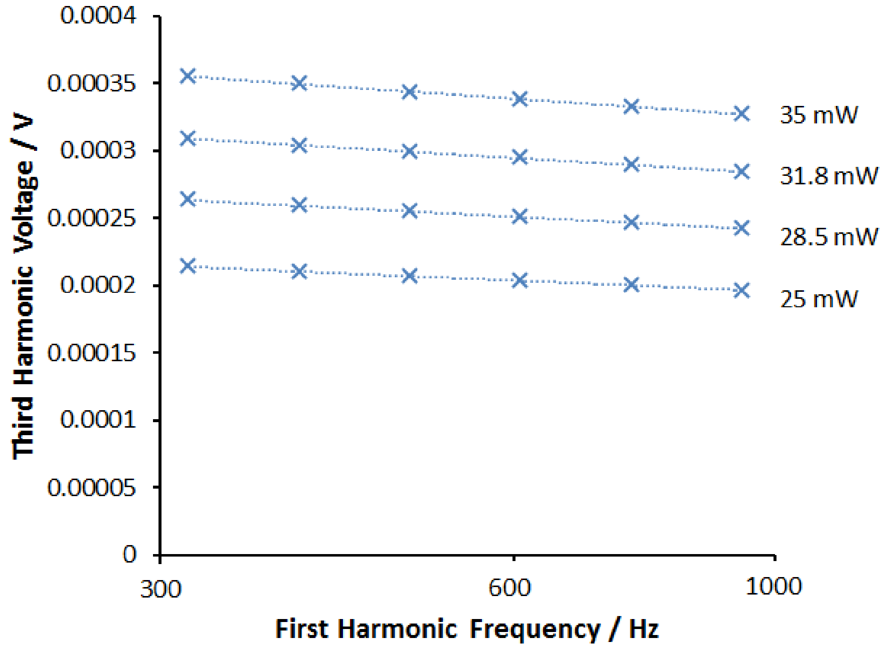

Figure 7.1: A representative set of data for a heater on the SiO_2 wedge. Third harmonic RMS voltage as a function of the frequency of the applied voltage is displayed for a number of applied RMS powers. This heater was on an SiO_2 film thickness of 98 nm.

silicon thermal conductivity of ∼142 W/m·K[82], with the imaginary third harmonic voltage (equation (2.51)) yielding values that were approximately 5% lower than those obtained using the real voltage component (equation (2.52)). Ideally, the determined value should be the same for a heater at any position on the substrate, regardless of the composition of any films between the heater and the substrate. However, it has been observed[92] that heaters on stacks of films yield lower-than-expected substrate thermal conductivities that decrease slightly with increasing film thickness. When considering the total film thickness of the data in figure 7.2 (450 nm Al_2O_3 plus 100 to 200 nm SiO_2), the observed values agree with those found by Kim, et al[92]. Projecting the linear trend back to zero SiO_2 thickness results in a substrate thermal conductivity of 139 ± 3 W/m·K.

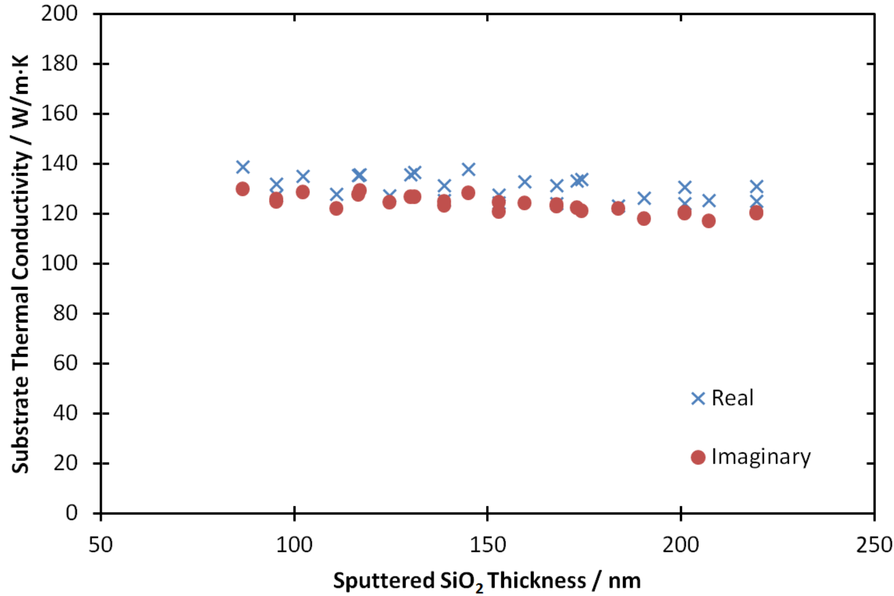

Figure 7.2: Comparison of the apparent substrate thermal conductivity as a function of sputtered SiO_2 film thickness. Data calculated using equations (2.51) (imaginary) and (2.52) (real) are shown.

7.3 SiO_2 Film Thermal Conductivity

The data in figure 7.3 demonstrate a linear relationship between heater temperature amplitude and sputtered film thickness, even at thicknesses as low as 100 nm, indicating that the film thermal conductivity was likely independent of film thickness. Using a linear fit, the intercept at zero sputtered film thickness can be used to determine the temperature contribution from the substrate, Al_2O_3 film and all interfacial thermal resistances.

While it has been reported that the thermal conductivity of SiO_2 thin films is thickness-dependent for thicknesses below approximately 250 nm[74, 73, 93], the linear dependence of temperature per unit power on film thickness demonstrated here suggests that the previous results may have been due to a thickness-independent interfacial contribution to the film thermal resistance that was not taken into account in earlier reports. The data in figure 7.4 show the results of two modes of analysis

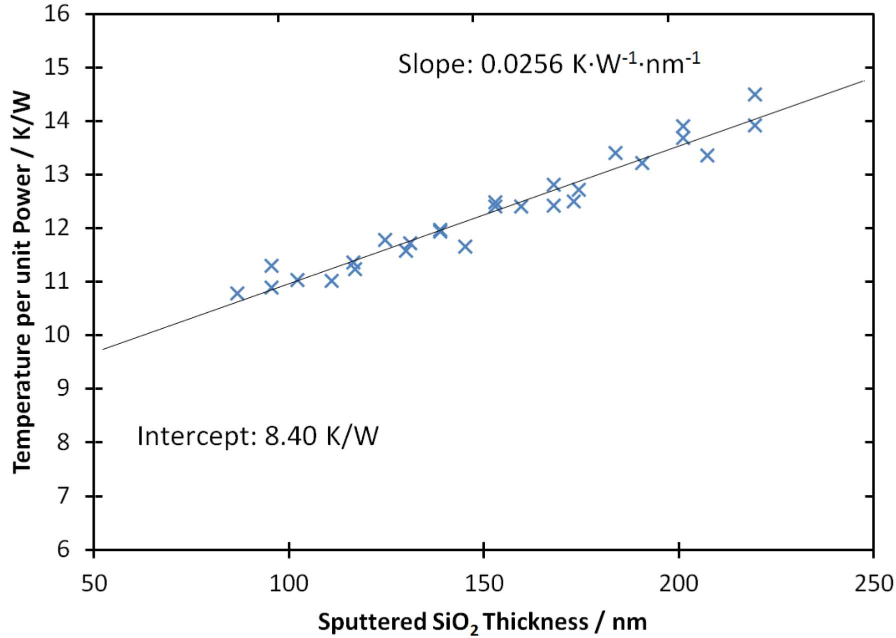

Figure 7.3: Temperature amplitude per unit power as a function of SiO_2 film thickness for all heaters on the SiO_2 wedge.

for finding κ_f, both of which account for the presence of an interfacial thermal resistance. Subtracting the substrate, interfacial, and Al_2O_3 layer contributions using the temperature per unit power intercept in figure 7.3, the thermal conductivity of the sputtered SiO_2 film was found to be constant for all thicknesses, at an average value of approximately 1.1±0.1W/m·K. This agrees with the value that is approached at higher thickness in the literature[92, 75].

Finally, a single value for the SiO_2 thermal conductivity was calculated using the slope from figure 7.3 and equation (2.54). This method also accounts for all interfacial thermal resistances. Using the slope of 0.026±0.001 W/K·nm, a heater length of 1.4 mm, and a heater half-width of 12.5 μm, the final, thickness-independent value for sputtered SiO_2 thin-film thermal conductivity was found to be 1.11±0.05 W/m·K.

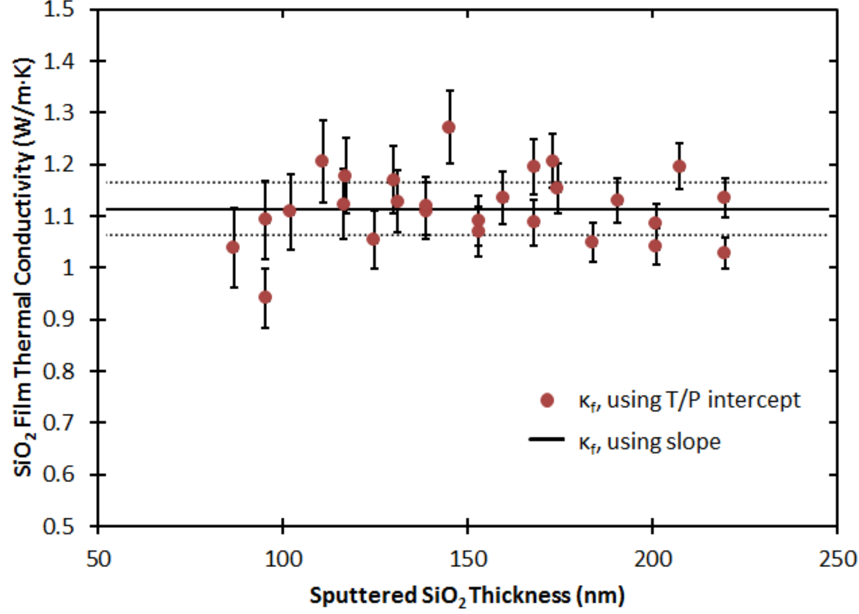

Figure 7.4: Film thermal conductivity as calculated for each heater on the SiO_2 wedge using two methods. To subtract the influence of the substrate and Al_2O_3, the temperature per unit power for a position with no SiO_2 was measured, and this value was subtracted from the data at each SiO_2 thickness. The dotted line indicates the error range for κ_f calculated using the slope in figure 7.3.

7.4 Interfacial Thermal Resistance

It is possible to calculate the magnitude of the difference in interfacial thermal resistance of Al_2O_3 on native oxide and Al_2O_3 on sputtered SiO_2 using the difference between the intercept determined in figure 7.3 and the temperature amplitude per unit power determined for a heater directly on Al_2O_3, using equation (2.56). In both cases the contributions from the substrate and films are the same, allowing a comparison of the interfacial contribution.

$$\Delta R = \left[R_{Sputtered/Al_2O_3} - R_{Native/Al_2O_3} \right] \frac{P}{2bl} \tag{7.1}$$

Using the intercept value of 8.40 K/W and the measured Al_2O_3-only heater temperature amplitude per unit power of 7.58 K/W, the difference in interfacial thermal

resistance was found to be $\sim 3 \times 10^{-8}$ K·m^2/W. For reference, this is approximately 10% of the total thermal resistance of $\sim 3 \times 10^{-7}$ K·m^2/W. It should be noted that this method assumes no interfacial contribution between the sputtered SiO_2 and the native oxide of the silicon wafer.

7.5 Temperature Dependence

A brief examination of the temperature dependence of the substrate and film thermal conductivities was undertaken. The entire wafer/PCB/holder assembly was heated to ∼100°C in an oven, and then allowed to cool slowly over several hours back to room temperature. 3ω measurements were taken for all heaters in a single 16-heater group during cooling. A sample of substrate thermal conductivity as a function of temperature is shown in figure 7.5 for three heaters in the group.

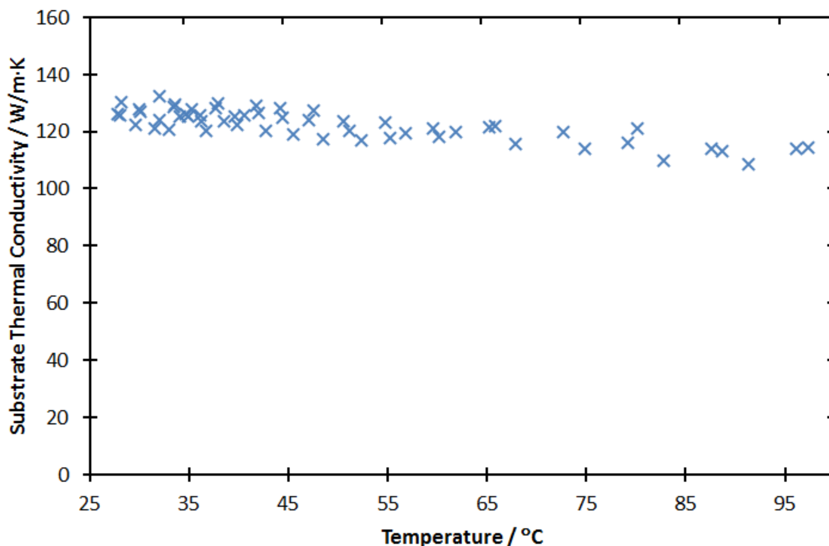

Figure 7.5: Silicon substrate thermal conductivity as a function of temperature for select devices on the SiO_2 wedge.

The vertical scatter in the plot is largely due to the variation in substrate thermal conductivity with SiO_2 film thickness, noted earlier. The range of temperatures was limited to a narrow band of values due to the sensitivity of plastic components used

in the construction of the combinatorial measurement system. This narrow range does not permit observation of a particular functional relationship between substrate thermal conductivity and temperature, but there is a clear downward trend with increasing temperature. This relationship is expected, as literature[94] shows silicon thermal conductivity decreasing in this temperature range due to increased phonon scattering.

7.6 SiO_2 Wedge Study Conclusions

In this proof-of-concept study, both the substrate thermal conductivity and film thermal conductivity of Si and SiO_2, respectively, were found to closely match the values found in the literature for comparable materials. This study demonstrated that the automated 3ω measurement system is capable of determining thin film thermal conductivity with a high degree of accuracy. In addition, the use of an e-beam-deposited Al_2O_3 layer to insulate patterned metal structures from a conductive substrate was demonstrated to be effective.

7.6.1 3ω Data Point Selection Criteria

The results of this wedge study were used to form a set of selection criteria for accepting or dismissing 3ω data points in the subsequent ZTO and ZIO thermoelectric experiments. To this end, the substrate thermal conductivity was calculated for every 3ω heater, and this calculated value was used as a check for the validity of the temperature amplitude per unit power value calculated at that point. This served to eliminate data from defective heater strips that may otherwise have appeared to provide 'reasonable' temperature amplitudes. Reasons why a heater strip might be defective include a 'short' between the metal and the sputtered film through the Al_2O_3 film, or poor metal adhesion causing a 'hot spot' in the heater.

Specifically, the substrate thermal conductivity, as calculated using both the real (equation (2.52)) and imaginary (equation (2.51)) methods, was required to be within

$\pm10\%$ of the 'expected' value based on the data in figure 7.2, and the measured thickness of the films for the sample and position being measured. Failure of a given heater to meet this criteria excluded the temperature amplitude data it provided from being used to calculate the thermal conductivity of the thin film at that point.

Following this study, the 3ω measurement system was ready for use on ZTO and ZIO thin-films.

Chapter 8

Zinc Tin Oxide Thermoelectric Study

Zinc tin oxide films sputtered under two different conditions were studied for the thermoelectric characterization component of the project. One was sputtered in the same manner as the transistor study, with a sputtering gas containing 90% argon and 10% oxygen, while the other was sputtered under 100% argon. The difference in electrical and thermal conductivity between these two conditions sheds light on the role of oxygen vacancies in the thermoelectric properties of these films.

8.1 90% Ar, 10% O_2 Sputtering Condition

8.1.1 Fabrication of 90% Ar, 10% O_2 Samples

Zinc tin oxide films were sputtered onto 100 mm diameter, heavily doped (< 0.005 $\Omega\cdot$cm) <100> silicon wafers. These wafers had only a native, self-passivated oxide on the surface. In order to electrically isolate the sputtered film from the substrate and to facilitate electrical conductivity measurements, a 200 nm Al_2O_3 film was e-beam evaporated onto each wafer prior to sputtering. The wafer was rotated during this deposition to ensure uniform thickness and avoid pinholes.

The SnO_2 and ZnO targets were sputtered at 40 W and 110 W, respectively, with a sputter gas pressure of 5 mTorr consisting of 90% Ar and 10% O_2. The targets were masked as in the TFT study, resulting in a sputtered film that would ideally vary from pure SnO_2 at the inside edge of the track, to pure ZnO at the outside edge. Each wafer was patterned during sputtering using a stainless steel stencil mask of the design in figure 3.1. Included on the table were mass disks, as well as silicon and glass strips to be used for microprobe, ellipsometry, X-ray diffraction and Seebeck

coefficient measurements. Total sputtering time was approximately four hours.

One wafer was annealed under oxygen for 30 minutes at 300°C and another at 600°C after sputtering, and prior to the deposition of Al_2O_3 insulating films and metal. A third wafer was left as-deposited. It should be noted that previous samples that were annealed after the patterning of heaters were found to exhibit very high rates of defects, and failed to produce useful results.

After annealing, the van der Pauw structures were covered with strips of aluminum foil, and 400 nm of Al_2O_3 was e-beam deposited at a rate of $\sim$0.2 nm/sec with the wafers rotating. After deposition of the Al_2O_3 insulating later, the wafers were patterned for lift-off using the mask in figure 3.2. A 'de-scum' step was performed after development, but prior to metal deposition, by exposing the wafer to a low-power oxygen plasma at 0.08 W/cm^2 in 150 mTorr of O_2 for 60 seconds. The de-scum step removed any remaining organic material left on the wafer surface from the patterning process, and improved metal adhesion.

Nickel was then e-beam deposited at a rate of 0.1 nm/sec to a total thickness of 320 nm. This thickness was calculated to give the current path for each heater a resistance of approximately 50 Ω. Prior to lift-off, the wafers were allowed to cool in vacuum for approximately 8 hours, and were then exposed to atmosphere for approximately 16 hours. Lift-off was then performed in Futurrex RR-5, followed by a rinse in de-ionized water. Finally, the wafers were blown dry with compressed air.

8.1.2 Physical Characterization of 90% Ar, 10% O_2 Samples

The ZTO films sputtered under partial oxygen were revealed to be slightly thicker than those used in the ZTO TFT study, with a thickness varying from 600 - 700 nm, with films thickest at the outside edges. The thicknesses of films both before and after annealing were compared, and no detectable change in film thickness was present. Therefore, the thickness profile presented in figure 8.1 was used for calculations on all three annealing conditions.

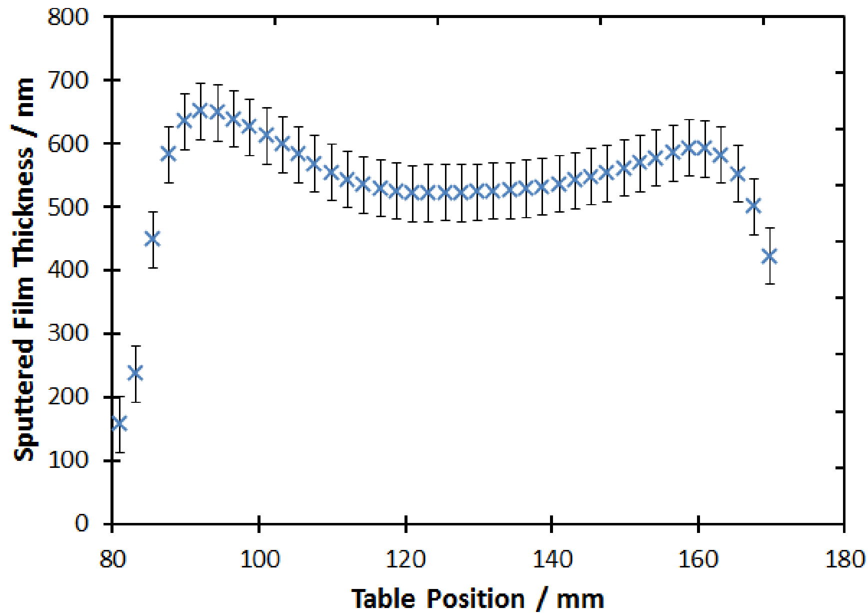

Figure 8.1: Measured thickness as a function of sputtering table position for ZTO films sputtered under 10% oxygen. Zinc oxide content increases with radial position.

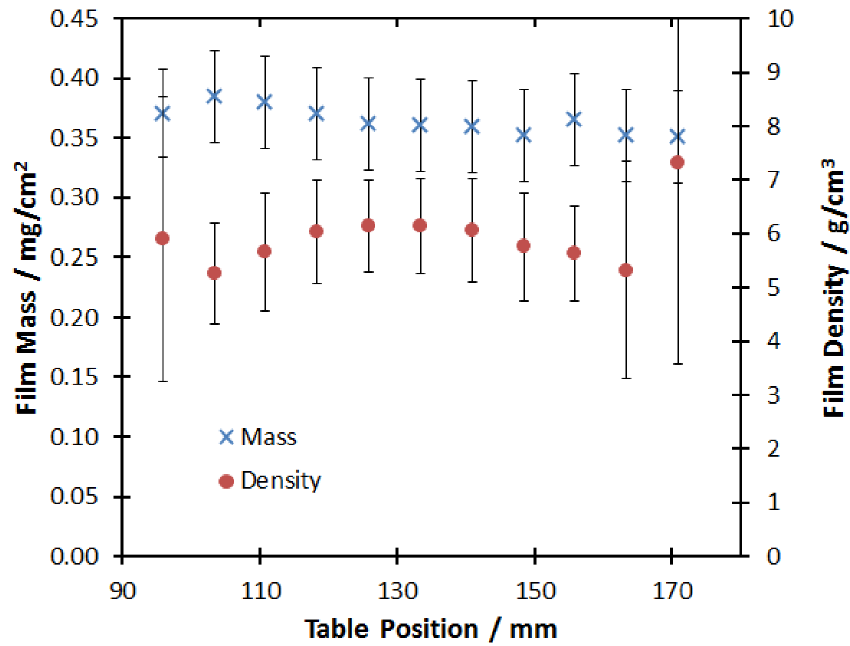

Figure 8.2: Film mass and density as a function of sputtering table position for ZTO films sputtered under 10% oxygen.

The mass and density of the film were determined using the difference between the pre- and post-sputtering mass of the aluminum foil disks as well as the thickness profile in figure 8.1, and results are presented as a function of table position in figure 8.2. The density of the film is relatively constant across the width of the sputtering track, and is generally confined to between 5 and 6 g/cm^3, except at the zinc-rich extreme. This range of values is consistent with the bulk density of ZnO (5.6 g/cm^3) and is slightly lower than the bulk density of SnO_2 (6.95 g/cm^3). Film mass is fairly constant across the range, decreasing slightly toward the outside (ZnO-rich) end of the range. The variation in thickness across the track was then due largely to changes in film density, and the film exhibited a broad peak in density around the middle of the sputtering track .

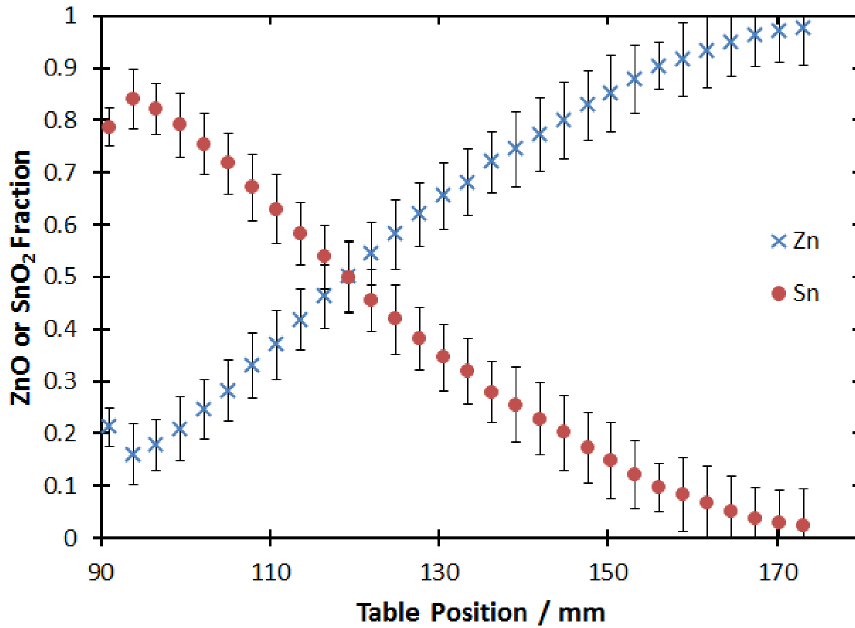

Figure 8.3: Relative atomic fraction of Zn and Sn as a function of radial position on the sputtering table for ZTO films sputtered under 10% oxygen.

WDS Microprobe of the sputtered film (figure 8.3) revealed it to vary between ∼85% Sn at the inner edge of the track to ∼98% Zn at the outer edge. Due to limitations in the photomask design that prevent heaters from approaching the extreme inner edge of the sputtering track, thermal conductivity data were only available for

ZnO fractions above 25%.

The ZnO sputtering rate and therefore the relative composition of the films led to a slightly more ZnO-rich sputtered film than that used in the ZTO TFT portion of the project. While the same targets, magnetron positions, tunnel masks and powers as the TFT study were used, the sputtering rate was changed likely due to magnetron replacements and the ZnO target aging due to its use for other studies in the intervening time.

8.1.3 Thermal Conductivity of 90% Ar, 10% O_2 Samples

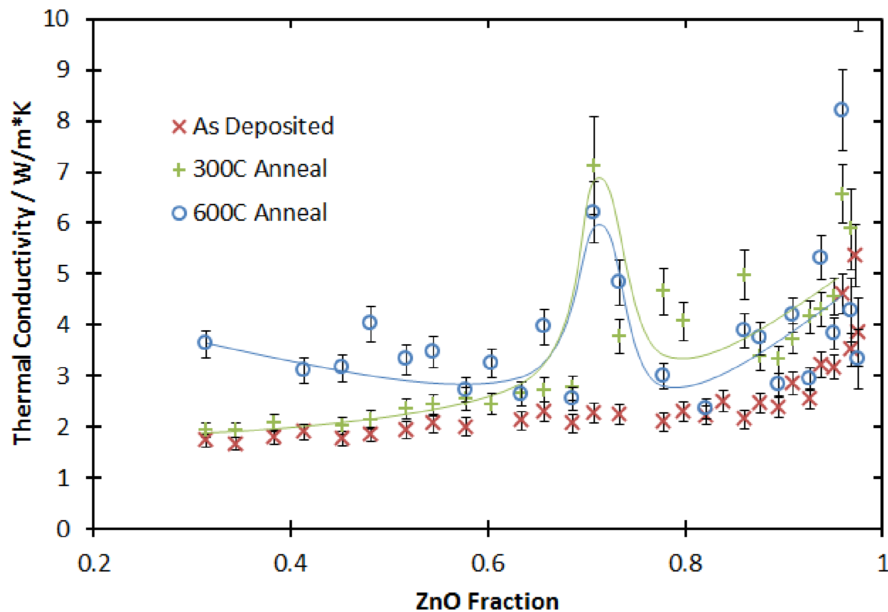

Figure 8.4: Thermal conductivity at room temperature as a function of zinc oxide fraction for ZTO films sputtered under 10% oxygen. Data for as-deposited, 300°C oxygen, and 600°C oxygen annealing conditions are presented. Note that the lines serve as a guide to the eye only.

The thermal conductivity of the as-deposited film as a function of ZnO fraction is presented in figure 8.4. The thermal conductivity of the film rises gradually, from approximately 1.5 W/m·K at the inner, 30% ZnO edge to approximately double that value at ~90% ZnO. However, above 90% ZnO the thermal conductivity of the film is

found to rise more sharply with increasing ZnO concentration. The measured values in this area range from 3 to 6 W/m·K, three to four times greater than those measured at the inner edge of the track.

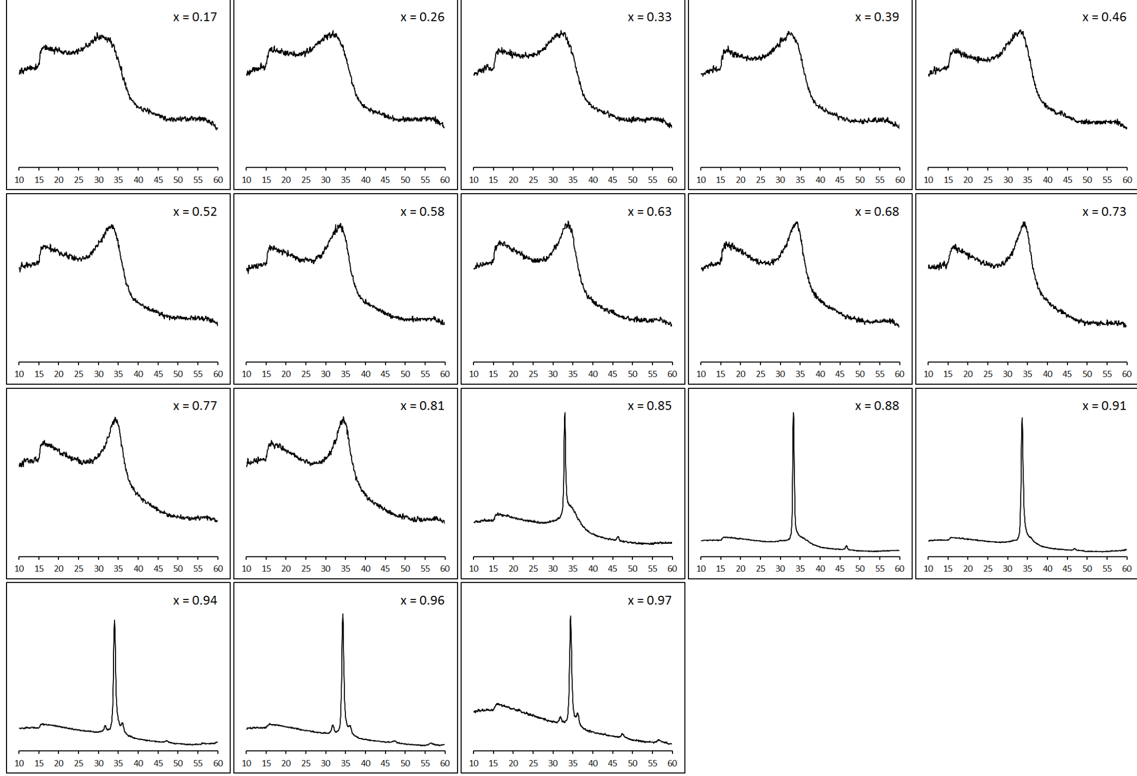

Figure 8.5: X-ray diffraction data for as-deposited ZTO films sputtered under 10% oxygen at multiple zinc oxide fractions x.

X-ray diffraction of the as-deposited film (figures 8.5 and 8.6) indicates the formation of a polycrystalline ZnO phase for $x \geq 0.85$. The formation of this phase is the likely cause of the increase in thermal conductivity in this range. While the peak positions of this phase are consistent with ZnO, the relative peak heights do not reflect those expected of a powder ZnO sample[95, 96, 97, 98], indicating a preferred orientation to the lattice relative to the substrate. In addition, a systematic shift of the peaks indicates distortion of the lattice. Xu et al. report the growth of column-shaped crystalline grains growing perpendicular to the substrate surface for ZnO films sputtered under oxygen. The thermal conductivities reported are also

similar to those observed near the pure ZnO extreme.[99]).

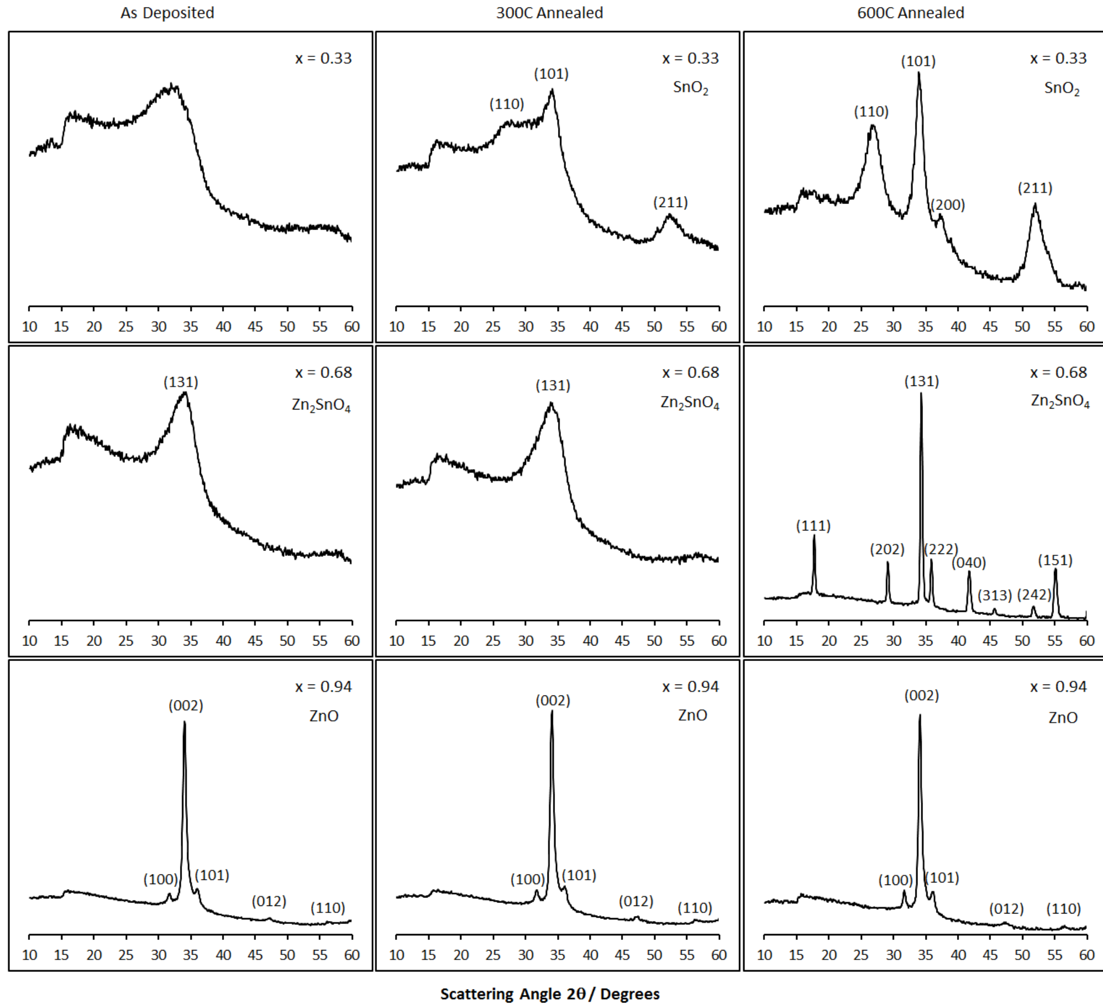

Figure 8.6: Comparison of XRD data for selected zinc oxide fractions of ZTO films sputtered under 10% oxygen, for as-deposited, 300°C under oxygen and 600°C under oxygen annealing conditions.

Figure 8.6 shows selected XRD plots in more detail. Miller indices are marked for the ZnO phase discussed above. In the tin-rich end of the range (x < 0.5, represented by the $x = 0.33$ plot) little evidence of a distinct SnO_2 phase is visible. At $x = 0.68$ there is a broad peak at $2\Theta = 35°$ that may correspond to the (131) peak of a Zn_2SnO_4 phase.

Films annealed at 300°C under oxygen exhibit a slight increase in thermal conductivity compared to the as-deposited films for $x < 0.7$ (figure 8.4). The magnitude

of this difference increases somewhat with increasing ZnO content, with films at the upper end of this range being 50% more thermally conductive than their as-deposited counterparts, at 3 W/m·K. Measurements for films between ZnO fractions of 0.7 and 0.85 exhibit an increased amount of scatter, and the annealed films in this range are significantly more thermally conductive than their as-deposited counterparts.

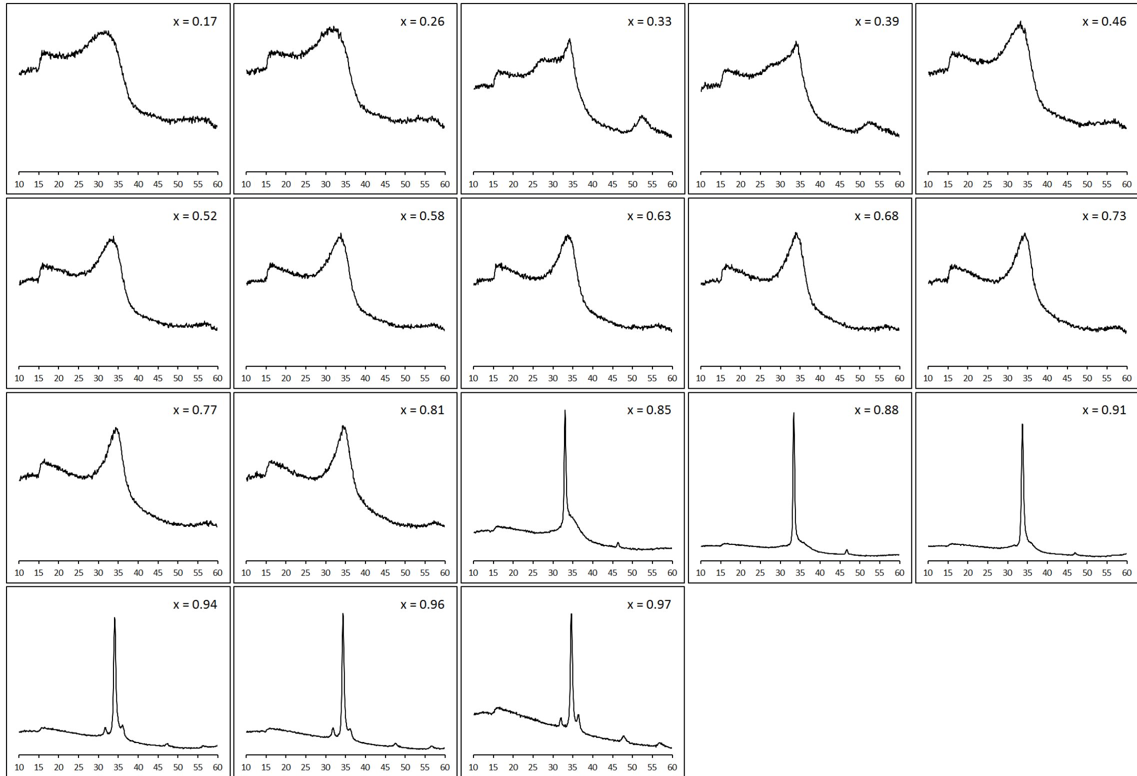

Figure 8.7: XRD results for ZTO films deposited in 10% oxygen and annealed at 300°C under oxygen.

XRD results for this sample (figures 8.7 and 8.6) are similar to the as-deposited films, though with some enhancement of the peak heights. Weak peaks corresponding to a SnO_2 phase are visible for $x < 0.5$. The ZnO phase becomes slightly more distinct, and this is reflected in the thermal conductivity in ZnO-rich films; the peak thermal conductivity as the pure-ZnO extreme is reached is slightly higher than in the as-deposited films.

After annealing, the $0.7 < x < 0.85$ region of the film was visibly cloudy, and was

also ‘rough’ in appearance (figure 8.8). This might indicate an increase in organization of the film in this region and the peak in thermal conductivity at this stoichiometry. Only a very slight enhancement of the possible (131) Zn_2SnO_4 peak is visible in the XRD data, however.

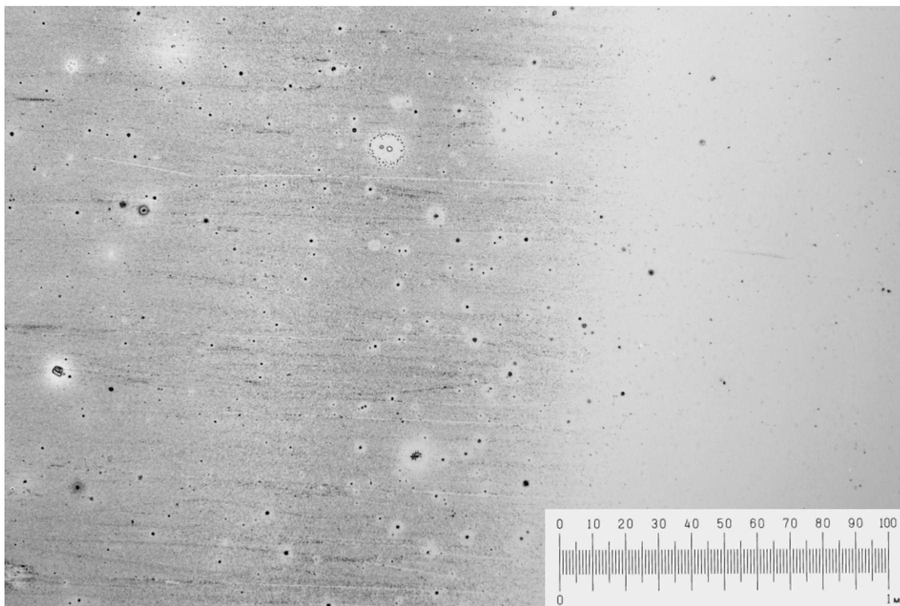

Figure 8.8: An optical image of the ‘rough’ area (left) and normal, ‘smooth’ area (right) on the 300°C annealed film for zinc oxide fractions of 0.7 < x < 0.85. The change in character is abrupt, occurring over a radial distance of less than 1 mm.

Annealing at 600°C produced a film that was significantly more thermally conductive in the $x < 0.5$ range than either the as-deposited or 300°C annealed films (figure 8.4). Similar to the 300°C film, a peak in thermal conductivity is visible around $x = 0.7$. Above $x = 0.85$, a rise in thermal conductivity with increasing ZnO content is observed, similar to the other two samples.

The ‘cloudy’ appearance of the film between $0.7 < x < 0.85$ was very similar to figure 8.8. XRD for this film (figure 8.9) exhibits a number of differences compared to the other annealing conditions. In this annealing condition a phase of Zn_2SnO_4 is clearly visible (figure 8.6) at the $x = 0.68$ stoichiometry, and this phase is aligned with the peak in thermal conductivity observed at the same zinc content value. In addition, the weak phase visible for $x < 0.5$ in the other annealing conditions is now

a clear SnO_2 phase, and this phase results in an increase in thermal conductivity for $x < 0.5$ compared to the other two films, approximately doubling it.

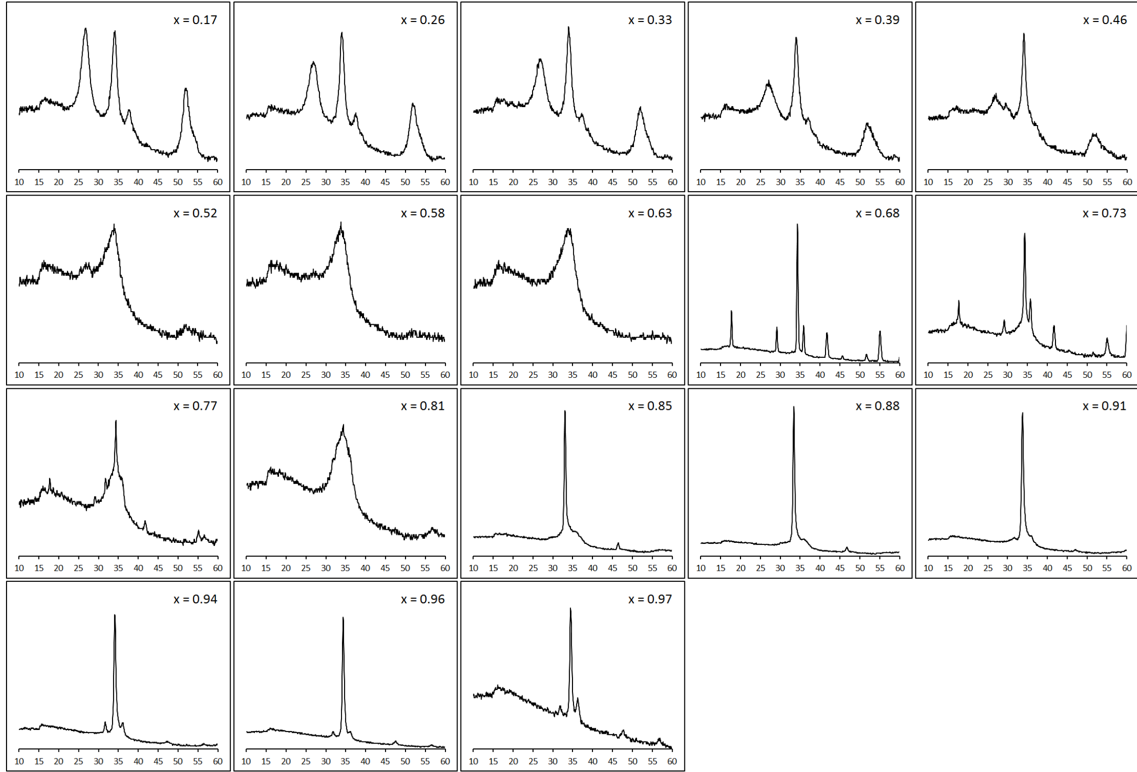

Figure 8.9: XRD results for ZTO films deposited in 10% oxygen and annealed at 600°C under oxygen. Three phases are visible across the range, one below $x = 0.5$, another around $x = 0.68$ and finally the ZnO phase observed earlier. A closer examination of these phases is shown in figure 8.6.

The phase of ZnO is still present near the zinc-rich extreme. This phase now appears to be very strongly oriented, with the height of the (002) peak relative to the other visible peaks even more pronounced than in either of the other conditions.

8.1.4 Electrical Conductivity of 90% Ar, 10% O_2 Samples

As-deposited, ZTO films sputtered under 10% oxygen were found to be highly resistive, and the electrical conductivity of these films could not be accurately measured.

The electrical conductivity of the 300°C annealed films (figure 8.10) were significantly higher than the as-deposited films. The data exhibit a trough in conductivity

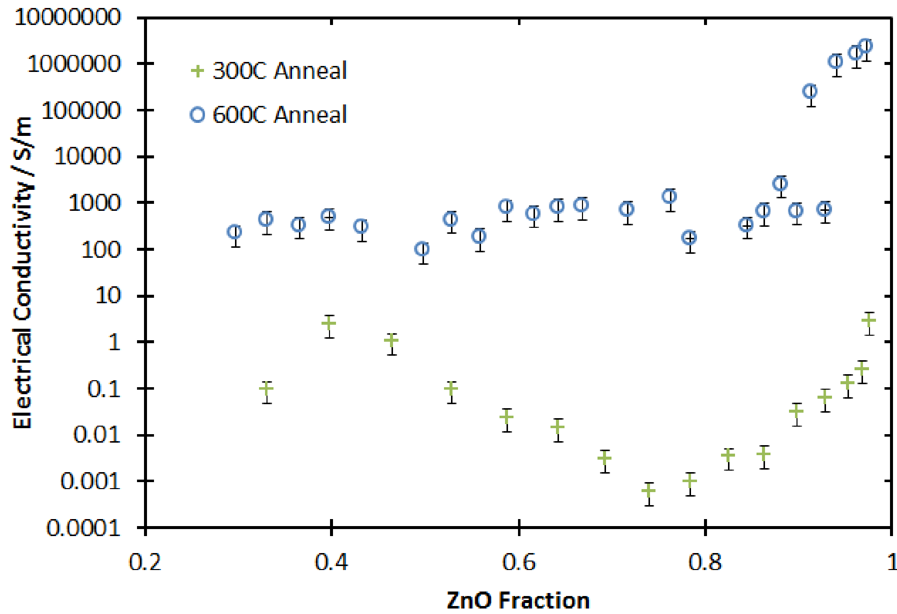

Figure 8.10: Electrical conductivity as a function of zinc oxide fraction, for ZTO films sputtered under 10% oxygen and annealed under oxygen at 300°C and 600°C.

at a ZnO fraction of approximately 0.7, increasing by approximately 3 orders of magnitude toward the extremes of the stoichiometric range. While not necessarily related, it is worth noting that the trough in electrical conductivity coincides with the 'cloudy' area of the film that was formed during the annealing process. Even in the most electrically conductive areas of the stoichiometric range, the conductivity is relatively low, not much exceeding 1 S/m.

In the case of the 600°C annealing condition (figure 8.10), the electrical conductivity is significantly higher for all compositions. The trough observed at the 300°C annealing condition is absent, and the electrical conductivity of the film appears to increase with zinc oxide fraction. However, this variation is very gradual, representing only a factor of two increase between zinc oxide fractions of 0.3 and 0.9. Mixtures composed of 95% ZnO or more appear to be much more electrically conductive, with values approximately three orders of magnitude higher than those across the rest of the range.

The variation in electrical conductivity with stoichiometry for the 600°C sample

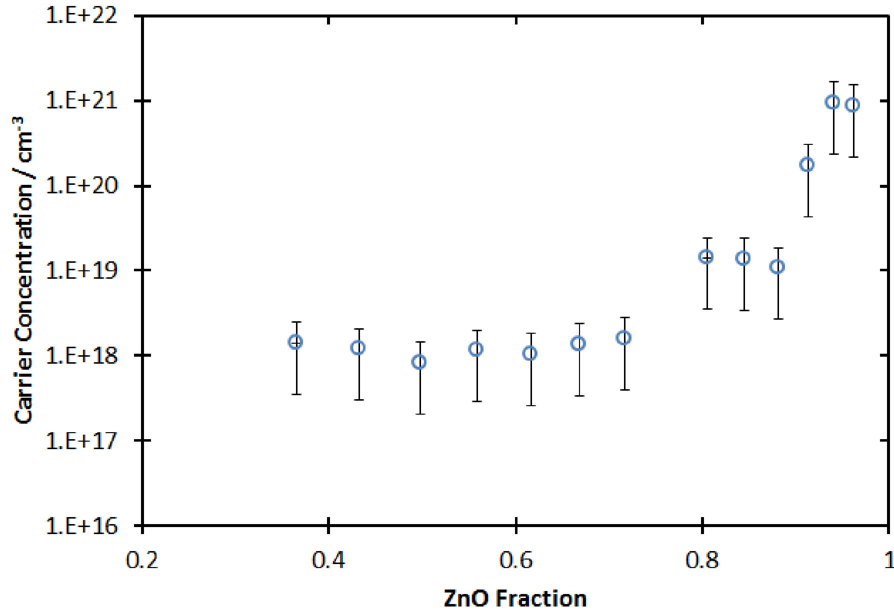

Figure 8.11: Charge carrier concentration as a function of stoichiometry for the 600°C annealing condition of ZTO sputtered under 10% oxygen.

appears to be largely due to an increase in available mobile charge carriers (figure 8.11). Carrier concentration as a function of stoichiometry closely mirrors electrical conductivity, with a Hall mobility on the order of 50 $cm^2/V{\cdot}s$ over the measured range. The magnitude of the Hall voltage for the 300°C sample was very small using the available magnet and current sources, even at the stoichiometries with the highest conductivity, preventing an accurate measurement of carrier concentration.

8.1.5 Seebeck Coefficient of 90% Ar, 10% O_2 Samples

Measurement of the Seebeck coefficient was carried out for selected stoichiometries for both annealing conditions and are presented in figure 8.12. While measurements of the Seebeck coefficient were attempted on the as-deposited films, their resistive nature prevented an accurate reading.

The measured values are all negative (n-type), as expected from the TFT study in chapter 6. The 300°C annealing condition produced large-magnitude Seebeck coefficients of -130, -250 and -120 μV/K at 300 K for $x = 0.2$, 0.45 and 0.95, respectively.

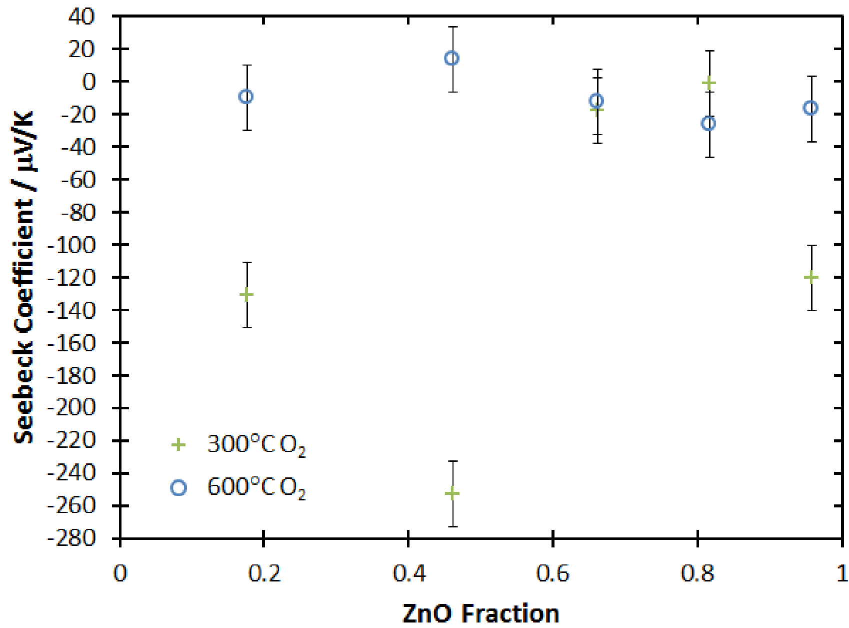

Figure 8.12: Seebeck coefficients for all ZTO films sputtered under 10% oxygen. The $x = 0.2$, 0.45 and 0.95 stoichiometries in the 300°C annealing condition all produced relatively high magnitude Seebeck coefficients, with $x = 0.45$ measured to be -250 μV/K.

These values are comparable to those of bismuth telluride (-230 μV/K) or lead telluride (-180 μV/K). However, Seebeck coefficients for films in the area of low electrical conductivity ($0.6 \leq x \leq 0.9$) are zero within experimental uncertainty.

Interestingly, the more thermally conductive 600°C films all have low-magnitude Seebeck coefficients, indicating that the strong crystallization of the films observed in XRD measurements significantly decreased the electron-phonon coupling in these materials.

8.1.6 Thermoelectric Figure of Merit

Using the thermal and electrical conductivities discussed earlier, a dimensionless figure of merit was calculated at each stoichiometry and annealing condition for which a measured Seebeck coefficient was available. A value of 300 K was used for T.

Despite the fact that the value of the thermoelectric figure of merit is most sensitive

Table 8.1: Calculated dimensionless figures of merit for ZTO films sputtered under 10% oxygen and annealed at 300°C and 600°C under oxygen. A temperature of 300 K was used for all measurements. Calculated for T = 300 K.

300°C O_2	x	0.18	0.46	0.66	0.81	0.96
	ZT	-	(9±5)x10^{-7}	(1±1)x10^{-10}	(0.4±0.6)x10^{-12}	(2±1)x10^{-7}
600°C O_2	x	0.47	0.64	0.78	0.90	0.98
	ZT	(0.5±1)x10^{-6}	(2±2)x10^{-5}	(3±4)x10^{-5}	(2±2)x10^{-5}	0.06±0.07

to Seebeck coefficient, it is clear in table 8.1 that the very low electrical conductivity of the 300°C annealed films result in very low values of ZT, despite the relatively low thermal conductivity and relatively high magnitude Seebeck coefficients of these films. The highest calculated value for ZT in a 600°C annealed film was 0.06±0.07 at high zinc concentration, again largely due to the electrical conductivity of this film, and in spite of a relatively low (-20 μV/K) Seebeck coefficient. While a value for ZT of 0.06 is quite high, there is high uncertainty on this value due to the low Seebeck coefficient. ZT across the rest of the range is lower than this pure-ZnO value.

8.2 Effective Lorenz Number

Table 8.2: Calculated effective Lorenz numbers for ZTO films sputtered under 10% oxygen and annealed at 300°C and 600°C under oxygen. A temperature of 300 K was used for all measurements. Calculated for T = 300 K.

300°C O_2	x	0.18	0.46	0.66	0.81	0.96
	$L_{eff}/\frac{W\Omega}{K^2}$	-	(7±4)x10^{-2}	3±1	4±2	(8±4)x10^{-2}
600°C O_2	x	0.47	0.64	0.78	0.90	0.98
	$L_{eff}/\frac{W\Omega}{K^2}$	(2±1)x10^{-5}	(1±0.5)x10^{-5}	(6±3)x10^{-5}	(3±1)x10^{-5}	(5±3)x10^{-8}

Effective Lorenz numbers calculated for ZTO films sputtered under oxygen are

presented in table 8.2. The low electrical conductivity of these samples results in very large L_{eff} (and therefore very non-metallic behaviour) at virtually all stoichiometries for both annealing conditions. The exception to this is a in the 600°C annealing condition near the pure-ZnO extreme, where L_{eff} approaches the ideal value of 2.45 x10^{-8} W·Ω/K^2, and the thermal conductivity is primarily dominated by the influence of charge carriers.

8.3 100% Ar Sputtering Condition

8.3.1 Fabrication of 100% Ar Samples

In order to study the effect of oxygen content during sputtering and annealing, a set of films similar to those discussed so far was sputtered using similar conditions, but under 100% argon.

In an effort to expedite the fabrication process and reduce the likelihood of electrical contact between the van der Pauw structures and silicon substrate, this later set of samples used heavily doped silicon wafers with 300 nm of thermal oxide on the surface. These 100 mm, <100> wafers were heavily doped (< 0.005 Ω·cm). The presence of thermal oxide on the wafer eliminated the need for the pre-sputtering Al_2O_3 deposition step.

Zinc tin oxide films were sputtered using the same ZnO and SnO_2 targets, at powers of 110 W and 40 W, respectively. It had been observed when making other samples that sputtering under pure argon would result in significantly higher deposition rates for a given power than when sputtering with 10% oxygen. As a result, the sputtering time was shortened to approximately two hours. The stencil masks used were the same as in the previous ZTO sputtering run. Again, mass disks, silicon strips and glass strips were included with the wafers on the sputtering table.

Two samples from this set were annealed at 600°C, one under pure oxygen and the other under pure argon. A third sample was left as-deposited. After annealing, the van der Pauw structures were covered while 400 nm of Al_2O_3 was deposited with the

wafers rotating. Patterning for lift-off followed the same procedure used in fabricating previous ZTO samples. However, the metal used in this set of samples was aluminum, which was deposited using thermal deposition from a tungsten filament, to a total thickness of 150 nm. Due to the higher conductivity of aluminum compared to nickel, this lower metal thickness resulted in the same average current path resistance for each heater of approximately 50 Ω.

Aluminum is not susceptible to the same adhesion issues observed with nickel, so neither the long cooling stage nor the long atmospheric exposure was necessary. After aluminum deposition, the wafer was immediately removed from vacuum and lift-off was performed in RR-5.

8.3.2 Physical Characterization of 100% Ar Samples

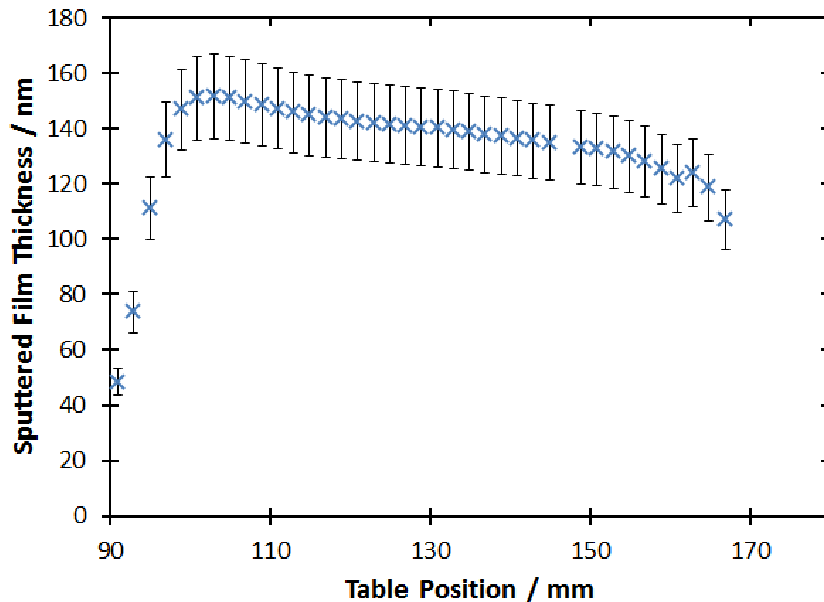

Figure 8.13: Measured thickness of ZTO films sputtered under argon as a function of radial position on the sputtering table. Zinc oxide content increases with radial position.

The thickness of the ZTO films sputtered under argon (figure 8.13) was somewhat

lower than was expected. It had been observed in earlier sputtering runs that deposition rates for a given chamber pressure with partial oxygen were significantly lower than for the same pressure of pure argon. Because the ZnO target was approaching end-of-life and there was concern that it would sputter through to the copper mounting plate and contaminate the samples, the sputtering time was halved compared to the partial oxygen run. Unfortunately, the low thickness of the films significantly increased the scatter in the thermal conductivity results.

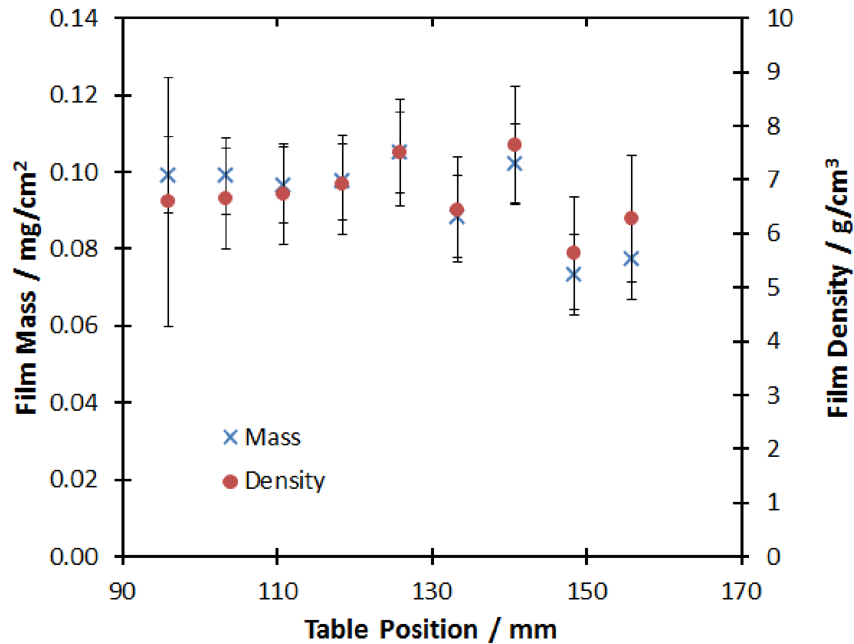

Figure 8.14: Film mass and density as a function of table position for ZTO films sputtered under argon.

The mass disk data show total deposited film mass per unit area varying similarly to film thickness, decreasing approximately linearly by ~20% from the inner to the outer edge of the track (figure 8.14). Film density is effectively constant, and lacks the broad peak around the middle of the track observed in the partial-oxygen sputtering condition. The films for the argon sputtering condition are also more dense, varying from 6-7 g/cm^3, as opposed to 5-6 g/cm^3 when sputtered under partial oxygen.

The range of sputtered stoichiometries (figure 8.15) is similar to the samples sputtered in 10% oxygen, ranging from 15% ZnO at inner edge, to 95% ZnO at the outer

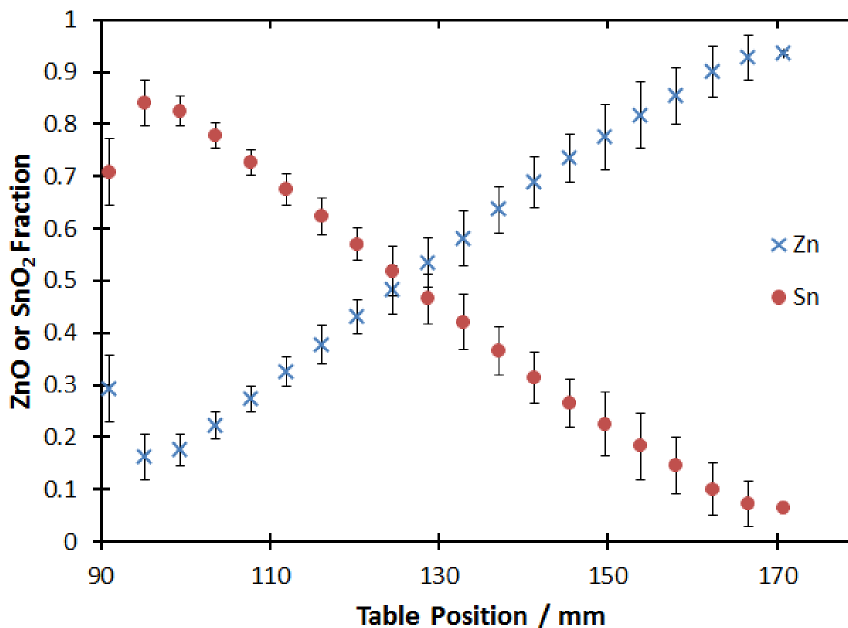

Figure 8.15: Normalized atomic fractions of Zn and Sn as a function of radial position on the sputtering table for the 100% argon sputtering run.

edge. There was concern that the thin nature of the films would require a correction to the microprobe data using Casino, as in the ZIO TFT study. However, WDS microprobe measurements for silicon showed negligible silicon signal, indicating that electron beam penetration was not sufficient to reach the underlying SiO_2/Si substrate. Therefore, the microprobe data were used as collected.

8.3.3 Thermal Conductivity of 100% Ar Samples

The thermal conductivity of the as-deposited film is presented in figure 8.16. The thermal conductivity is approximately constant at 2 W/m·K for zinc oxide fractions between 0.5 to 0.9. For zinc oxide fractions below 0.5, the measured thermal conductivity rises and peaks at $x \approx 0.4$, then decreases down to approximately 1 W/m·K for a zinc oxide fraction of 0.2.

X-ray diffraction of the as-deposited film (figure 8.17) showed very little structure at the majority of stoichiometries, with an amorphous profile for all $x < 0.9$. At the zinc-rich end of the extreme however, the weak, single peak shown in figure 8.18 is

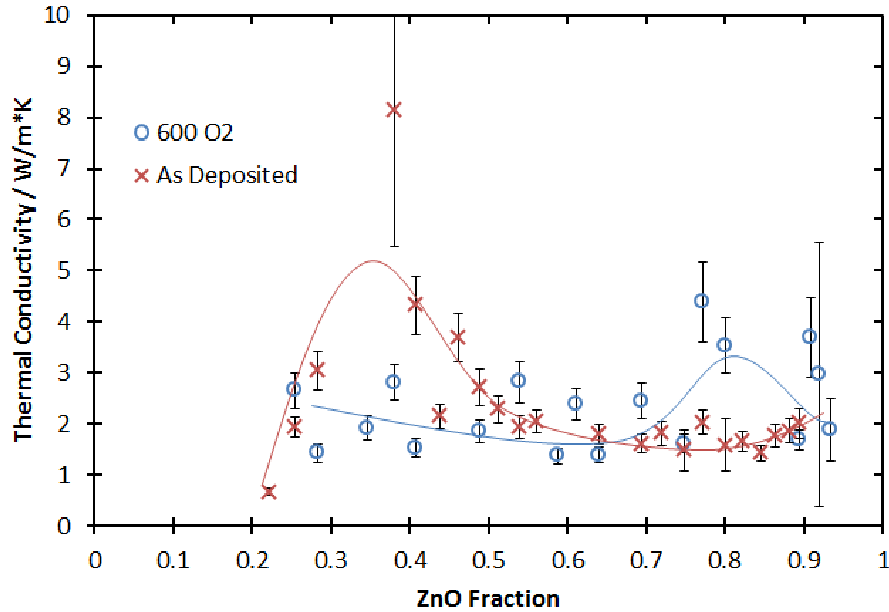

Figure 8.16: Thermal conductivity at room temperature of ZTO films sputtered under pure argon, for the as-deposited and 600° oxygen annealing conditions, presented as a function of zinc oxide fraction.

visible. This peak is likely the same (002) ZnO peak observed in the oxygen-sputtered films, indicating that the preferred-orientation growth of ZnO grains was present regardless of oxygen content. The broad peak in thermal conductivity observed around $x = 0.4$ does not seem to correspond to formation of a crystalline phase.

In the 600°C under oxygen annealing conditions, the peak in thermal conductivity observed at a zinc oxide fraction of 0.4 in the as-deposited data is not present (figure 8.16). Instead, the thermal conductivity is constant across most of the range at an average value of approximately 2 W/m·K, increasing slightly around the zinc-rich extreme. These data are not unlike those observed for ZTO sputtered under 10% oxygen and annealed at 600°C under oxygen.

The same three phases of SnO_2, Zn_2SnO_4 and ZnO present in the oxygen-sputtered film are also visible at approximately the same stoichiometric ratios (figure 8.18) in this film. The lower film thickness used in this condition is responsible for the lower

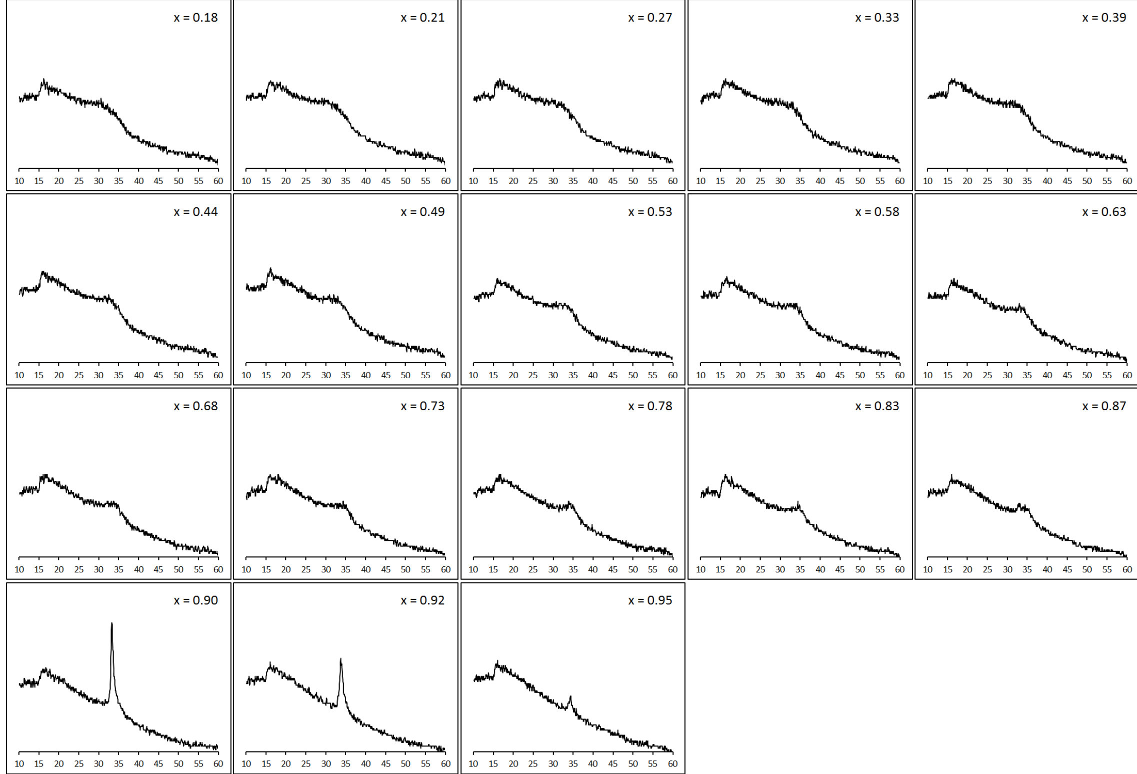

Figure 8.17: XRD results for as-deposited ZTO films deposited in argon at a variety of zinc oxide fractions.

signal to noise ratio in these measurements compared to those made on oxygen-sputtered films.

While the measured thermal conductivity of the films is presented in figure 8.20, the data cannot be relied upon for an accurate measure of film thermal conductivity. The temperature per unit power data for this sample are also presented, along with the accompanying temperature amplitudes for the adjacent reference heaters. The difference between the two amplitudes is effectively zero within experimental uncertainty, and indicates the presence of a film too thermally conductive for the current technique to measure.

XRD results for the 600°C, argon-annealed film are presented in figures 8.21 and 8.18. Like the 600°C, oxygen-annealed films, a ZnO phase is visible near the zinc-rich extreme, and a Zn_2SnO_4 phase is formed around the $x = 2/3$ stoichiometry. However, for tin-rich stoichiometries of $x < 0.5$, two superimposed phases are visible.

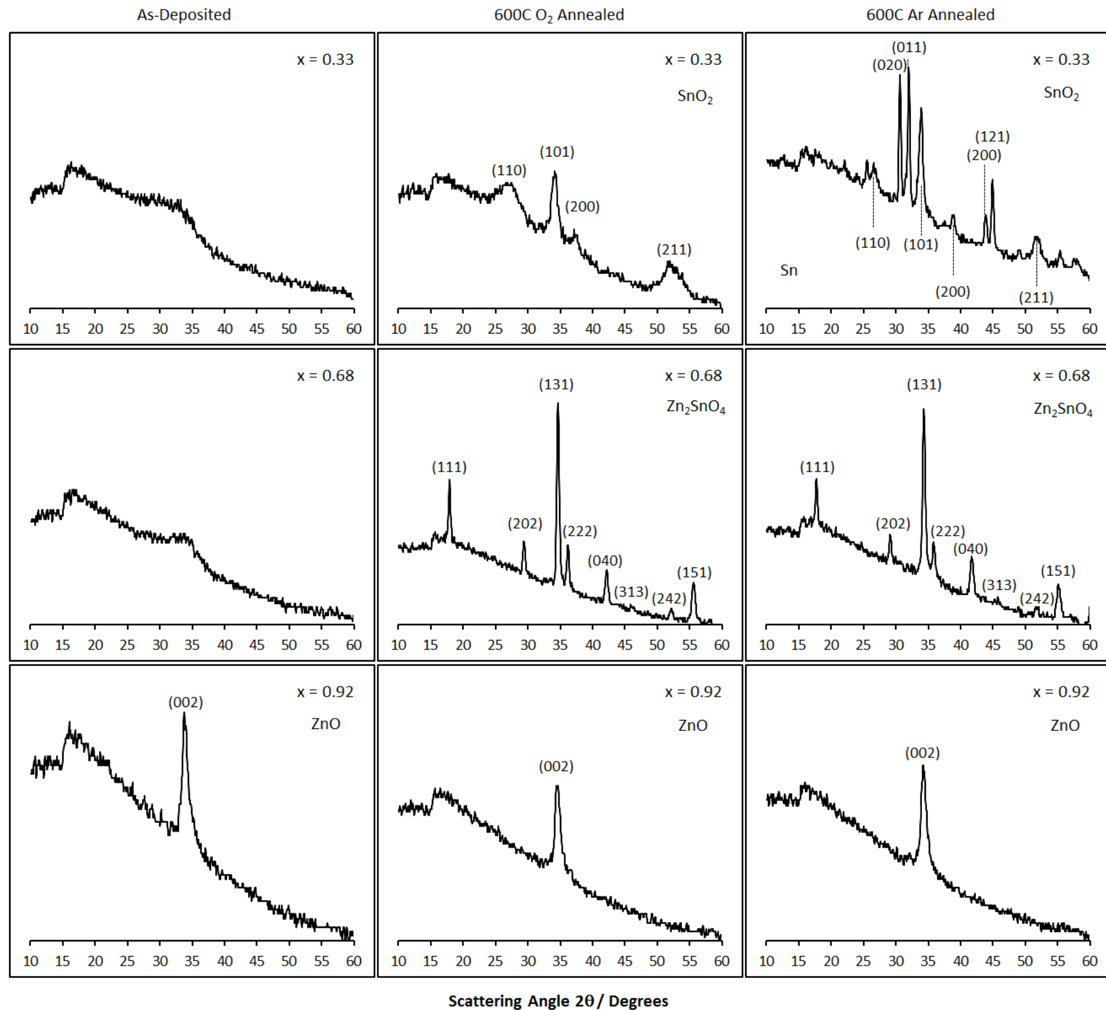

Figure 8.18: Larger plots of XRD data for ZTO films sputtered under argon for selected zinc oxide fractions, and all annealing conditions.

The tin(iv) oxide phase seen in the oxygen annealing conditions is still clearly visible, however it is now accompanied by a co-phase of tin metal. The formation of this extra phase is likely due to oxygen deficiency in the film.

8.3.4 Electrical Conductivity of 100% Ar Samples

In contrast to the films sputtered under 10% oxygen, the films sputtered under pure argon are significantly more electrically conductive as-deposited (figure 8.22). There is a broad peak in electrical conductivity around a zinc oxide fraction 0.4, with a

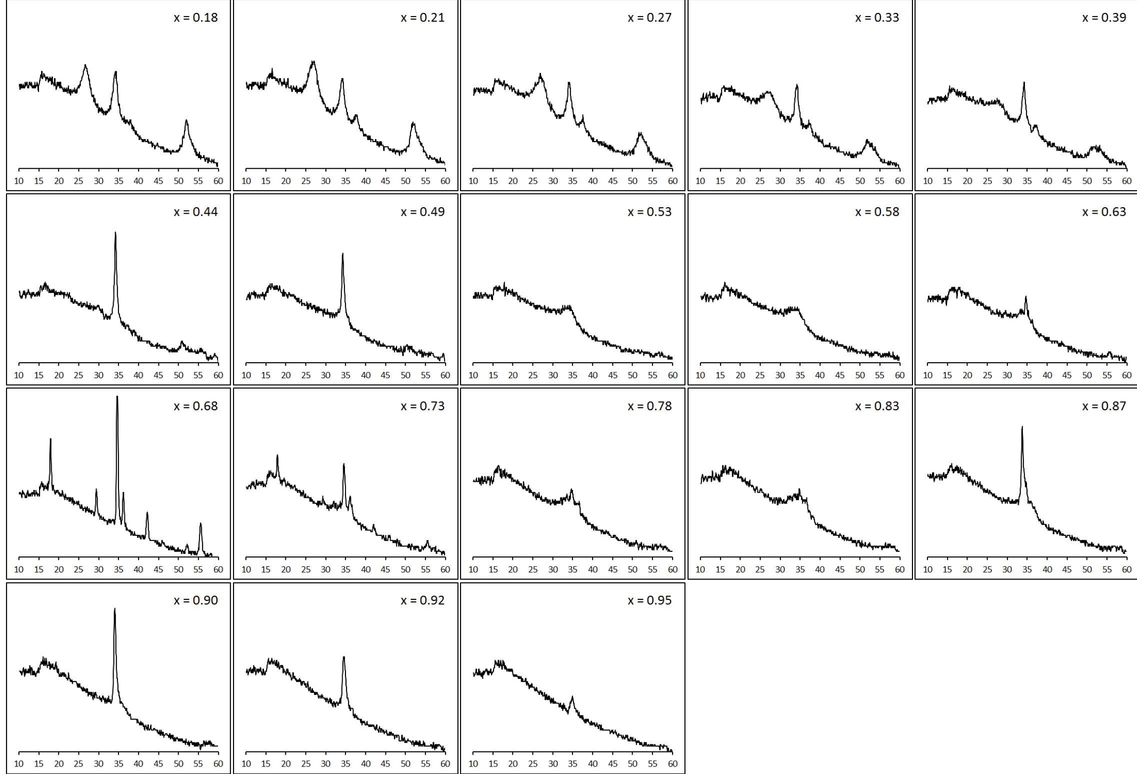

Figure 8.19: XRD results for ZTO films deposited in argon and annealed at 600°C under oxygen.

maximum of ∼100 S/m. The data include a precipitous drop for lower ZnO concentrations, and a gradual decline for greater concentrations. This decline continues into a broad minimum of 10 S/m at a ZnO fraction of 0.8, above which electrical conductivity rapidly increases with increasing ZnO content. Note that the data in figure 8.22 were taken using van der Pauw measurements of films on glass, instead of the patterned structures on the wafer. The broad peak in thermal conductivity observed in the as-deposited film around $x = 0.4$ mirrors the broad peak in electrical conductivity around the same stoichiometry, suggesting that thermal transport via electrons is dominant around this stoichiometry.

Annealing under oxygen (figure 8.22) results in an increase in electrical conductivity for SnO_2-rich films of approximately one order of magnitude, below a ZnO fraction of approximately 0.4, likely due to the increase in order in this region (see figures 8.17

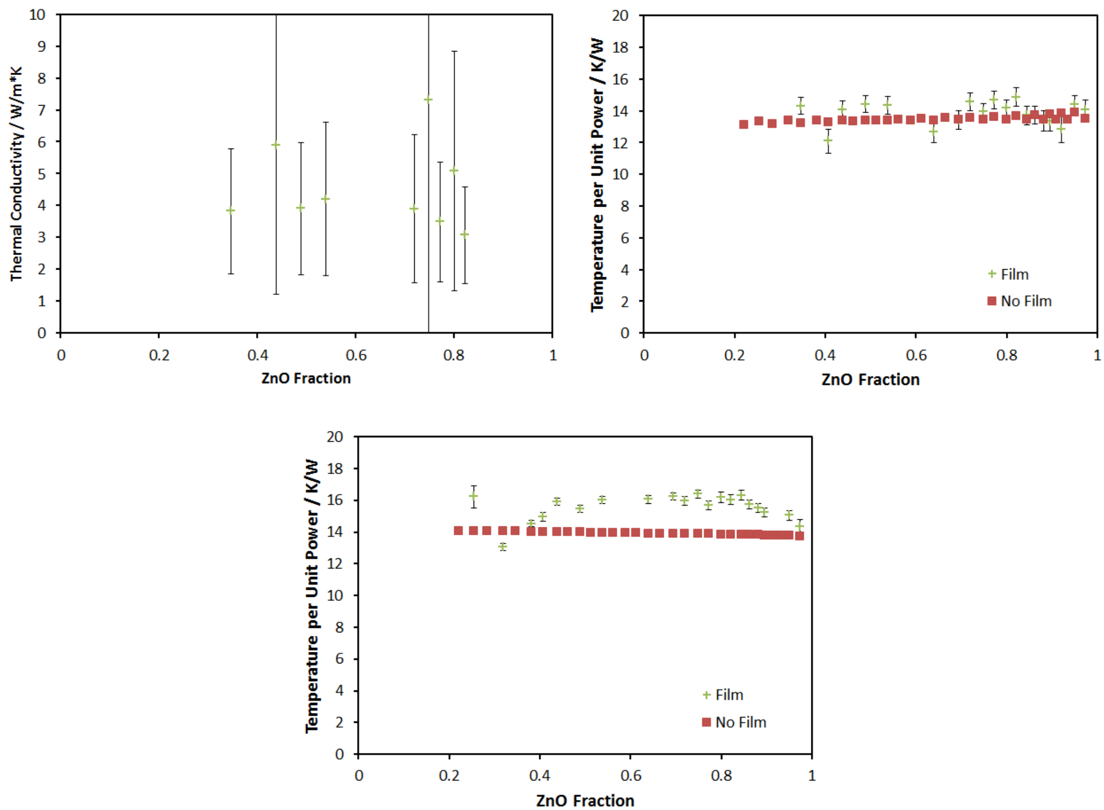

Figure 8.20: (Top Left) Thermal conductivity of films annealed at 600°C under argon, as a function of zinc oxide fraction. (Top Right) Temperature amplitude per watt for both the heaters on 600°C Ar-annealed films and their adjacent 'reference' heaters. (Bottom) For comparison, temperature amplitude per watt for both the heaters on as-deposited ZTO films sputtered under argon and their adjacent 'reference' heaters.

and 8.19) causing an increase in the electron mean free path. However, the ZnO-rich end of the sample exhibits a drop in electrical conductivity of the same order, with a slight decrease for films with a ZnO fraction above 90%. Despite the thermal conductivity and XRD results for this film being similar to those of the equivalent oxygen-sputtered film, the thermal conductivity is significantly higher across the entire range. This is particularly true for tin-rich mixtures. These results support the hypothesis that electrical conductivity in these films is largely the result of doping due to oxygen deficiency.

An apparent 'trough' in electrical conductivity is visible around the stoichiometries for which a Zn_2SnO_4 phase was seen to form.

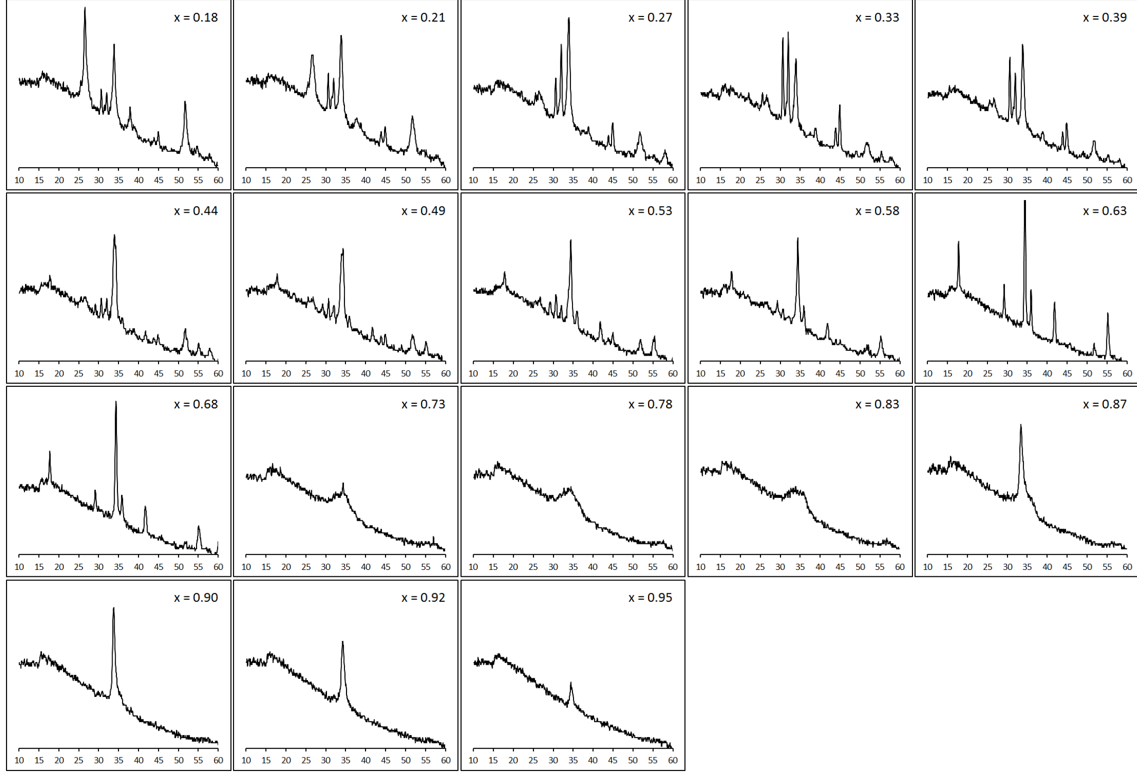

Figure 8.21: XRD results for ZTO films deposited in argon and annealed at 600°C under argon.

Films annealed under argon (figure 8.22) exhibit a relationship between stoichiometry and electrical conductivity that resembles the one observed for the as-deposited films. However, the argon-annealed film is significantly more conductive, by as much as two orders of magnitude below $x = 0.5$. However, similar to the oxygen-annealed films, a trough in electrical conductivity around $x = 0.7$ coincides with the formation of the Zn_2SnO_4 phase. Above this trough the argon-annealed film remains more thermally conductive than the as-deposited film, though the gap closes as x approaches 1.

The effect of oxygen deficiency on carrier concentration can be seen in figure 8.23. The as-deposited films exhibit the highest carrier density, despite also exhibiting the lowest electrical conductivity, indicated that their largely amorphous nature limits mobility. Annealing lowers the carrier concentration significantly, by as much as

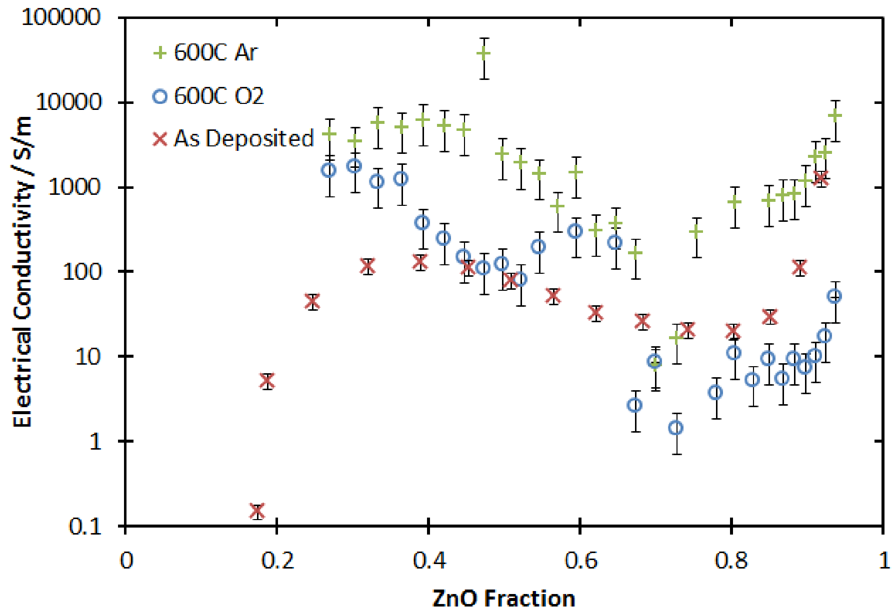

Figure 8.22: Electrical conductivity of ZTO films sputtered under argon as a function of zinc oxide fraction for all annealing conditions.

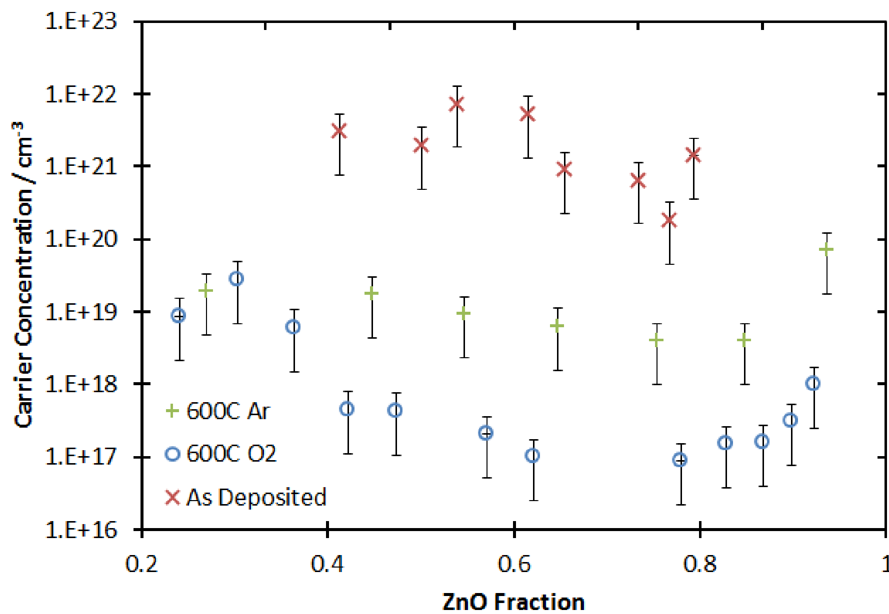

Figure 8.23: Charge carrier concentration of ZTO films sputtered under argon, for all annealing conditions.

two orders of magnitude in the case of argon annealing, and up to four orders of magnitude when annealed under oxygen. The lower carrier density after annealing in oxygen compared to argon supports the conclusion that the source of these carriers is largely oxygen deficiencies in the lattice.

The decrease in carrier density between the as-deposited and argon-annealed films might suggest that oxygen, independent of zinc or tin, was present in the as-deposited films, and this formed oxides under annealing, lowering the number of donor sites in the resulting film. However, the film was exposed to oxygen between sputtering and annealing as well, and some degree of atmospheric contamination may have served as an oxygen source during the annealing process.

8.3.5 Seebeck Coefficient of 100% Ar Samples

The Seebeck coefficients measured for the argon sputtering condition are shown in figure 8.24. The as-deposited film was measurable for this case, and contains the highest-magnitude Seebeck coefficients of -220 μV/K around $x \sim 0.4$, and -140 μV/K at $x \sim 0.9$. Similar to the film sputtered under 10% oxygen, the 600°C annealing condition appears to have significantly reduced electron-phonon coupling (due to the increase in order and reduction of charge carrier density), as the magnitude of the Seebeck coefficients in these films are seen to decrease by as much as an order of magnitude compared to their as-deposited counterparts.

8.3.6 Thermoelectric Figure of Merit

The final thermoelectric figures of merit for the argon-sputtered ZTO films are presented in table 8.3. ZT for these films is often noticeably lower than the oxygen-sputtered films.

Since it was not possible to accurately determine the thermal conductivity of the argon-annealed films for this sputtering condition, a calculation of ZT was not possible. The best possible candidate for the argon-annealed set was the film in the

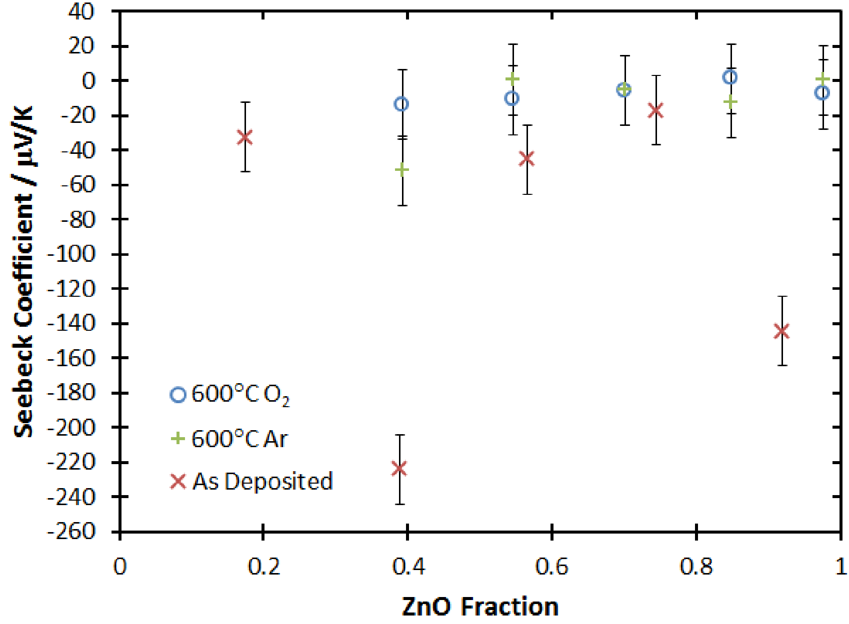

Figure 8.24: Seebeck coefficients for all ZTO films sputtered under argon.

Table 8.3: Calculated dimensionless figures of merit for ZTO films sputtered under argon, both as-deposited and annealed at 600°C under O_2. Calculation of ZT for the argon-annealed films was not possible due to the problems encountered determining thermal conductivity. Calculated for T = 300 K.

As dep.	x	0.17	0.39	0.56	0.74	0.92
	ZT	$(7\pm5)\text{x}10^{-8}$	$(2\pm1)\text{x}10^{-4}$	$(2\pm1)\text{x}10^{-5}$	$(1\pm1)\text{x}10^{-6}$	0.004 ± 0.002
600°C O_2	x	0.39	0.55	0.70	0.85	0.98
	ZT	$(2\pm2)\text{x}10^{-5}$	$(3\pm5)\text{x}10^{-6}$	$(0.3\pm1)\text{x}10^{-7}$	$(0.1\pm0.2)\text{x}10^{-8}$	$(0.5\pm1)\text{x}10^{-6}$

vicinity of x = 0.4, due to the high electrical conductivity of ~100 000 S/m and relatively high Seebeck coefficient of -50 μV/K. Taking a (very) approximate value for thermal conductivity of 10 W/m·K from figure 8.20, the calculated dimensionless figure of merit for this film is on the order of 0.01. While this would make this material among the best thermoelectric candidate of the ZTO films tested, further exploration of this material would require a significantly thicker film for 3ω measurements to

verify the thermal conductivity, or a direct measurement of a bulk sample.

8.4 Effective Lorenz Number

Table 8.4: Effective Lorenz numbers for ZTO films sputtered under argon, both as-deposited and annealed at 600°C under O_2. Calculation of L_{eff} for the argon-annealed films was not possible due to the problems encountered determining thermal conductivity. Calculated for $T = 300$ K.

As dep.	x	0.17	0.39	0.56	0.74	0.92
	$L_{eff}/\frac{W\Omega}{K^2}$	(2±0.5)x10^{-2}	(2±1)x10^{-4}	(1±0.7)x10^{-4}	(2±1)x10^{-4}	(5±3)x10^{-6}
600°C O_2	x	0.39	0.55	0.70	0.85	0.98
	$L_{eff}/\frac{W\Omega}{K^2}$	(1±0.7)x10^{-5}	(5±3)x10^{-5}	(1±0.5)x10^{-4}	(1±0.5)x10^{-4}	(1±0.7)x10^{-5}

Effective Lorenz numbers for ZTO films sputtered under argon are presented in table 8.4. Only the oxygen annealing condition is included, as difficulties with determining the thermal conductivity for the 600°C Ar annealing condition prevent calculation of L_{eff}. In general, all reported values are at least two orders of magnitude from the $\kappa \approx \kappa_e$ value for the Lorenz number of 2.45x10^{-8} W·Ω/K^2, indicating that electronic conduction of heat is dominated by phonon transport over the bulk of the stoichiometric range for the as-deposited and oxygen annealed samples.

8.5 Zinc Tin Oxide Thermoelectric Study Conclusions

The highly resistive, amorphous oxygen-sputtered films have low thermal conductivity, particularly below $x = 0.9$. Sputtering under argon produces a much more electrically conductive film, with high (10^{22} cm^{-3}) carrier concentration. In this argon-sputtered film, the peak in thermal conductivity near $x = 0.4$ closely mirrors a similar peak in electrical conductivity at the same stoichiometry. Annealing under oxygen produces a three order of magnitude drop in carrier concentration, and in

the annealed film the peak in thermal conductivity is no longer visible. This, combined with the lack of structure in XRD measurements, supports the idea that heat transport is electron-dominated, and that charge carriers in the as-deposited film are largely due to oxygen vacancies.

Annealing produces an increase in crystallinity, notably in the Zn_2SnO_4 phase around $x = 0.7$, and the SnO_2 phase below $x = 0.5$. In areas of increased crystallinity, thermal conductivity is seen to rise compared to the as-deposited films, and phonon transport of heat appears to dominate.

While an increase in ZnO and SnO_2 crystallinity appears to increase both thermal conductivity and electrical conductivity, the formation of a Zn_2SnO_4 phase results in a significant trough in electrical conductivity, as well as a narrow peak in thermal conductivity in non oxygen-deficient films.

In the as-deposited argon-sputtered film, the variation in electrical conductivity appears to be largely modulated by changes in mobility near the tin-rich and zinc-rich ends of the range, while carrier mobility is relatively constant near the middle. In all other films however, electrical conductivity appears to be modulated primarily by carrier concentration, save for the abrupt drop in mobility around the formation of Zn_2SnO_4 phases.

Up to an order of magnitude decrease in the magnitude of Seebeck coefficients for annealed films relative to their as-deposited counterparts is observed, largely due to a multiple order of magnitude decrease in carrier concentration. Relatively low-magnitude ($\sim$ -20 μV/K) Seebeck coefficients result in relatively low dimensionless figures of merit for annealed films, while low electrical conductivity limits the as-deposited films.

Chapter 9

Zinc Indium Oxide Thermoelectric Study

As with the zinc tin oxide thermoelectric study, two zinc indium oxide sputtering conditions were examined. In the first, the same sputter gas conditions as the ZIO transistor study were used, with gas concentrations at 80% Ar and 20% O_2. The second condition used 100% argon.

9.1 80% Ar, 20% O_2 Sputtering Condition

9.1.1 Fabrication of 80% Ar, 20% O_2 Samples

Zinc indium oxide films were sputtered onto 100 mm, heavily doped ($< 0.005\ \Omega\cdot$cm) <100> silicon wafers. As with the partial oxygen ZTO study, these wafers had only a native oxide, and therefore required that a 200 nm Al_2O_3 electrically insulating film be applied via e-beam, with rotation, prior to sputtering.

The ZnO and In_2O_3 targets were the same 50 mm targets used in the ZIO TFT study in chapter 6. The ZnO target was sputtered at a power of 40 W, while the In_2O_3 target was sputtered at 90 W. In contrast to the samples presented in the TFT study, the ZIO samples sputtered here were masked to create a film varying nominally from 100% In_2O_3 at the inner edge to 100% ZnO at the outer edge, using the deposition rates determined for each target prior to the TFT study. Sputtering occurred at a pressure of 5 mTorr, consisting of 80% argon and 20% oxygen. The wafers were patterned using the stencil mask design in figure 3.1. Silicon strips, glass strips, and mass disks were included on the table with the wafers.

Due to the lower sputtering rate of the In_2O_3 target, sputtering time was approximately 16 hours. This time also helped to ensure that films were thick enough

that the corrections done to the microprobe data in the TFT experiment were not necessary for these samples.

Two wafers were annealed at 300°C for 30 minutes while a third was left as-deposited. One wafer was annealed under oxygen, and the other was annealed under argon. After annealing, the van der Pauw structures of all three wafers were covered with aluminum foil and 400 nm of Al_2O_3 was e-beam deposited at a rate of approximately 0.2 nm/s, with the wafers rotating. The wafers were then patterned for lift-off using the mask design in figure 5.3, followed by a de-scum step.

Nickel was e-beam deposited at a rate of 0.1 nm/s to a total thickness of 320 nm. The wafers were allowed to cool in vacuum, and were then exposed to atmosphere for approximately 16 hours before lift-off to enhance adhesion of the metal to the sample.

9.1.2 Physical Characterization of 80% Ar, 20% O_2 Samples

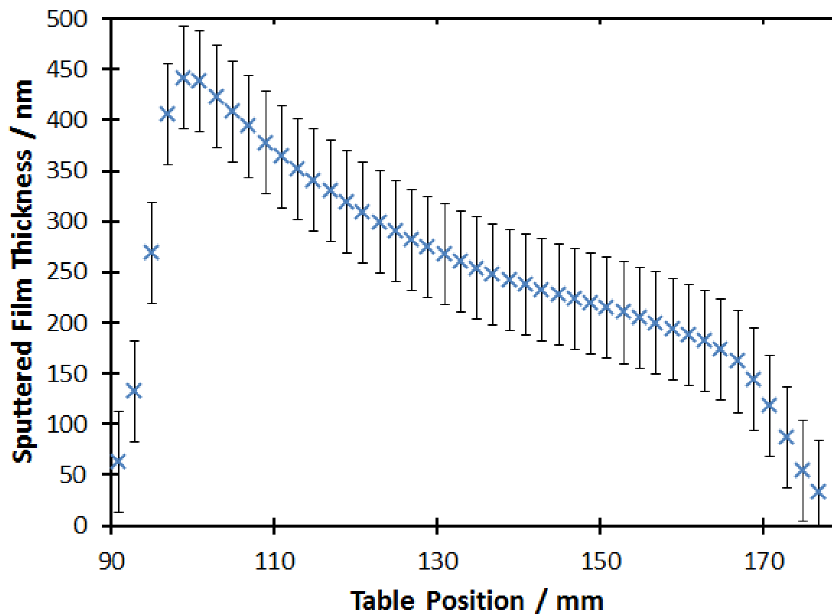

Figure 9.1: Measured thickness of ZIO films sputtered under 20% oxygen as a function of radial position on the sputtering table. Zinc oxide content increases with radial position.

Ellipsometry and profilometry measurements revealed the sputtered film to range

from 450 nm thick at the inner edge of the sputtering track, to 150 nm at the outer edge (figure 9.1). This is approximately four times the thickness of the films used in the ZIO TFT experiment and is consistent with the approximately four-fold increase in sputtering time used here.

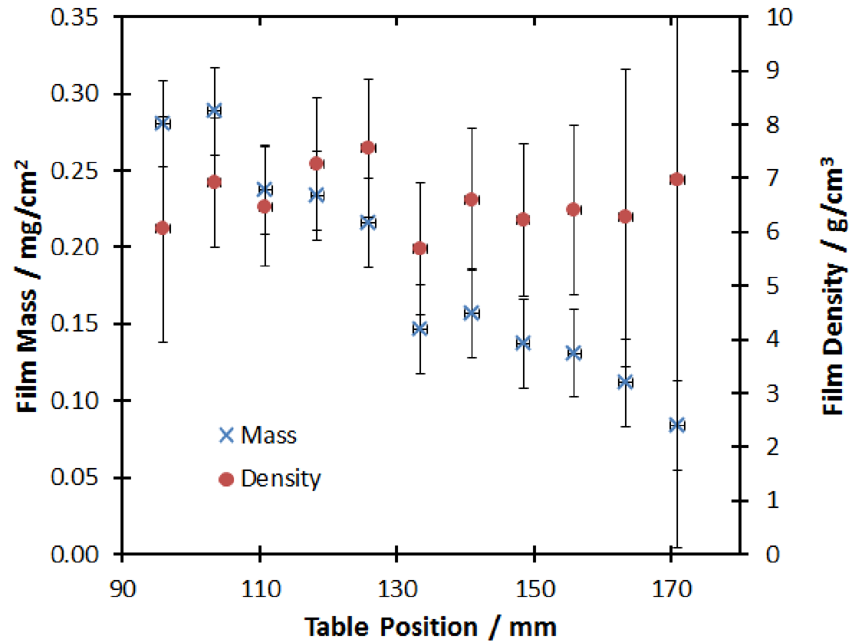

Figure 9.2: Film mass and density for ZIO films sputtered under 20% oxygen.

The mass per unit area of the films (figure 9.2) varies significantly across the sputtering track. However, mass as a function of table radial position mirrors film thickness with radial position. As a result, the calculated density of the films is approximately equal for all stoichiometric positions, at around 7 ± 1 g/cm^3. This value is consistent with the bulk density of In_2O_3 of around 7.2 g/cm^3[100], but is approximately 25% higher than the bulk density of ZnO, even at the outermost edge of the track. This is in contrast to the ZTO films in which the sputtering film bulk density approached the ZnO bulk value near the edge, and suggests that the presence of In_2O_3 in the zinc-rich end of the range results in a different film structure than the same ratio of ZnO and SnO_2.

Microprobe measurements of film stoichiometry (figure 9.3) revealed the films to

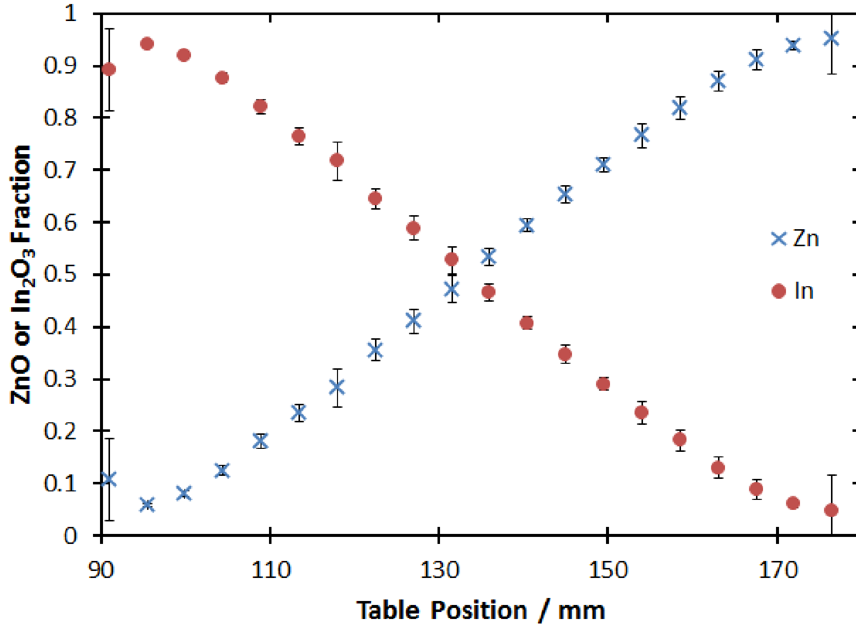

Figure 9.3: Normalized atomic fractions of Zn and In as a function of radial position on the sputtering table for the 80% argon, 20% oxygen sputtering run.

vary from approximately 5% ZnO at the inner edge, to 95% ZnO at the outer edge. WDS mode measurements revealed a negligible silicon signal during measurements, indicating that the film was sufficiently thick to remove the need for the corrections using Casino that were necessary in the TFT experiment.

9.1.3 Thermal Conductivity of 80% Ar, 20% O_2 Samples

The thermal conductivity of the as-deposited samples (figure 9.4) shows a broad minimum in thermal conductivity of 3 W/m·K for $0.3 < x < 0.5$, and rises with ZnO content toward a peak of ∼6 W/m·K near $x = 1$. The small signal (i.e. small difference in temperature amplitude between film and no-film heaters) combined with the relatively thin film in this region results in some increase scatter toward the zinc edge of range.

X-ray diffraction results (figures 9.5) show two main areas of structure, one near the pure indium oxide extreme and the other near the zinc oxide extreme. Representative plots for these regions are shown in figure 9.6. For $x < 0.1$, a phase of In_2O_3 is

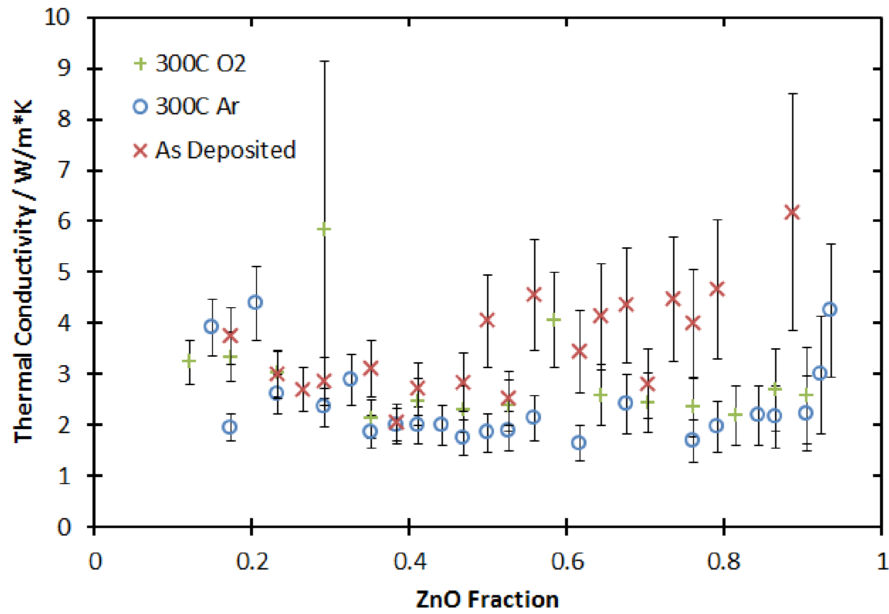

Figure 9.4: Thermal conductivity at room temperature of ZIO films sputtered in 20% oxygen as a function of zinc oxide fraction.

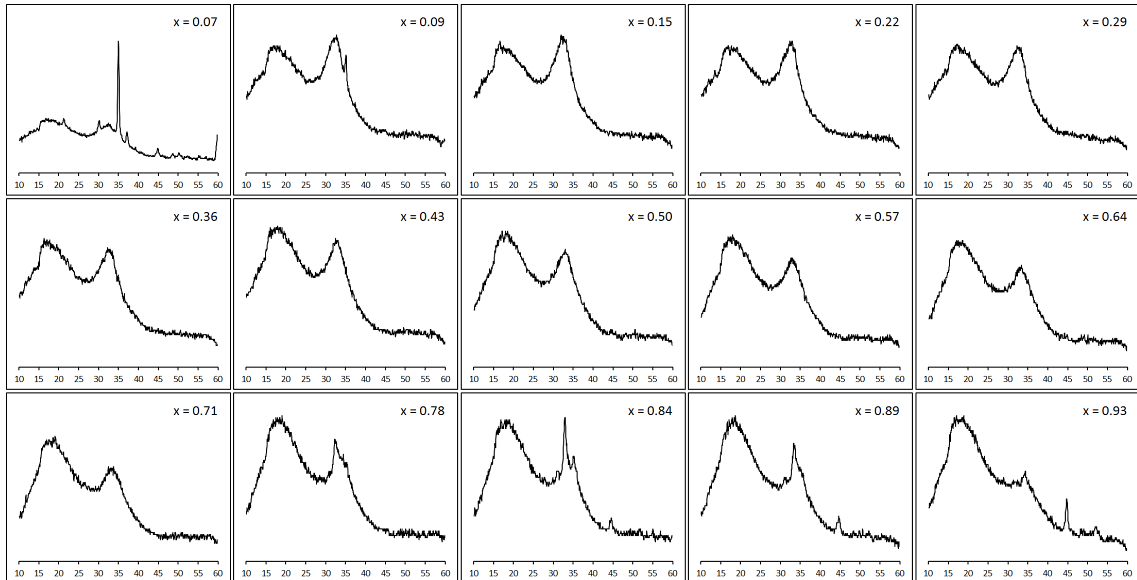

Figure 9.5: XRD results for as-deposited ZIO films deposited in 20% oxygen.

visible. The peaks for this phase differ from what would be expected from a powder diffraction sample[95, 96, 97, 98]; in a powder sample the (222) peak should be dominant, while in these data the (400) peak is by far the most pronounced, indicating a

potential preferred orientation for the phase. For $x \geq 0.8$ a ZnO phase is visible, the peaks for which are labeled in figure 9.6. This ZnO phase exhibits the same apparent preferred orientation as the phases observed in the ZTO films, with the (002) peak stronger than any other visible peaks.

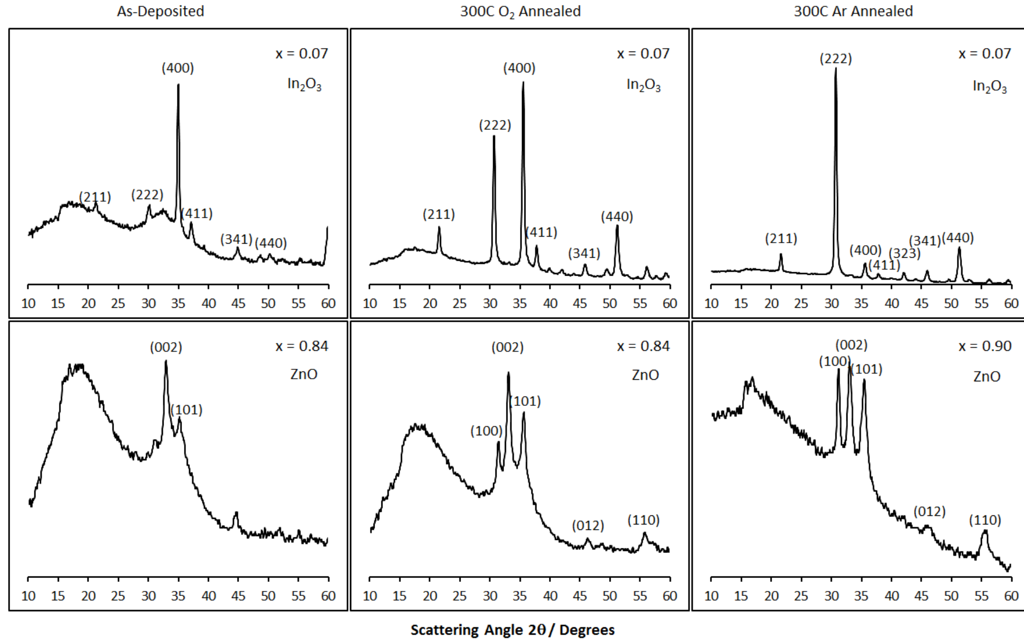

Figure 9.6: XRD for selected stoichiometries of ZIO sputtered under 20% oxygen for all annealing conditions.

The thermal conductivity of the film after annealing at 300°C under oxygen reveals that the rise in thermal conductivity with zinc content for $x > 0.5$ is now absent. This could indicate that the thermal conductivity in this region of the as-deposited films was an electronic contribution, with a carrier density due largely to oxygen vacancies in the sputtered film. Across most of the range the thermal conductivity of the film is confined between 2-3 W/m·K, rising slightly above 3 W/m·K near the indium oxide edge.

XRD of the film shows a significant increase in crystallinity for $x < 0.2$ compared to the as-deposited film (figure 9.7). While the (222) peak of this annealed phase is more prominent, potentially indicating less global orientation to the phase, it is

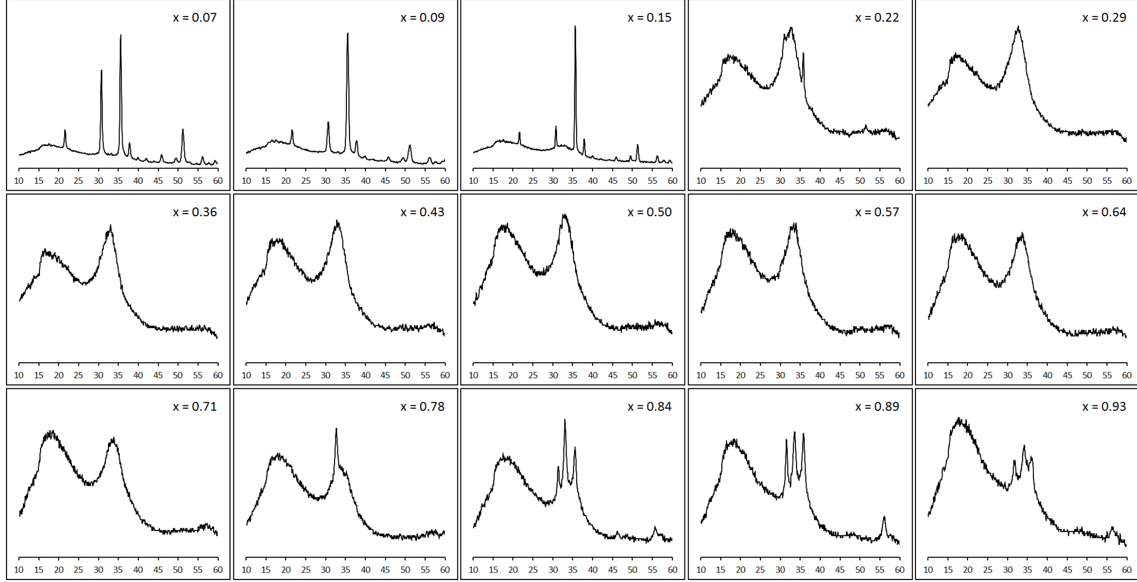

Figure 9.7: XRD results for 300°C oxygen-annealed ZIO films deposited in 20% oxygen.

still far lower than the 4:1, (222):(400) peak intensity ratio one would expect from a powder sample[95, 96, 97, 98]. Additionally, an increase in structure for $x > 0.8$ is visible.

The thermal conductivity of the films annealed at 300°C under argon is largely similar to the oxygen-annealed film, being constant across most of the range. However it appears to be slightly lower, on average, than the oxygen-annealed films. Again there appears to be a small increase in thermal conductivity below approximately 25% ZnO. It should be noted that both annealing under oxygen and under argon produced the same reduction in thermal conductivity in the ZnO-rich end of the range.

The XRD data for the argon annealing condition indicate both the In_2O_3 and ZnO phases observed in the as-deposited and oxygen annealing conditions, with some distinct differences. The In_2O_3 phase extends to much higher ZnO concentrations than in either of the other conditions, with peaks visible as high as $x = 0.38$. In addition, the (400) peak dominance seen in the other films is only visible here for $x \geq 0.2$, while films below this value of x produce XRD plots similar to what one would expect of a randomly oriented powder sample[95, 96, 97, 98] (figure 9.6). The

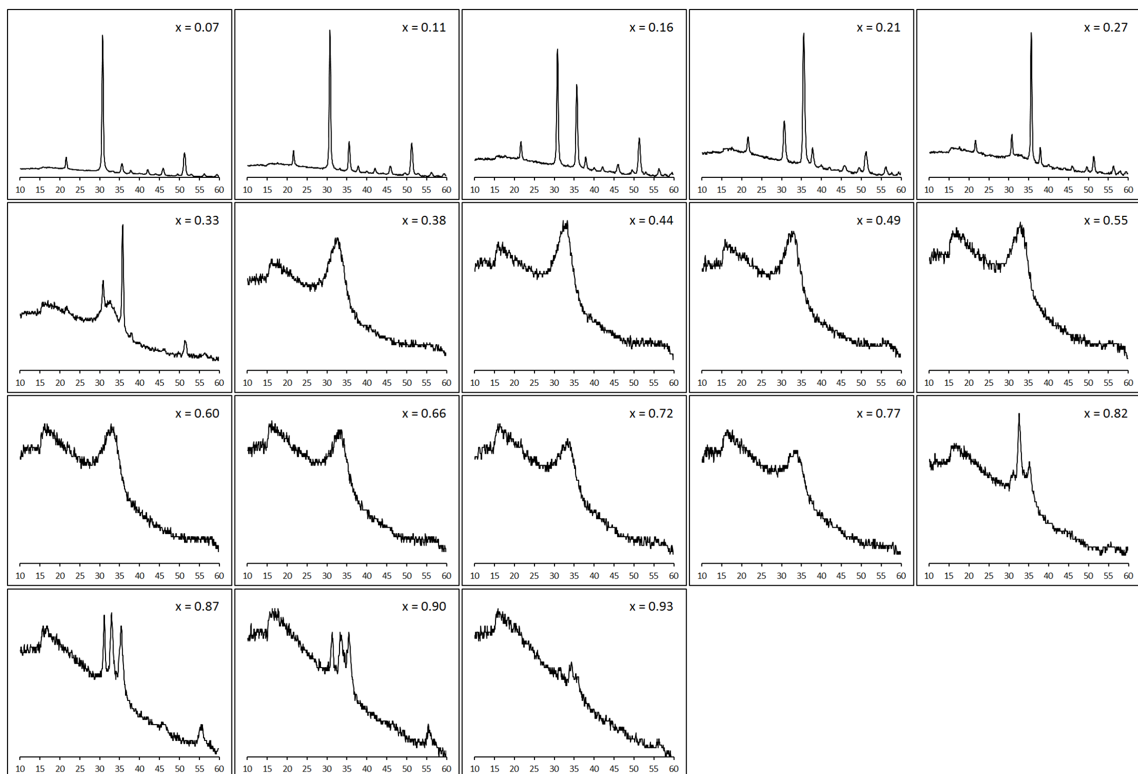

Figure 9.8: XRD results for ZIO films deposited in 20% oxygen and annealed at 300°C under argon.

ZnO peaks also no longer have the dominant (002) peak seen in the other annealing conditions, as well as all ZTO data, and instead shows peaks that are approximately equal in intensity.

In all three annealing conditions, a rise in thermal conductivity is visible toward the indium oxide extremes of the stoichiometric range, and these appear to correspond to increases in crystallinity, indicating that phonon transport of heat is primary in these films. In the case of the as-deposited film near the zinc-oxide extreme, there is an increase in thermal conductivity that may correspond to a small increase in electrical conductivity.

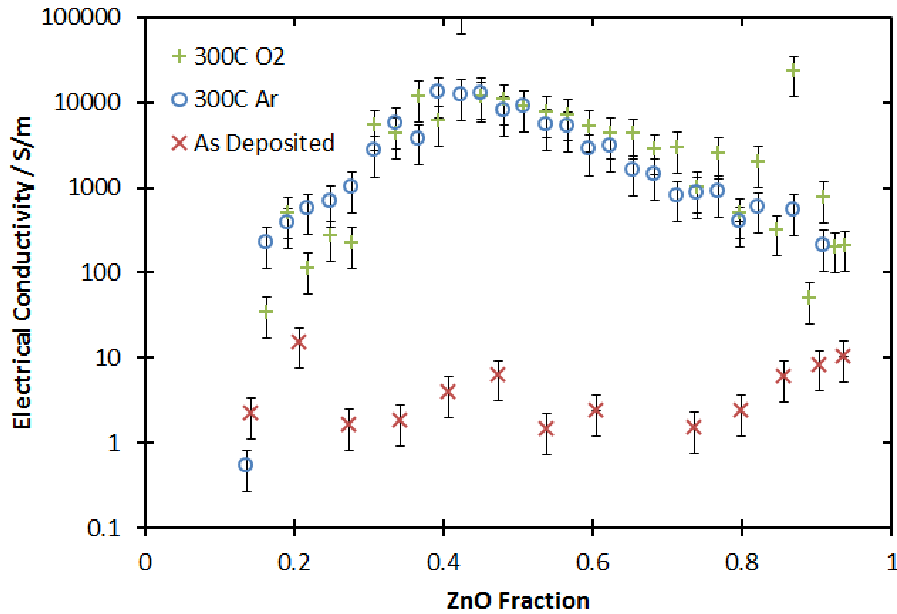

Figure 9.9: Electrical conductivity of ZIO films sputtered in 20% oxygen as a function of zinc oxide fraction.

9.1.4 Electrical Conductivity of 80% Ar, 20% O_2 Samples

The electrical conductivity of the as-deposited samples (figure 9.9) was low, ranging from 1-10 S/m. This result was expected, and is consistent with the results found for the ZIO TFT study in chapter 6. However, the TFT study covered only half of the stoichiometric range, from 50% to 100% ZnO, for films sputtered under 20% O_2. The data in figure 9.9 show that this low electrical conductivity continues across the entire range.

The low conductivity of films sputtered under 20% oxygen contrasts with the high conductivity of an initial set of films sputtered during the TFT study under 10% oxygen. This contrast is consistent with the sensitivity of electrical conductivity to oxygen during sputtering reported in other studies[65].

In any case, electrical conductivity rises by an order of magnitude over $0.7 < x < 0.95$, and this appears to correspond to the increase in thermal conductivity over the same range. While there is also an increase in crystallinity in this range, that same

increase exists in the annealed films, without a corresponding rise in electrical conductivity. This may indicate that thermal transport may be influenced by conduction electrons in this region.

Annealing at 300°C under oxygen dramatically increases the electrical conductivity of the films, by as much as four orders of magnitude (figure 9.9). A broad peak in conductivity is seen across the range, with a maximum conductivity of 10^4 S/m at a zinc oxide fraction of 0.4. For ZnO concentrations below this the electrical conductivity drops rapidly, to below 100 S/m at a zinc oxide fraction of 0.2. Above 0.4, the conductivity of the films decreases approximately linearly with increasing zinc oxide fraction, reaching ∼100 S/m at the zinc-rich end of the stoichiometric range.

In figure 9.9 the films annealed under argon exhibit a very similar relationship between stoichiometry and electrical conductivity as their oxygen-annealed counterparts. However, films with zinc oxide fractions below 0.4 appear to be more conductive, falling from a similar peak of 10^4 S/m to slightly above 100 S/m for zinc oxide fractions below 0.2.

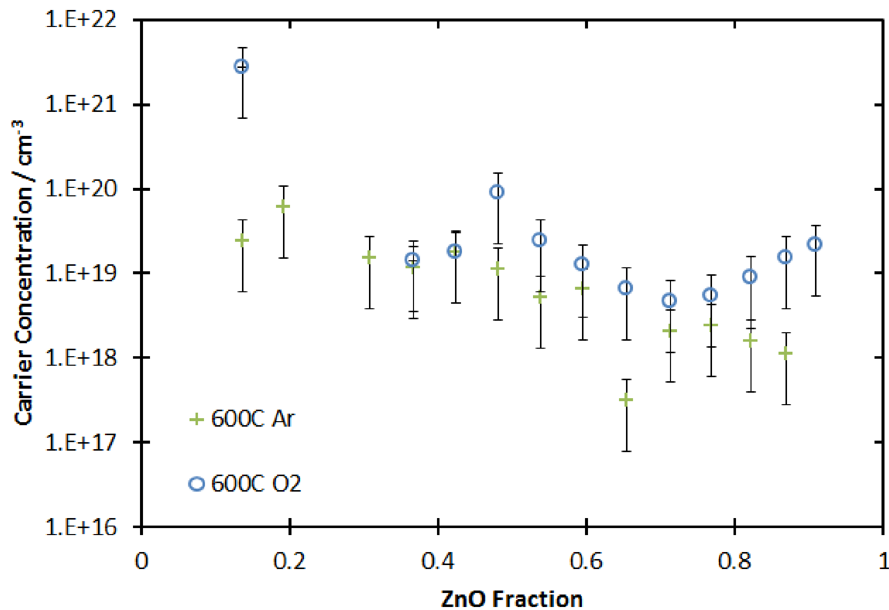

Figure 9.10: Carrier density for ZIO films sputtered under 20% oxygen.

The relatively small difference in thermal conductivity between the oxygen and argon-annealed films, and their large increase relative to the as-deposited film, suggests that an increase in crystal structure resulted in an increase in carrier mobility. Unfortunately, the low conductivity of the as-deposited films made it impossible to conduct an accurate Hall effect measurement, and charge carrier density for this film could not be determined. The charge carrier density of the other two films (figure 9.10) indicate that a decrease in mobility with increasing In_2O_3 content likely limits conductivity for $x < 0.4$, since carrier concentration does not decrease in this region. Above this mixture ratio mobility is relatively constant and electrical conductivity changes with carrier density as a function of stoichiometry.

9.1.5 Seebeck Coefficient of 80% Ar, 20% O_2 Samples

The Seebeck coefficients of all annealing conditions are shown as a function of stoichiometry in figure 9.11. In contrast to the zinc tin oxide films, the as-deposited film Seebeck coefficients are approximately zero across the entire stoichiometric range.

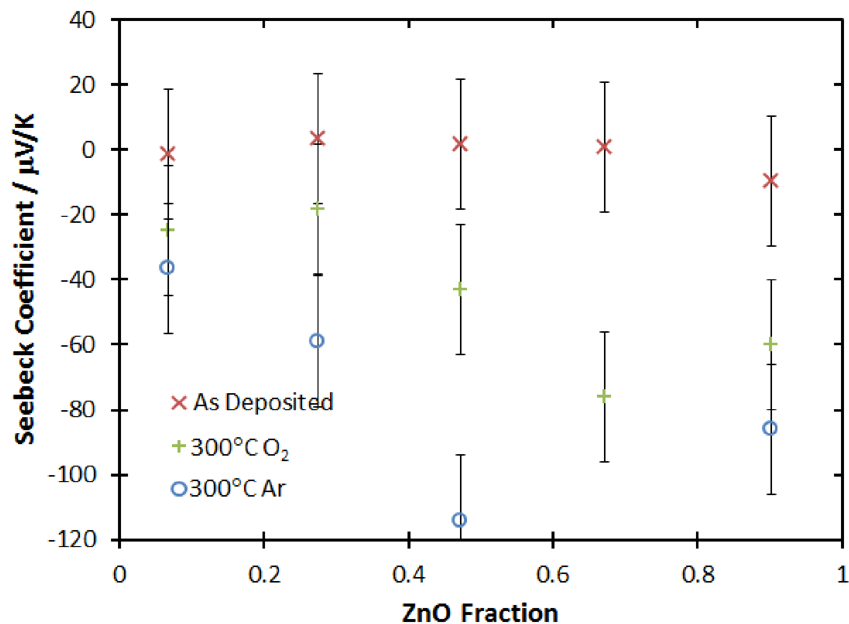

Figure 9.11: XRD results for all ZIO films sputtered under 20% oxygen.

Annealing under both argon and oxygen produces a broad peak in Seebeck coefficient magnitude, with a maximum around $x = 0.7$. As expected from the n-type nature of the TFT devices made using the same films, the Seebeck coefficients are negative. The oxygen annealing condition produces a peak that is more than double in magnitude with respect to the argon-annealed film. Seebeck coefficients for the oxygen condition are also larger in magnitude than their argon-annealed counterparts for all other measured stoichiometries. The higher carrier concentration in the oxygen films relative to the argon may explain this difference, if electron-phonon coupling is assumed to be similar.

9.1.6 Thermoelectric Figure of Merit

Table 9.1: Calculated dimensionless figures of merit for ZIO films sputtered under oxygen for $T = 300$ K.

As dep.	x	0.27	0.47	0.67	0.90
	ZT	$(0.2\pm0.1)\text{x}10^{-8}$	$(0.2\pm0.2)\text{x}10^{-8}$	$(0.1\pm0.3)\text{x}10^{-10}$	$(4\pm8)\text{x}10^{-8}$
300°C O_2	x	0.27	0.47	0.67	0.90
	ZT	$(8\pm5)\text{x}10^{-5}$	0.02 ± 0.01	0.01 ± 0.005	$(6\pm4)\text{x}10^{-4}$
300°C Ar	x	0.27	0.47	0.67	0.90
	ZT	$(4\pm5)\text{x}10^{-5}$	0.003 ± 0.001	0.001 ± 0.0005	$(1\pm0.7)\text{x}10^{-4}$

The dimensionless thermoelectric figures of merit were calculated at $T = 300$ K and are shown in table 9.1. Due to the high magnitude Seebeck coefficients found in both annealed films for $x = 0.5$ and 0.7, and combined with relatively high electrical conductivity and low thermal conductivity, the 300°C annealed films both produced relatively high figures of merit. The oxygen condition in particular produces interesting values, as high as 0.02 for $x = 0.47$.

The samples annealed at 300°C under oxygen yield the highest values for ZT, on the order of 0.01 for $x = 0.47$ and $x = 0.67$. These are consistent with the finding of Amani et. al.[39] in which ZIO compounds around this stoichiometric range are found to give ZT between 0.01 and 0.04 at 300°C. However, the stoichiometries measured here that lie outside of this range have far lower ZT.

A common theme in the ZTO films was that high electrical conductivity came at the cost of high thermal conductivity. This is particularly noticeable in the argon-sputtered, argon-annealed films. The annealed ZIO films, however, exhibit the same order of electrical conductivity (~10^4 S/m) at their peaks, while maintaining comparatively low (<3 W/m·K) thermal conductivity, resulting in a number of films with ZT on the order of 10^{-2}. While argon annealing resulted in a somewhat lower ZT than oxygen annealing, both of the annealed films produce significantly higher ZT than the ZTO films.

9.2 Effective Lorenz Number

Table 9.2: Calculated effective Lorenz numbers for ZIO films sputtered under oxygen for $T = 300$ K.

As dep.	x	0.27	0.47	0.67	0.90
	$L_{eff}/\frac{W\Omega}{K^2}$	(6±3)x10^{-3}	(2±1)x10^{-3}	(6±3)x10^{-3}	(3±1)x10^{-3}
300°C O_2	x	0.27	0.47	0.67	0.90
	$L_{eff}/\frac{W\Omega}{K^2}$	(5±2)x10^{-5}	(7±3)x10^{-7}	(3±2)x10^{-6}	(1±0.6)x10^{-5}
300°C Ar	x	0.27	0.47	0.67	0.90
	$L_{eff}/\frac{W\Omega}{K^2}$	(5±0.7)x10^{-5}	(7±4)x10^{-7}	(6±3)x10^{-6}	(4±2)x10^{-5}

Effective Lorenz numbers for selected stoichiometric ratios are presented in table 9.2. Due to the low carrier concentration, L_{eff} for the as-deposited samples are

significantly greater than the 'ideal' Lorenz number for a metal of 2.45 x 10^{-8} W·Ω/K^2, and are generally high by ~5 orders of magnitude, indicating phonon-dominated thermal transport.

While the two annealing conditions also produce Lorenz numbers that are significantly greater than this ideal value, the increased carrier density and electrical conductivity result in values that are closer in magnitude to the ideal. However, only the $x = 0.47$ stoichiometries approach within an order of magnitude of L, corresponding to the peak in electrical conductivity for these two conditions, seen in figure 9.9.

9.3 100% Ar Sputtering Condition

9.3.1 Fabrication of 100% Ar Samples

Zinc indium oxide films sputtered onto 100 mm diameter, heavily doped (< 0.005 Ω·cm) <100> silicon wafers. These wafers had a thermally grown, 300 nm silicon dioxide layer. This layer made the deposition of an Al_2O_3 electrically insulating film prior to sputtering unnecessary.

The zinc oxide target used was the same 50 mm target used in all other sputtering runs. However, a new indium oxide target, acquired from Kurt Lesker and consisting of 99.99% In_2O_3, was used for this experiment, as the previous target sputtered through to the copper mounting plate on a prior run, contaminating the sputtered films. The ZnO and In_2O_3 targets were sputtered at 40 W and 90 W, respectively, and were masked to create a film that would nominally vary from 100% In_2O_3 at the inner edge of the track, to 100% ZnO at the outer edge. Sputtering took place under 5 mTorr of argon. Mass disks, as well as silicon and glass strips were included on the sputtering table. Wafers were patterned using stainless steel stencil masks of the pattern in figure 3.1.

The sputtering time was chosen to match that of 80% Ar, 20% O_2 ZIO samples, at approximately 16 hours. It was expected that sputtering under argon would result

in an increase in sputtering rate, so this time was picked to again ensure that the resulting films would be thick enough that no correction of the microprobe data would be required.

Two wafers were annealed at 300°C for 30 minutes, while a third was left as-deposited. One wafer was annealed under oxygen, while the other was annealed under argon. All three wafers had a 400 nm Al_2O_3 layer e-beam deposited at 0.2 nm/s with the wafer rotating. The wafers were patterned for lift-off using the design in figure 5.3 with a de-scum step. Aluminum was e-beam deposited at ~0.1 nm/s to a total thickness of 150 nm. Because aluminum was used, it was not necessary to cool the wafers in vacuum after metal deposition, nor was a long atmospheric exposure required to promote metal adhesion.

9.3.2 Physical Characterization of 100% Ar Samples

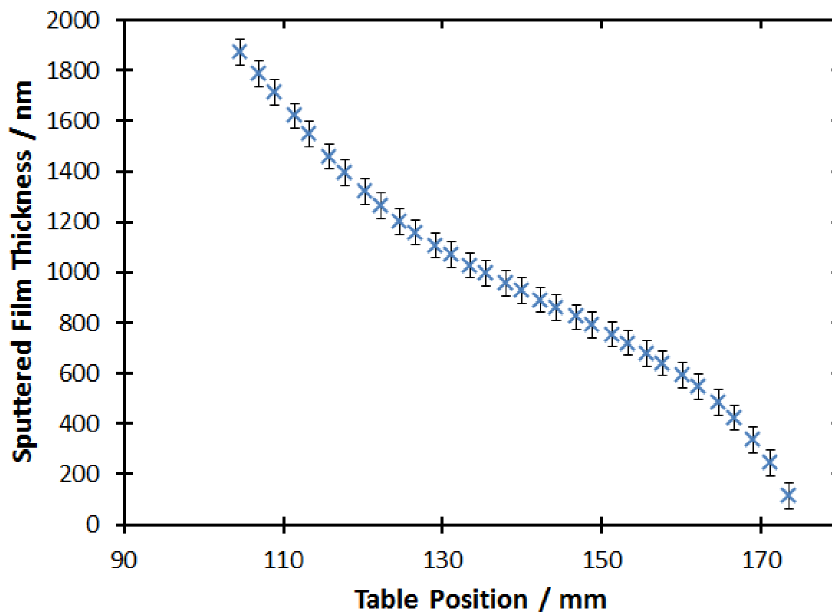

Figure 9.12: Measured thickness of ZIO films sputtered under argon as a function of radial position on the sputtering table. Zinc oxide content increases with radial position.

Thickness as a function of table position is presented in figure 9.12. It was found

that the sputtering rate for the indium oxide target at 90 W and a pressure of 5 mTorr was much higher under 100% argon than it was under 80% argon and 20% oxygen. The total thickness of the film for the same target powers and sputtering time was approximately 2000 nm at the inner, indium oxide edge of the track, to 200 nm at the outer, zinc oxide edge. The film at the inner edge is much thicker than any other films measured in these experiments. However, while thick films can cause problems in thin film transistors, namely in the form of increased off currents, it was not expected to pose a problem for the thermal conductivity, electrical conductivity and Seebeck measurements for this phase of the project.

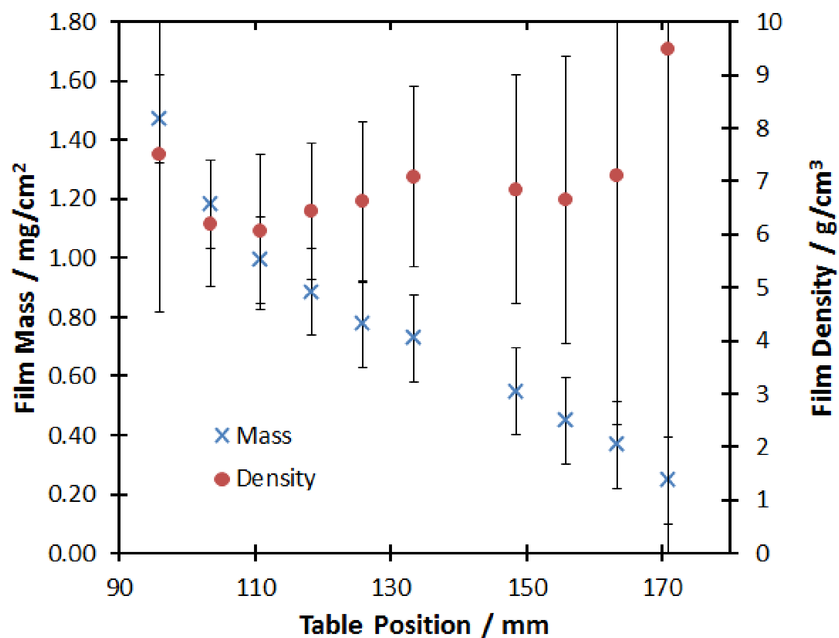

Figure 9.13: Film mass and density for ZIO films sputtered under argon.

The mass of this film was found to change with table position in a manner similar to the film thickness (figure 9.13). However, the density of the film was again found to be largely constant across the sputtering track, and has a similar value (6-7 g/cm^3) as the films sputtered under partial oxygen. Therefore, the increased thickness indicates a greater amount of material being deposited, as opposed to a more porous structure, when compared to films produced in the partial oxygen ZIO sputtering condition.

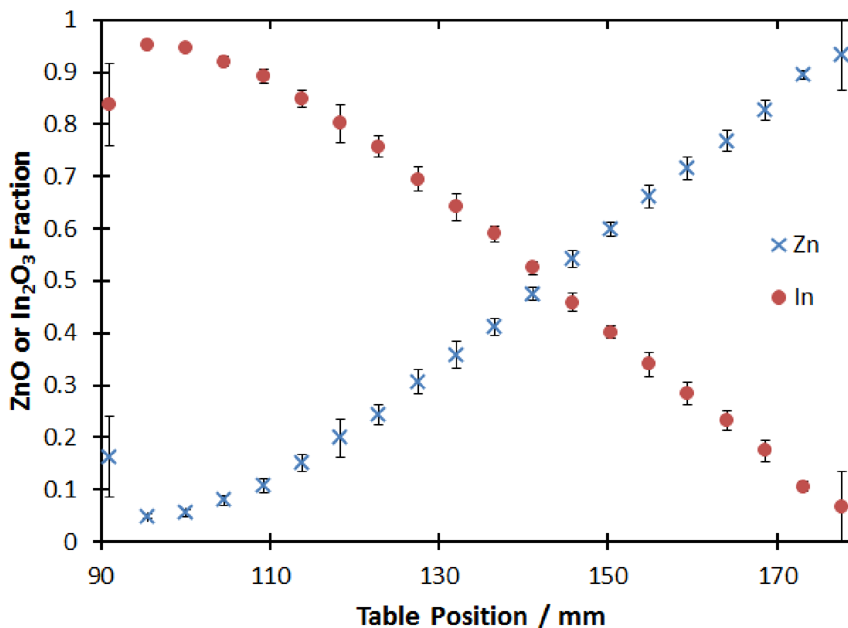

Figure 9.14: Normalized atomic fractions of Zn and In as a function of radial position on the sputtering table for the 100% argon sputtering run.

Due to the increased indium oxide deposition rate, the stoichiometry of the films as a function of table position (figure 9.14) reaches a 50/50 mixture closer to the outside edge of the track. However, the total range is similar to the partial oxygen run, varying from 97% In_2O_3 at the inner edge of the track to 95% ZnO at the outer edge. As might be expected with a film of this thickness, negligible silicon signal from the substrate was detected during WDS mode microprobe measurements.

9.3.3 Thermal Conductivity of 100% Ar Samples

The heaters used to characterize the as-deposited films had relatively low yields and high scatter, possibly due to higher-than-normal roughness on the sputtered film owing to the increased sputtering rate. The data (figure 9.15) show the thermal conductivity of the film varying from approximately 4-5 W/m·K at the indium-rich end, to 2-3 W/m·K at the zinc rich end.

The film near $x = 0$ was found to be significantly more crystalline than the as-deposited film in the 20% oxygen condition, with a clear In_2O_3 phase visible for x

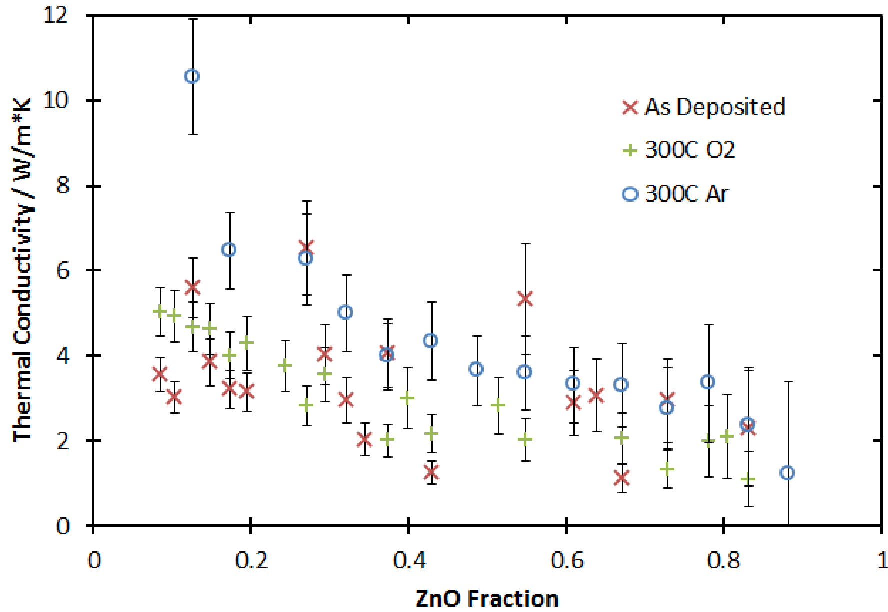

Figure 9.15: Thermal conductivity at room temperature of ZIO films sputtered in argon as a function of zinc oxide fraction.

$\leq$ 0.13 (figure 9.16). However, unlike the oxygen-sputtered as-deposited film, this phase has relative peak intensities that are close to those one would expected from a randomly oriented polycrystalline structure, and the preferred orientation is absent at $x = 0.06$ (figure 9.17). Moving away from the $x = 0$ edge, the (222) peak becomes more intense relative to the other peaks. Interestingly, this effect is different from what was observed in the oxygen-sputtered samples, where the (400) peak intensity grew with increasing ZnO content, indicating a different preferred direction for the crystal structure when sputtered under argon than when sputtered under oxygen. The apparent decrease in thermal conductivity with ZnO content appears to mirror the decrease in organzation of the film. Near the ZnO end of the range a set of ZnO peaks are visible, but this signal is very weak, particularly considering the thickness of the film in this area.

The thermal conductivity of the films annealed at 300°C under oxygen are presented in figure 9.15. The same trend of increasing thermal conductivity with increasing In_2O_3 content is visible. Thermal conductivity decreases approximately linearly

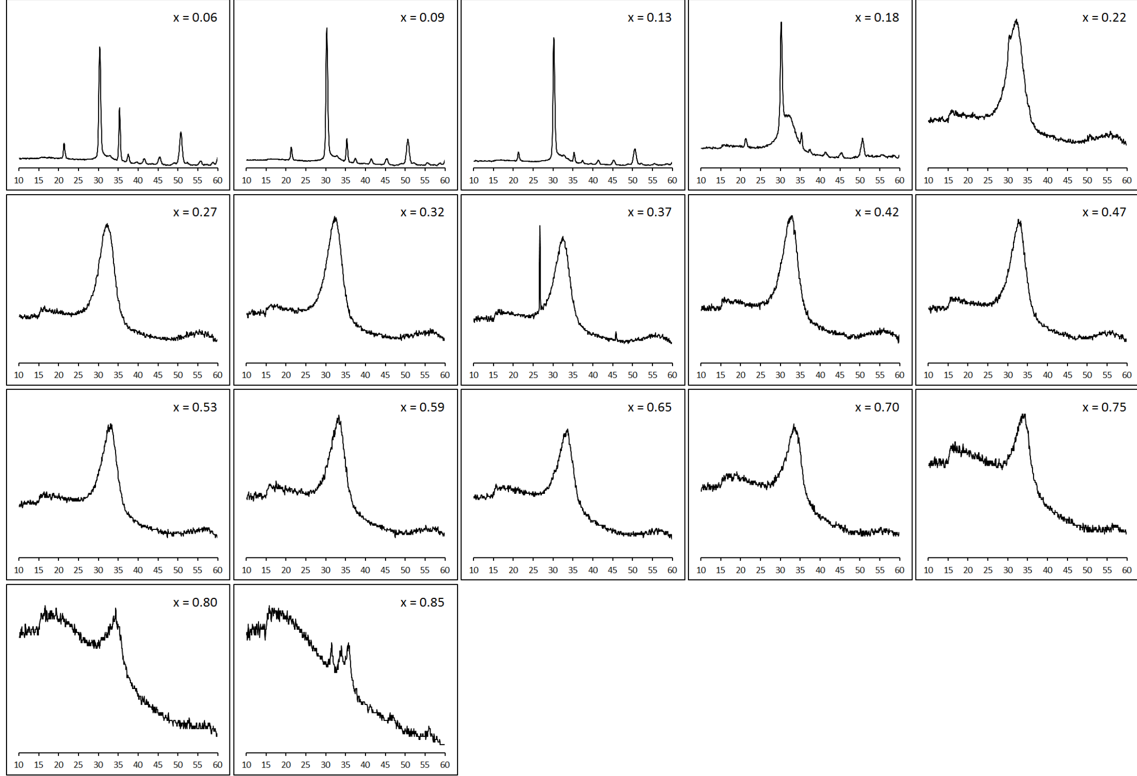

Figure 9.16: XRD results for as-deposited ZIO films deposited in argon.

from 5 to 2 W/m·K over $0.1 < x < 0.6$, and decreases slightly more to just over 1 W/m·K above $x = 0.8$. If one compares the XRD results for this film (figure 9.18) to those for the equivalent oxygen-sputtered film (figure 9.7) both show a clear In_2O_3 phase up to $x \approx 0.15$, but the argon-sputtered film is significantly more conductive in this region. This may be due to an increase in the electronic contribution to thermal conductivity due to oxygen vacancies in the argon-sputtered film.

Focusing on the peaks themselves (figure 9.17) the $x = 0.06$ phase is very similar to the as-deposited film, though with enhanced peak intensity. This increase in intensity is not apparent near the ZnO edge, where the $x = 0.85$ is very similar to its as-deposited counterpart. An interesting difference exists between annealed and as-deposited $x = 0.13$ plots. While the relative peak intensities are similar, there is a clear 'doubling' of the (222) peak after annealing, suggesting a superposition of two distinct In_2O_3 phases or twinning. The weaker, left-hand phase visible in figure 9.17

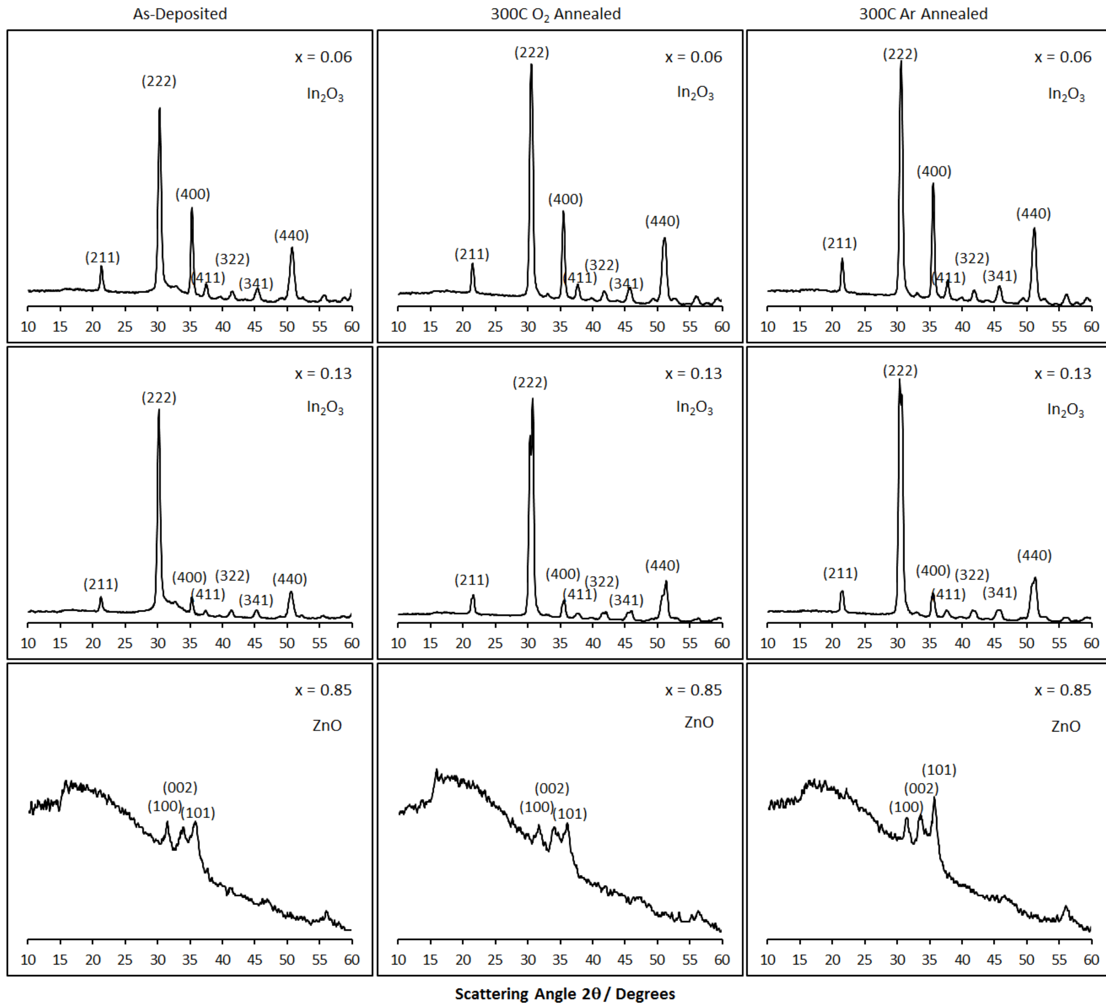

Figure 9.17: XRD for selected values of x for argon-sputtered ZIO films.

appears to be a slight distortion of the crystal structure, while the right-hand peaks are consistent with reference powder-diffraction data[95, 96, 97, 98].

Thermal conductivity results for the films annealed under argon (figure 9.15) exhibit a trend similar to the oxygen-annealed samples. However, the thermal conductivities are broadly higher; around $x = 0.8$ they are measured to be around 3 W/m·K and increase approximately linearly to 4 W/m·K around $x = 0.4$. Below this zinc oxide fraction thermal conductivity rises rapidly to over 6 W/m·K around $x = 0.2$, and over 10 W/m·K at $x = 0.13$.

XRD reveals the argon-annealed films to be very similar to the oxygen-annealing

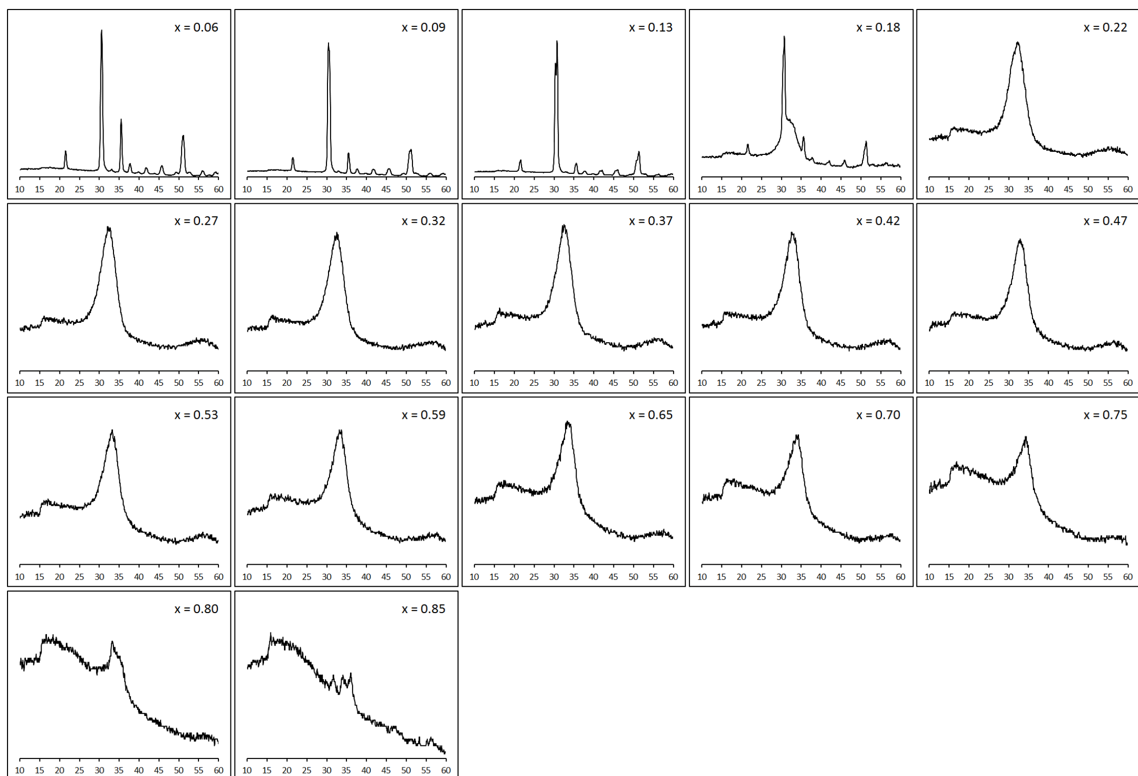

Figure 9.18: XRD results for ZIO films deposited in argon and annealed at 300°C under oxygen.

condition (figure 9.19), though In_2O_3 structure is now visible in the $x = 0.18$ plot. The same change in relative peak intensity with increasing ZnO content is visible, along with the 'doubling' of peaks around the $x = 0.18$ result (figure 9.17). The ZnO end of the range again seems relatively unaffected by annealing. While there may be a slightly larger amount of organization in the argon-annealed films (namely in the form of the $x = 0.18$ structure) the increase across the range relative to the oxygen annealing condition again suggests a significant electronic contribution to thermal conductivity in these films from increased density of charge carriers due to oxygen vacancies.

In all three cases, the zinc oxide-rich region of films exhibits a decrease in thermal conductivity with annealing, matching the results from the 20% oxygen sputtering condition. However, annealing greatly increase the thermal conductivity of the indium

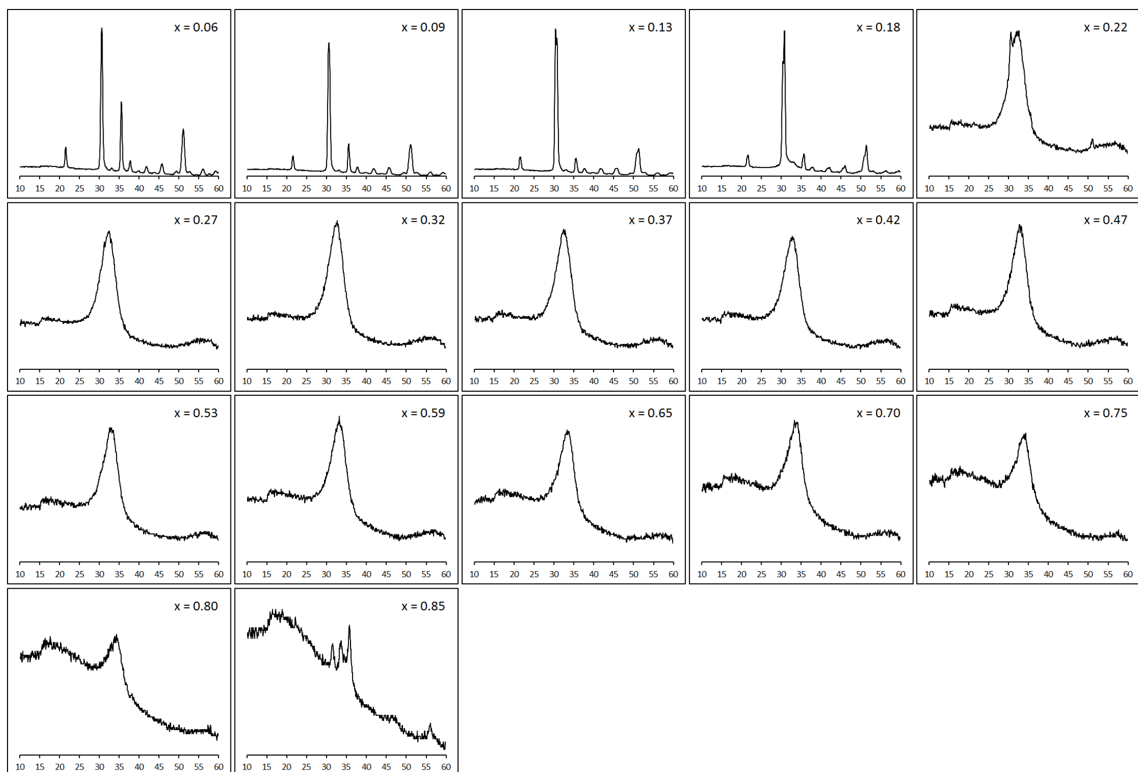

Figure 9.19: XRD results for ZIO films deposited in argon and annealed at 300°C under argon.

oxide-rich end in the films sputtered under argon, while the thermal conductivity of indium-rich films sputtered under oxygen was relatively unaffected by annealing.

9.3.4 Electrical Conductivity of 100% Ar Samples

The as-deposited films were found to be highly electrically conductive (figure 9.20), at approximately 10^5 S/m for all films in the stoichiometric range. This demonstrates clearly the high sensitivity of electrical conductivity to oxygen during annealing, as these films are five to six orders of magnitude more conductive than their counterparts sputtered under 20% oxygen.

Annealing under oxygen results in a significant decrease in electrical conductivity for almost all stoichiometries (figure 9.20). Films around a zinc oxide fraction of 0.3 are the least affected, with a peak in this region at 10^5 S/m. For lower zinc

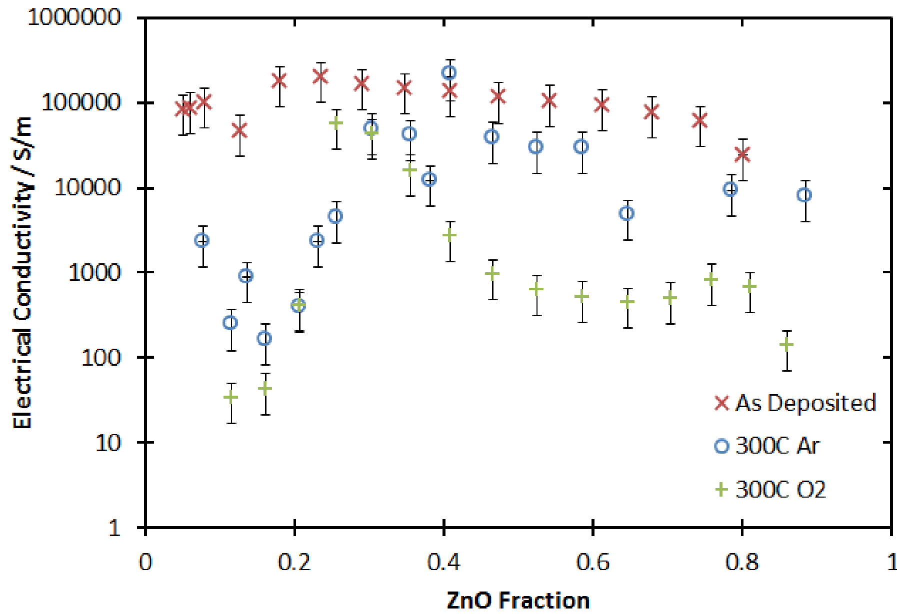

Figure 9.20: Electrical conductivity of ZIO films sputtered in argon as a function of zinc oxide fraction.

oxide concentrations the conductivity drops precipitously, to as low as 10 S/m at a zinc oxide fraction of 0.1, and approaching the as-deposited electrical conductivity of the 20% oxygen sputtered films. Above a zinc oxide fraction of 0.3 the electrical conductivity gradually decreases with increasing zinc oxide concentration, reaching approximately 100 S/m at 90% zinc oxide.

The films annealed under argon are shown in figure 9.20. Films at stoichiometries above a zinc oxide fraction of 0.3 appear to be relatively unaffected by annealing, with conductivities between 10^4 and 10^5 S/m. However, films below this range show a decrease in electrical conductivity. However, this decrease is an order of magnitude less than for films annealed under oxygen, with conductivities between 10^2 and 10^3 S/m.

Charge carrier density in the as-deposited film (figure 9.21) is relatively constant with stoichiometry, around 10^{20} cm^{-3}. Carrier density in the argon-annealed films is slightly lower, except around $x = 0.3$, and appears to mirror the change in electrical conductivity with annealing, within experimental uncertainty. Above $x = 0.3$,

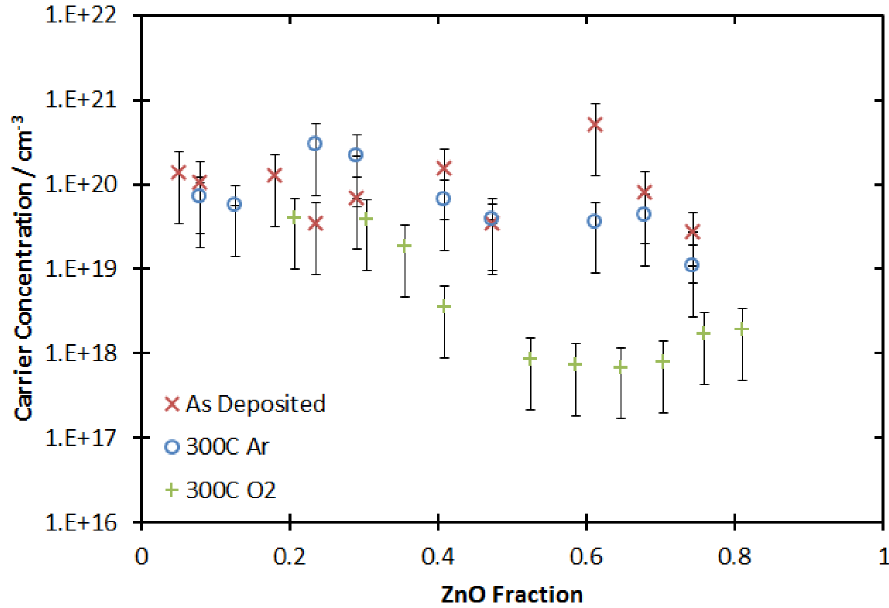

Figure 9.21: Charge carrier concentration in ZIO films sputtered under argon for all three annealing conditions. Of particular note is the lack of difference between the as-deposited and argon-annealed films, while annealing under oxygen significantly reduces carrier density for higher values of x, suggesting that oxygen vacancies in the films are the primary carrier source in zinc-rich ZIO films.

annealing under oxygen results in a two order of magnitude drop in carrier density, consistent with the decrease in electrical conductivity with annealing in this stoichiometric range. Below $x = 0.3$ the electrical conductivity was too low to reliably measure charge carrier density in the oxygen-annealed films.

These data help to demonstrate the critical role of oxygen in both thermal and electric transport in these films. The higher electrical conductivity of the argon-annealed films appears to correlate to higher thermal conductivity, though only by 20-30%. This indicates that neither the electronic nor phonon contribution to thermal conductivity is dominant, and further demonstrated by a two order of magnitude shift in L_{eff} at $x = 0.54$ between the two annealing gas conditions.

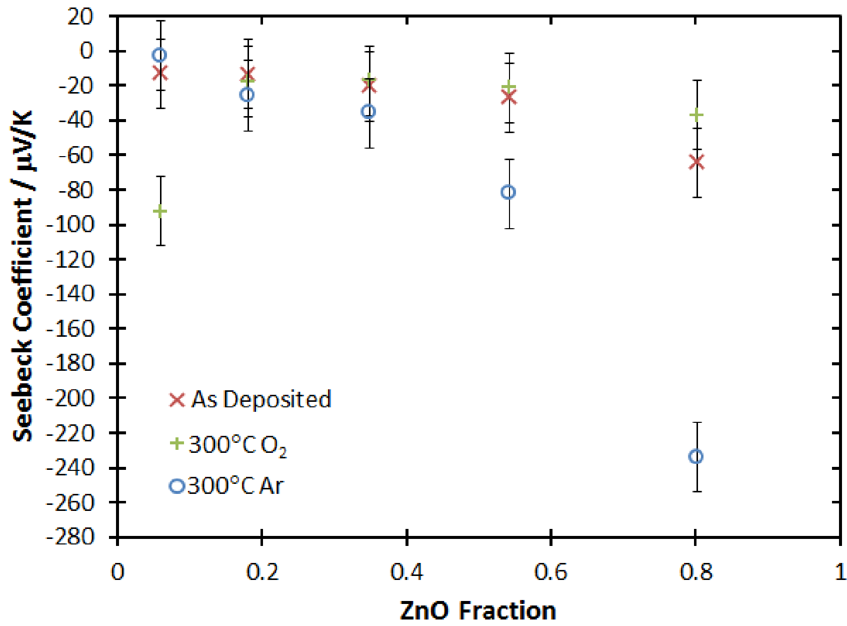

Figure 9.22: Seebeck coefficients for all ZIO films sputtered under argon.

9.3.5 Seebeck Coefficient of 100% Ar Samples

The Seebeck coefficients of the as-deposited films are near zero for $x < 0.6$, similar to the films deposited under oxygen. However, the film around $x = 0.8$ exhibits a relatively high magnitude Seebeck coefficient of -64 μV/K. The oxygen-annealed film appears to be similar to the oxygen-sputtered/oxygen-annealed film, with a Seebeck coefficient of -230 μV/K around $x = 0.8$. Annealing under argon does not appear to significantly affect the Seebeck coefficient, with the exception of the $x = 0.06$ result of -90 μV/K.

The Seebeck results for the oxygen-annealed film appear to be quite similar to both annealed films in the oxygen sputtering condition.

9.3.6 Thermoelectric Figure of Merit

Unlike the other three sputtering conditions examined in chapters 8 and 9, the dimensionless thermoelectric figures of merit for the argon-sputtered ZIO films (table

Table 9.3: Calculated dimensionless figures of merit for ZIO films sputtered under argon, calculated for T = 300 K.

As dep.	x	0.06	0.18	0.34	0.54	0.80
	ZT	0.001±0.001	0.003±0.005	0.006±0.006	0.004±0.004	0.01±0.005
300°C O_2	x	0.06	0.18	0.34	0.54	0.80
	ZT	(0.4±0.3)x10^{-8}	(2±2)x10^{-6}	0.003±0.002	(6±3)x10^{-4}	0.006±0.003
300°C Ar	x	0.06	0.18	0.34	0.54	0.80
	ZT	(5±3)x10^{-4}	(2±3)x10^{-6}	(7±9)x10^{-4}	0.001±0.001	0.001±0.001

9.3) show a relatively high level of consistency. This is particularly true of the as-deposited films where ZT varies only between 0.001 and 0.01 across the range. The as-deposited film at x = 0.80 is also the highest calculated ZT for the sputtering condition at 0.01. Annealing under oxygen results in relatively low ZT, except at x = 0.34, where a value of ZT = 0.003 coincides with the peak in electrical conductivity for this film. Relatively low Seebeck coefficients contribute to a low ZT for argon-annealed films near the indium-rich extreme, while a combination of relatively high electrical conductivity and low thermal conductivity contribute to values of ZT of 0.001 for this annealing condition above x = 0.5. All values of ZT observed fall far below the values found by Amani, et. al. at 300°C[39], as the metallic nature of the argon-sputtered films significantly lowered the Seebeck coefficient across most of the stoichiometric range.

9.4 Effective Lorenz Number

L_{eff} for ZIO samples sputtered under argon are presented in table 9.4. Unsurprisingly, based on the high electrical conductivity seen at all values of x in figure 9.20 the as-deposited film behaves largely as a metal, with L_{eff} within an order of magnitude of

Table 9.4: Calculated effective Lorenz numbers for ZIO films sputtered under argon, calculated for $T = 300$ K.

As dep.	x	0.06	0.18	0.34	0.54	0.80
	$L_{eff}/\frac{W\Omega}{K^2}$	(1±0.6)x10^{-7}	(6±3)x10^{-8}	(7±4)x10^{-8}	(2±1)x10^{-7}	(3±2)x10^{-7}
300°C O_2	x	0.06	0.18	0.34	0.54	0.80
	$L_{eff}/\frac{W\Omega}{K^2}$	(2±1)x10^{-3}	(3±1)x10^{-4}	(4±2)x10^{-7}	(1±0.6)x10^{-5}	(1±0.6)x10^{-5}
300°C Ar	x	0.06	0.18	0.34	0.54	0.80
	$L_{eff}/\frac{W\Omega}{K^2}$	(2±0.8)x10^{-5}	(1±0.7)x10^{-4}	(4±2)x10^{-7}	(4±2)x10^{-7}	(1±0.8)x10^{-6}

L for essentially the entire stoichiometric range.

With the reduced electrical conductivity after annealing, the two annealing gas conditions produce similar results for most of the range, notably diverging around $x = 0.54$ where the argon annealing condition is quite metallic, while the oxygen condition is not. Regardless, outside of the 'peak' in electrical conductivity observed around $x = 0.34$ in figure 9.20 for the two annealing conditions, and the low L_{eff} for argon annealing at $x = 0.54$, the annealing conditions produce effective Lorenz numbers well away from that of an ideal metal, indicating thermal conductivity dominated by phonon contributions.

9.5 ZIO Thermoelectric Study Conclusions

The sensitivity of sputtered ZIO film to oxygen during sputtering is clearly demonstrated in this chapter, particularly in the five order of magnitude difference in electrical conductivity. This is strong evidence for the primary source of mobile charge carriers in ZIO films being oxygen vacancies in the sputtered film.

Unlike the ZTO study, the contribution of electron heat transport is much more muted in ZIO films. There is some evidence that electronic transport contributes

to thermal conductivity on the same order as phonon transport. For example, in the argon sputtering condition, the argon-annealed film is 20-30% more thermally conductive across most of the range than the oxygen-annealed equivalent, without an obvious corresponding increase in crystallinity that could explain an increased phonon contribution, leaving the two order of magnitude difference in charge carrier density to explain the increased thermal conductivity. Oxygen during sputtering and during annealing therefore influences both electrical and thermal transport.

While an oriented ZnO phase was clearly visible in virtually all ZTO data, the ZnO phase in the ZIO study is much more muted, and appears largely unaffected by annealing. In addition, sputtering under argon appears to diminish the appearance of this phase. Both thermal and electrical conductivity are significantly lower in ZnO-rich films mixed with indium oxide than in films mixed with tin oxide, indicating that the presence of indium oxide interferes with the formation of a distinct polycrystalline ZnO phase.

In this chapter, as-deposited films exhibited relatively low Seebeck coefficients, and annealing helped to increase them. The 'peak' of Seebeck coefficients occurred around $x = 0.7$ or $x = 0.8$ in the oxygen annealing conditions, corresponding to a trough in carrier density in both cases.

Chapter 10

Conclusions and Future Work

The initial TFT portion of this study sought to examine thin film transistor performance, particularly the values of saturation field effect mobility and inverse subthreshold swing, as a function of stoichiometry in mixtures of zinc oxide with either tin(iv) oxide or indium(iii) oxide. These studies produced a number of interesting results, particularly regarding high mobility at particular stoichiometries. In the ZTO study, two peaks were found after annealing at 600°C under oxygen, both on the order of 10 $cm^2/V{\cdot}s$, at $x = 0.3$ and $x = 0.8$. In the ZIO study only half of the stoichiometric range could be examined using TFT devices, but a peak in mobility of 30 $cm^2/V{\cdot}s$ was found near $x = 0.7$, when annealed at 300°C under oxygen, while a 600°C annealing condition was found to be detrimental to transistor performance. These devices also offered on/off ratios as high as 10^6 and sub-1 V/decade inverse sub-threshold swings. These studies produced two publications[101, 102].

Brief XRD measurements after the TFT study revealed the films to have many stoichiometries that appeared to be largely amorphous in nature. This suggested that they may therefore also be of low thermal conductivity. This result, coupled with the high mobility results, suggested that both films might be interesting in a thermoelectric context. Other work[65] at fixed mixed ratios of ZIO suggested that the influence of oxygen during sputtering might significantly effect the electrical properties of these films. The decision to examine the films from a thermoelectric point of view (i.e. to determine ZT as a function of fabrication parameters) resulted in the bulk of this study. However, the study expanded beyond simple determination of ZT, to include an examination of the nature of thermal and electrical conduction in the materials.

While devices and facilities were available to measure electrical conductivity and Seebeck coefficients, the method used to create the combinatorial films necessitated the use of an indirect method of measurement for determination of the thermal conductivity of the films. The 3ω method was chosen for this measurement, due to its relative simplicity and the availability of the DSP lock-in amplifier necessary for its application. Initially, all 3ω measurements were carried out manually, using calculations to model the film stack and determine thermal conductivity. However, a single, reliable manual measurement using any heater was found to take a great deal of time (on the order of several hours). This made 'debugging' the fabrication and measurements of combinatorial arrays very difficult.

An automated system for measuring many different heaters relatively quickly was developed. This made measurements, and therefore the optimization of the fabrication and measurement processes, much quicker. To demonstrate that the method was reliable, a brief study of sputtered SiO_2 thin films as a function of film thickness was conducted[103]. The results were consistent with literature values for sputtered SiO_2, demonstrating that the automated method was capable of delivering accurate results. This study was instrumental in identifying and eliminating a large number of issues with the system as initially designed, such as unreliable data when using a chromium 'binding' layer with nickel, or 'hot spots' in mask design used for patterning the heaters.

Initially the fabrication conditions used for both ZTO and ZIO were matched to those used in the TFT studies. However, a second set of films was fabricated for each material under pure argon, to help shed light on the influence of oxygen vacancies in both electrical and thermal transport.

All data taken for a particular set of fabrication conditions were measured using films created in a single sputtering run. In addition, for a given set of sputtering conditions, the pre-annealed films were all from the same sputtering run. Therefore, combined values, such as ZT are as-measured for a single sample, and do not represent an aggregate of data from multiple, different fabrications.

In the ZTO films, sputtering under argon was found to result in a significantly more electrically conductive film compared to sputtering under oxygen, likely due to an increase in oxygen deficiency in the argon-sputtered film. In addition, thermal conductivity in the more electrically conductive argon-sputtered film appeared to be primarily due to the electronic contribution, as electrical conductivity mirrored thermal conductivity. The oxygen-sputtered film was highly resistive, and exhibited very low thermal conductivity, except where crystalline structure was visible near the ZnO edge. This ZnO phase was visible in all ZTO films, and appears to have a preferred orientation, based on the relative intensities of the visible peaks in XRD measurements. Crystal structure is also visible in some films near the SnO_2 edge, particularly for 600°C annealed films. A tin-metal phase is visible along with an SnO_2 phase in the argon-sputtered, argon-annealed films. This is further evidence of a strongly oxygen-deficient film. A narrow peak in thermal conductivity is observed coincident with the formation of a Zn_2SnO_4 phase that is visible in the 600°C annealed films.

Annealing under oxygen at 600°C appeared to effectively 'fill' oxygen vacancies. In the argon-sputtered films, annealing in oxygen produced a drop in charge carrier density of as much as four orders of magnitude. Interestingly, annealing under argon also produced a large drop in carrier density, but of 1-2 orders of magnitude less, implying that unbound, trapped oxygen was present in the films as-deposited, or that annealing 'healed' donor-like defects. Annealing under oxygen also caused a reduction in thermal conductivity, supporting the assertion that the electronic contribution to thermal conductivity was significant in these films.

Seebeck coefficient magnitudes tended to be highest in the as-deposited films, with 600°C annealing conditions resulting in low-magnitude Seebeck coefficients of around -40 μV/K. The oxygen-sputtered, 300°C annealed and the as-deposited argon sputtered films produced relatively high magnitude Seebeck coefficients of as much as -260 μV/K.

Because the electronic contribution to thermal conductivity is high in these films,

high electrical conductivity tended to come at the cost of high thermal conductivity as well. In addition, the films with high electrical conductivity required annealing, resulting in low Seebeck coefficients. As a result, ZT calculated for the ZTO films was generally low. The highest observed value of 0.06 occurred in the oxygen-sputtered, 600°C oxygen-annealed film, very near the pure ZnO extreme ($x = 0.98$). The best 'low processing temperature' thermoelectric film was the argon-sputtered, as-deposited film, with a value for ZT of 0.004 at $x = 0.92$. The next best was $ZT = 0.0002$ for the same film at $x = 0.39$.

In the ZIO films crystallinity was generally only visible near the indium oxide edge of the sputtering track. The presence of indium oxide appeared to interfere more strongly with the formation of a ZnO phase than had the tin oxide in the ZTO samples, as the ZnO peaks in the ZIO films are never as clearly visible, despite generally thicker films (and therefore higher XRD intensities). Thermal conductivity was fairly low in all oxygen-sputtered films, with a slight rise visible near the indium oxide edge. Annealing under oxygen and argon produced an increase in electrical conductivity, which was roughly the same regardless of annealing gas. This indicates that the oxygen-sputtered films are not strongly oxygen-deficient. In these oxygen-sputtered films, thermal conductivity did not appear to vary with electrical conductivity, indicating a weak electronic contribution to thermal conductivity.

In the argon sputtered films electrical conductivity was highest in the as-deposited film, at around 10^5 S/m at all stoichiometries. In this case, annealing caused a reduction in electrical conductivity, except at a peak around $x = 0.3$. Both XRD and thermal conductivity data indicated an increase in crystallinity in the annealed films near the indium oxide end of the range. Charge carrier density was shown to be much lower in the oxygen-annealed films (except near the peak at $x = 0.3$) compared to both the as-deposited and argon-annealed films. Annealing under argon did not appear to significantly affect carrier density, further demonstrating the oxygen sensitivity of the films. The higher electrical conductivity and carrier density of the argon-annealed film caused only a slight increase in thermal conductivity compared

to the oxygen-annealed film. Again, this indicated that electronic contributions to thermal conductivity are relatively insignificant.

Seebeck coefficients in the ZIO films were found to increase with annealing, with values for the as-deposited films being near zero. In both sputter gas conditions the 'peak' measured Seebeck coefficient was around $x = 0.7$ or $x = 0.8$, at a magnitude as high as -260 μV/K. Oxygen-annealed films produced the highest magnitude coefficients. The argon-sputtered, oxygen-annealed film also produced a relatively high peak Seebeck coefficient. There was some indication that oxygen in a ZIO film played an important role in determining the Seebeck coefficients of that film.

Films both sputtered and annealed under oxygen at 300°C produced the highest values for ZT, of 0.02±0.01 and 0.01±0.005 at $x = 0.47$ and $x = 0.67$, respectively. ZT for the argon-annealed version of this film was approximately an order of magnitude lower at the same stoichiometric ratios. While ZT for films sputtered under oxygen was generally lower, the as-deposited (i.e. low processing temperature) ZT values were relatively high, the most notable being $ZT = 0.01$ at $x = 0.80$, excellent for a room-temperature fabricated and tested film.

10.1 Future Work

The study of annealing temperature in ZTO films was limited by the fact that films could not be annealed after deposition of metal contacts, requiring a 'fresh', as-deposited sample to be annealed prior to testing. However, it is clear from the results in chapter 8 that annealing temperature may be a useful avenue of exploration for optimizing ZT. Specifically, it may be possible to find an optimum annealing temperature between 300°C and 600°C at which ZT is optimized (i.e. where electrical conductivity is increased without the observed decrease in Seebeck coefficient). In addition, exploration of a range of oxygen contents during sputtering between 0% and 10% may be used to further optimize ZT, again by maximizing electrical conductivity while maintaining Seebeck coefficient.

The ZTO films used here were observed to be very 'tough', in that they were highly resistant to scratches or cracking. For example, films deposited on thin, slide-cover glass were found to maintain electrical conductivity, even after significant flexing of the substrate. A study of the growth of these films on low-cost, flexible substrates, likely at a fixed stoichiometric ratio at a range of thicknesses, may be interesting for any future use of ZTO in low-cost devices. An XRD study of the films on non-crystalline substrates would also yield interesting information about the oriented ZnO phase observed near the zinc-rich end of the stoichiometric range. Growth of the film on a randomly oriented substrate may result in less oriented, less thermally conductive films in this region, and a correspondingly higher ZT.

The ZIO study yielded values for ZT that were consistent with literature[104], reaching as much as 0.02. It is clear from the results in chapter 9 that the thermoelectric properties of ZIO are exquisitely sensitive to oxygen, during both sputtering and annealing. As with the ZTO study, a more detailed exploration of the range of oxygen partial pressure values during sputtering is warranted. This is particularly true in the case of ZIO as increasing oxygen content during sputtering to 20% significantly increased the determined value of ZT around the $x = 0.5$ stoichiometry. With this in mind, a study of oxygen partial pressure during sputtering both for lesser and greater oxygen values would help to find a peak in thermoelectric performance. The Seebeck coefficient of the ZIO films was also found to be highly sensitive to annealing, and ZT could again be optimized via a study of a range of annealing temperatures under oxygen.

While ZIO was not observed to be as 'tough' as ZTO, being more likely to 'flake' and otherwise deform under stress, sputtering of ZIO films onto flexible substrates would be an interesting avenue of experiment. Given the lower temperatures at which annealing produced positive results, it may be possible to do relatively low-temperature annealing on organic substrates such as teflon or thermoset polyimide.

Both ZTO and ZIO films were observed to be partially transparent. A cursory study to quantify this transparency as a function of stoichiometry was undertaken

during the TFT phase of the experiment. However, this aspect of the materials was not pursued in detail due to time constraints. Future studies of these sputtered films could include an examination of this transparency as a function of the various fabrication parameters discussed.

Finally, the combinatorial, thin-film thermal conductivity measurement system developed for this study is not limited to use on only ZIO and ZTO, and other systems, such as the Indium-Gallium-Oxide system, can be studied. Further, the combinatorial sputtering system used is capable of creating ternary systems. With further optimization, including a larger number of heaters spread across a larger area of the substrate, this system could be used for studying ternary systems, such as the indium-gallium-zinc-oxide system.

While not implemented due to time constraints, an implementation of the heaters used in the 3ω method to determine Seebeck coefficient was briefly explored. In brief, an area of the film of interest is given a temperature amplitude at 2ω, as in a 3ω measurement. A voltage sense line is patterned on the film below the heater, separated electrically from the heater metal by an insulating layer. The difference in potential at frequency 2ω between this sense lead and another point on the film that is unheated is taken to be due to Seebeck coefficient. This is known as the 2ω method[105] and it could, in combination with the combinatorial 3ω method presented here, be used to take all the necessary measurements for calculated ZT on a single-substrate combinatorial library.

References

[1] R. L. Hoffman, B. J. Norris, and J. F. Wager *Applied Physics Letters*, vol. 82, p. 733, 2003.

[2] P. F. Carcia, R. S. McLean, M. H. Reilly, and G. Nunes *Applied Physics Letters*, vol. 82, p. 1117, 2003.

[3] M. McDowell, I. G. Hill, J. E. McDermott, S. L. Bernasek, and J. Schwartz *Applied Physics Letters*, vol. 88, p. 073505, 2006.

[4] D. J. Gundlach, T. N. Jackson, Y. Y. Lin, and D. G. Schlom *IEEE Electron Device Letters*, vol. 17, p. 87, 1997.

[5] N. L. Dehuff, E. S. Kettenring, D. Hong, H. Q. Chiang, J. F. Wager, R. L. Hoffman, C.-H. Park, and D. A. Keszler *Journal of Applied Physics*, vol. 97, p. 064505, 2005.

[6] H. Q. Chiang, D. Hong, C. M. Hung, R. E. Presley, J. F. Wager, C.-H. Park, G. S. Herman, and D. A. Keszler *J. Vac. Sci. Technol. B*, vol. 24, p. 2702, 2006.

[7] H. Q. Chiang, J. F. Wager, R. L. Hoffman, J. Jeong, and D. A. Keszler *Applied Physics Letters*, vol. 86, p. 013503, 2005.

[8] W. B. Jackson, R. L. Hoffman, and G. S. Herman *Applied Physics Letters*, vol. 87, p. 193503, 2005.

[9] R. E. Presley, C. L. Munsee, C.-H. Park, D. Hong, J. F. Wager, and D. A. Keszler *Journal of Physics D: Applied Physics*, vol. 37, p. 2810, 2004.

[10] H. Q. Chianga, J. F. Wager, R. L. Hoffman, J. Jeong, and D. A. Keszler *Applied Physics Letters*, vol. 86, p. 013503, 2005.

[11] H. Q. Chiang, A. D. Hong, C. M. Hung, R. E. Presley, J. F. Wager, C.-H. Park, D. A. Keszler, and G. S. Herman *J. Vac. Sci. Technol. B*, vol. 24, p. 2702, 2006.

[12] J. D. Perkins, J. A. del Cueto, J. L. Alleman, C. Warmsingh, B. M. Keyes, L. M. Gedvilas, P. A. Parilla, B. To, D. W. Readey, and D. Ginley *Thin Solid Films*, vol. 411, pp. 152–160, 2002.

[13] Y. J. Chang, D. H. Lee, G. S. Herman, and C. H. Chang *Electrochemical and Solid-State Letters*, vol. 10, pp. H135–H138, 2007.

[14] T. Minami, S. Takata, H. Sato, and H. J. Sonohara *Vac. Sci. Technol. A*, vol. 13, p. 1095, 1995.

[15] W. B. Jackson, G. S. Herman, R. L. Hoffman, C. Taussig, S. Braymen, F. Jeffery, and J. Hauschildt *Journal of Non-Crystalline Solids*, vol. 352, pp. 1753–1755, 2006.

[16] W. B. Jackson, G. S. Herman, R. L. Hoffman, C. Taussig, S. Braymen, F. Jeffrey, and J. Hauschildt *Jour. Non-Cryst. Soli.*, vol. 352, pp. 1753–1755, 2006.

[17] D. Kovachera and K. Petrov *Solid State Ionics*, vol. 109, p. 327, 1998.

[18] D. L. Young, H. Moutinho, A. T. Yan, and J. Coutts, T. J. *Journal of Applied Physics*, vol. 92, p. 310, 2002.

[19] D. L. Young, D. L. Williamson, and T. J. Coutts *Journal of Applied Physics*, vol. 91, p. 1464, 2002.

[20] R. Hoffman *Solid-State Electronics*, vol. 50, pp. 784–787, 2006.

[21] E. Fortunato, P. Barquinha, A. Pimentel, L. Pereira, G. Goncalves, and R. Martins *Physica Status Solidi (RRL)*, vol. 1, p. R34, 2007.

[22] B. Yaglioglu, H. Y. Yeom, R. Beresford, and D. C. Paine *Applied Physics Letters*, vol. 89, p. 062103, 2006.

[23] G. Gonalves, P. Barquinhaa, L. Ranieroa, R. Martinsa, and E. Fortunato *Thin Solid Films*, vol. 516, pp. 1374–1376, 2008.

[24] N. L. Dehuff, E. S. Kettenring, D. Hong, H. Q. Chiang, J. F. Wager, R. L. Hoffman, C. H. Park, and D. A. Keszler *Applied Physics Letters*, vol. 97, p. 064505, 2005.

[25] J.-I. Song, J.-S. Park, H. Kim, Y.-W. Heo, J.-H. Lee, J.-J. Kim, G. M. Kim, and B. D. Choi *Applied Physics Letters*, vol. 90, p. 022106, 2007.

[26] W. Lima, Y.-L. Wangb, F. Renb, D. Nortona, I. Kravchenkoc, J. Zavadad, and S. Peartona *Applied Surface Science*, vol. 254, pp. 2878–2881, 2008.

[27] Y.-L. Wang, L. N. Covert, T. J. Anderson, W. Lim, J. Lin, S. J. Pearton, D. P. Norton, J. M. Zavada, and F. Ren *Electrochemical and Solid-State Letters*, vol. 11, pp. H60–H62, 2008.

[28] F. Utsuno, H. Inoue, Y. Shimane, T. Shibuya, K. Yano, K. Inoue, I. Hirosawa, M. Sato, and T. Honma *Thin Solid Films*, vol. 516, p. 58185821, 2008.

[29] R. Martins, P. Barquinha, A. Pimentel, L. Pereira, E. Fortunato, D. Kang, I. Song, C. Kim, J. Park, and Y. Park *Thin Solid Films*, vol. 516, p. 13221325, 2008.

[30] T. Iwasaki, N. Itagaki, T. Den, and H. Kumomi *Applied Physics Letters*, vol. 90, p. 242114, 2007.

[31] A. M. Omer *Renewable and Sustainable Energy Reviews*, vol. 12, p. 2331, 2008.

[32] M. H. Elsheikh, D. A. Shnawah, M. F. M. Sabri, S. B. M. Said, M. H. Hassan, M. B. A. Bashir, and M. Mohamad *Renewable and Sustainable Energy Reviews*, vol. 30, no. 0, pp. 337 – 355, 2014.

[33] A. F. Ioffe, *Semiconductor Thermoelements and Thermoelectric Cooling*. Infosearch Ltd, London, 1957.

[34] H. Goldsmid, "Theory of thermoelectric refrigeration and generation," in *Introduction to Thermoelectricity*, vol. 121 of *Springer Series in Materials Science*, pp. 7–21, Springer Berlin Heidelberg, 2009.

[35] D. Nemir and J. Beck *Journal of Electronic Materials*, vol. 39, p. 1897, 2010.

[36] J. G. Snyder and E. S. Toberer *Nature Materials*, vol. 7, p. 105, 2008.

[37] A. I. Hochbaum, R. Chen, R. D. Delgado, W. Liang, E. C. Garnett, M. Najarian, A. Majumdar, and P. Yang *Nature*, vol. 451, pp. 163–167, 2008.

[38] M. Xie and D. M. Gruen *Journal of Physical Chemistry B*, vol. 114, p. 14339, 2010.

[39] M. Amani, I. M. Tougas, O. J. Gregory, and G. C. Fralick *Journal of Electronic Materials*, vol. 42, pp. 114–120, 2013.

[40] C. Wan, Y. Wang, N. Wang, and K. Koumoto *Materials*, vol. 3, no. 4, pp. 2606–2617, 2010.

[41] B. B. Iversen, A. E. Palmqvist, D. E. Cox, G. S. Nolas, G. D. Stucky, N. P. Blake, and H. Metiu *Journal of Solid State Chemistry*, vol. 149, no. 2, pp. 455 – 458, 2000.

[42] K. P. Ong, D. J. Singh, and P. Wu *Phys. Rev. B*, vol. 83, p. 115110, Mar 2011.

[43] Y. Tanaka, T. Ifuku, K. Tsuchida, and A. Kato *Journal of Materials Science Letters*, vol. 16, no. 2, pp. 155–157, 1997.

[44] M. Ohtaki and R. Hayashi, "25th international conference on thermoelectrics, 2006.," pp. 276–279, 2006.

[45] P. Jood, R. J. Mehta, Y. Zhang, G. Peleckis, X. Wang, R. W. Siegel, T. Borca-Tasciuc, S. X. Dou, and G. Ramanath *Nano Letters*, vol. 11, pp. 4337–4342, 2011.

[46] Y. Yang, K. C. Pradel, Q. Jing, J. M. Wu, F. Zhang, Y. Zhou, Y. Zhang, and Z. L. Wang *ACS Nano*, vol. 6, no. 8, pp. 6984–6989, 2012.

[47] X. Qu, W. Wang, S. Lv, and D. Jia *Solid State Communications*, vol. 151, no. 4, pp. 332 – 336, 2011.

[48] H. Colder, E. Guilmeau, C. Harnois, S. Marinel, R. Retoux, and E. Savary *Journal of the European Ceramic Society*, vol. 31, no. 15, pp. 2957 – 2963, 2011.

[49] K.-H. Jung, K. H. Lee, W.-S. Seo, and S.-M. Choi *Applied Physics Letters*, vol. 100, no. 25, p. 253902, 2012.

[50] H. Jingfeng, T. A. I. Yoong, and H. H. Hoon, *Nanostructured ZnO Thermoelectric Materials for Microelectronics*. LAP Lambert Academic Publishing, 2013.

[51] P. Kumar, M. Kar, A. V. Sanchela, C. V. Tomy, and A. D. Thakur, "Solid state physics: Proceedings of the 57th dae solid state physics symposium 2012.," 2012.

[52] M. Sndergaard, E. D. Bjesen, K. A. Borup, S. Christensen, M. Christensen, and B. B. Iversen *Acta Materialia*, vol. 61, no. 9, pp. 3314 – 3323, 2013.

[53] L. Wang, C.-Y. Chang, S.-T. Yeh, S. W. Chen, Z. A. Peng, S. C. Bair, D. Lee, F. Liao, and Y. Kuo *Ceramics International*, vol. 38, no. 2, pp. 1167 – 1174, 2012.

[54] X. Zhou, H. Zhang, Q. Chen, J. Shang, and P. Zhang *Thin Solid Films*, vol. 519, no. 10, pp. 3026 – 3028, 2011.

[55] S. Isobe, T. Tani, Y. Masuda, W.-S. Seo, and K. Koumoto *Japanese Journal of Applied Physics*, vol. 41, pp. 731–732, 2002.

[56] H. Kaga, R. Asahi, and T. Tani *R and D Review of Toyota CRDL*, vol. 41, 2006.

[57] M. Amani, I. M. Tougas, O. J. Gregory, and G. C. Fralick *Journal of Electronic Materials*, vol. 42, pp. 114–120, 2006.

[58] Y. Wu. PhD thesis, Arizona State University, 2011.

[59] P. Jood. PhD thesis, University of Wollongong, 2012.

[60] J. H. Ko, I. H. Kim, K. S. Lee, T. S. Lee, B. Cheong, and W. M. Kim *Applied Surface Science*, vol. 253, pp. 7398–7403, 2007.

[61] O. J. Gregory and M. Amani *Journal of The Electrochemical Society*, vol. 158, 2011.

[62] A. Rolland, J. Richard, J. P. Kleider, and D. Mencaraglia *Journal of the Electrochemical Society*, vol. 140, p. 3679, 1993.

[63] K. Biswas, J. He, I. D. Blum, C.-I. Wu, T. P. H. D. N. Seidman, V. P. Dravid, and M. G. Kanatzidis *Nature*, vol. 489, pp. 414–418, 2012.

[64] L. J. van der Pauw *Philips Research Reports*, vol. 13, pp. 1–9, 1958.

[65] R. Martins, P. Barquinha, A. Pimentel, L. Pereira, and E. Fortunato *Phys. Stat. Sol.*, vol. 202, p. R95, 2005.

[66] S. Isobe, T. Tani, Y. Masuda, W. Seo, and K. Koumoto *Japanese Journal of Applied Physics*, vol. 41, p. 731, 2002.

[67] H. Kaga, R. Asahi, and T. Tani *Japanese Journal of Applied Physics*, vol. 43, p. 3540, 2004.

[68] T. Ashida, A. Miyamura, Y. Sato, T. Yagi, N. Taketoshi, T. Baba, and Y. Shigesato *J. Vac. Sci. Technol. A*, vol. 25 (4), p. 1178, 2007.

[69] B. Su-Yuan, T. Zhen-An, H. Zheng-Xing, Y. Jun, and W. Jia-Qi *Chin. Phys. Lett.*, vol. 25, p. 593, 2008.

[70] D. G. Cahill *Review of Scientific Instruments*, vol. 61, p. 802, 1990.

[71] T. M. Tritt, ed., *Thermal Conductivity: Theory, Properties, and Applications.* Springer, 2004.

[72] S. M. Lee and D. G. Cahill *J. Appl. Phys.*, vol. 81, pp. 2590–2595, 1997.

[73] F. R. Brotzen, P. J. Loos, and D. P. Brady *Thin Solid Films*, vol. 207, pp. 197–201, 1992.

[74] J. C. H. Henager and W. T. Pawlewicz *Applied Optics*, vol. 32, pp. 91–101, 1993.

[75] T. Yamane, N. Nagai, S. ichiro Katayama, and M. Todoki *Journal of Applied Physics*, vol. 91, pp. 9772–9776, 2002.

[76] H. B. Callen, *Thermodynamics and an Introduction to Thermostatistics.* John Wiley and Sons, 1960.

[77] R. Franz and G. Wiedemann *Annalen der Physik*, vol. 165, pp. 497–531, 1853.

[78] P. J. Kelly and R. D. Arnell *Vacuum: Surface Engineering, Surface Instrumentation and Vacuum Technology*, vol. 56, pp. 159–172, 2000.

[79] J. R. Dahn, S. Trussle, T. D. Hatchard, A. Bonakdarpour, J. N. Meuller-Neuhaus, K. C. Hewitt, and M. Fleischauer *Chemistry of Materials*, vol. 14, p. 3519, 2002.

[80] H. J. Levinson, *Principles of Lithography.* SPIE Press, 2011.

[81] K. E. Petersen *Proceedings of IEEE*, vol. 70, p. 421, 1982.

[82] H. R. SHanks, P. D. Maycock, P. H. Sidles, and G. C. Danielson *Physical Review*, vol. 130, p. 1743, 1963.

[83] P. Benjamin and C. Weaver *Proceedings of the Royal Society of London. Series A*, pp. 516–531, 1961.

[84] K. R. Neumaier, G. Elender, E. Sackmann, and R. Merkel *Europhysics Letters*, vol. 49, pp. 14–19, 2000.

[85] A. Janotti and C. G. V. de Walle *Reports on Progress in Physics*, vol. 72, p. 126501, 2009.

[86] A. P. Mackenize *Rep. Prog. Phys*, vol. 56, p. 557, 1993.

[87] B. E. Warren, *X-Ray Diffraction.* Dover Books on Physics, 1990.

[88] D. G. Cahill, H. E. Fischer, T. Klitsner, E. T. Swartz, and R. O. Pohl *J. Vac. Sci. Technol. A*, vol. 7, pp. 1259–1266, 1989.

[89] H. R. Shanks, P. D. Maycock, P. H. Sidles, and G. C. Danielson *Phys. Rev.*, vol. 130, pp. 1743–1748, Jun 1963.

[90] D. Drouin, "Casino," Dec 2013. http://www.gel.usherbrooke.ca/casino/index.html.

[91] P. Barquinha, A. Pimentel, A. Marques, L. Pereira, R. Martins, and E. Fortunato *Journal of Non-Crystalline Solids*, vol. 352, pp. 1749–1752, 2006.

[92] J. H. Kim, A. Feldman, and D. Novotny *Journal of Applied Physics*, vol. 86, pp. 3959–3963, 1999.

[93] R. Kato and I. Hatta *International Journal of Thermophysics*, vol. 26, pp. 179–190, 2005.

[94] C. J. Glassbrenner and G. A. Slack *Phys. Rev.*, vol. 134, pp. A1058–A1069, 1964.

[95] S. Graulis, A. Dakevi, A. Merkys, D. Chateigner, L. Lutterotti, M. Quirs, N. R. Serebryanaya, P. Moeck, R. T. Downs, and A. Le Bail *Nucleic Acids Research*, vol. 40, no. D1, pp. D420–D427, 2012.

[96] S. Gražulis, D. Chateigner, R. T. Downs, A. F. T. Yokochi, M. Quirós, L. Lutterotti, E. Manakova, J. Butkus, P. Moeck, and A. Le Bail *Journal of Applied Crystallography*, vol. 42, pp. 726–729, Aug 2009.

[97] R. T. Downs and M. Hall-Wallace *American Mineralogist*, vol. 88, pp. 247–250, 2003.

[98] A. Le Bail *Journal of Applied Crystallography*, vol. 38, pp. 389–395, Apr 2005.

[99] Y. Xu, M. Goto, R. Kato, Y. Tanaka, and Y. Kagawa *Journal of Applied Physics*, vol. 111, p. 084320, 2012.

[100] I. C. of America, "Material Safety Data Sheet (MSDS)," 2014.

[101] M. G. McDowell, R. J. Sanderson, and I. G. Hill *Applied Physics Letters*, vol. 92, p. 013502, 2008.

[102] M. G. McDowell and I. G. Hill *IEEE Transactions on Electron Devices*, vol. 56, pp. 343–347, 2009.

[103] M. G. McDowell and I. G. Hill *Review of Scientific Instruments*, vol. 84, p. 053906, 2013.

[104] P. Jood, R. J. Mehta, Y. Shang, T. Borca-Tasciuc, S. X. Dou, D. J. Singh, and G. Ramanath *RSC Adv.*, vol. 4, p. 6363, 2014.

[105] T. Miao, W. Ma, X. Zhang, and Z. Li *Review of Scientific Instruments*, vol. 82, no. 2, p. 024901, 2011.

Appendix A

Uncertainties

For the thermoelectric portion of this study, determination of uncertainties was crucial as the reported values are determined from a large number of independent measurements. This section will outline the various sources of uncertainty in measurements used during the thermoelectric study.

Uncertainties were not reported for measurement on devices in the transistor portion of this study (chapter 6), owing to the large number of devices (and therefore measurements) available. The high density of data points over the stoichiometric range made it possible to observe systematic behaviour without considering of the uncertainty of an individual measurement. However, various sources of uncertainty exist for these measurements, the most significant of which is in the linear fit used to determine saturation mobility and threshold voltage (see figure 2.2).

A.1 Thermal Conductivity

The conductivity of the thin films was taken to be due to the difference in temperature amplitude between a heater sitting on a stack of films and an adjacent heater on a similar stack of films, but without the film of interest. To find this difference, the temperature amplitude per unit power of each heater was determined using equation (2.50). The uncertainty of each of these measurements depended on the uncertainty in R, C_{RT} and the first and third harmonic voltages. C_{RT} was determined using a series of AC current and voltage measurements for a variety of applied voltages of each heater as it cooled over approximately 20°C. The slope of R with respect to temperature was then calculated, resulting in a very low uncertainty measurement of

less than 5%. The determined value of C_{RT} and its uncertainty was then used for all subsequent calculations for the heater.

R was determined for each temperature amplitude measurement, by simultaneously measuring AC current and $V_{1\omega}$. The uncertainty for this value was extremely small, and was neglected.

The first harmonic voltage measurement was stable to one part in one thousand and was neglected. Uncertainty in the third harmonic voltage often dominated temperature amplitude measurements due to the low magnitude of this voltage relative to the first harmonic voltage. For each heater, 30 - 40 temperature amplitude per unit power measurements were taken at a variety of applied powers and frequencies. The standard deviation of these measurements over the root of the number of measurements was taken to be the standard error in temperature amplitude due to the third harmonic voltage. The error when determining the difference in temperature amplitude between adjacent heaters was the sum of these individual uncertainties.

For converting this temperature amplitude difference into a film thermal conductivity, the thickness of the film and width and length of the heater were also required. Heater width in all cases was 25 $\mu m \pm 1$ μm, as determined using microscope photos of standard heaters (see figure A.1).

Both the heater width and length are subject to the same fabrication methods, so the uncertainty in heater length was assumed to be the same as it was for the width. Since this length was 1.4 mm for all heaters, the uncertainty in this value was neglected. The final value used to calculate film thermal conductivity was the film thickness. This was determined using spectroscopic ellipsometry and profilometry. The difference in measurements between these two techniques over several fabrications runs led to a general ±10% uncertainty being assumed for all film thicknesses measured using ellipsometry.

The uncertainty in $V_{3\omega}$ and film thickness were by far the dominant sources of error when determining film thermal conductivity. Thinner and/or more conductive films led to higher uncertainty.

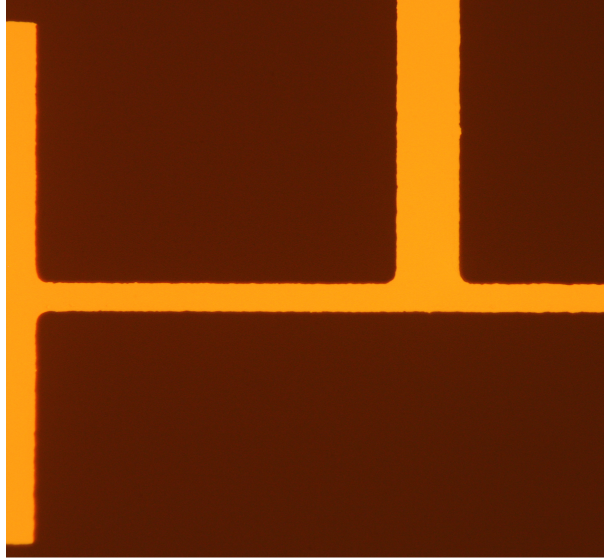

Figure A.1: Close up view of a standard heater. The horizontal line is the heater element, with a width of 25 μm.

A.2 Electrical Conductivity

Electrical conductivity measurements were done using sheet resistance and the film thickness. The sheet resistance depended on a number of 4-wire resistance measurements, as well as the film thickness. Uncertainty in film thickness was discussed previously and was taken to be ± 10%. Scatter in the 4-wire resistance measurements themselves also contributed an uncertainty of approximately 10%.

However, the van der Pauw technique used to determine the conductivity of these films also requires that the thickness of the films be uniform. This increased the uncertainty for two reasons. First, film thickness for some samples could vary noticeably over the width of the cloverleaf structure owing to a thickness change across the width of the sputtering track. However, due to the small size of the cloverleaf structures relative to the width of the sputtering track and the smooth change in thickness across all samples, this effect was neglected. Second, due to the stencil mask technique used to pattern the cloverleaf structures, the thickness did not fall off as a 'step edge' at the perimeter of the structure. The distance over which the thickness of the film was found to go from full thickness to zero was about 1/5 of the

width of the thinnest parts of the structure, so the thickness was assumed to vary by 20%. Adding these three effects in quadrature resulted in a $\pm$ 25% uncertainty being assumed for all electrical conductivity data taken using cloverleaf structures.

For very high resistivity measurements taken using films on glass slides, the 10% uncertainty in film thickness was taken to be the uncertainty in the measurement.

A.3 Seebeck Coefficient

Seebeck voltage measurements were done using the Physical Properties Measurement System. All values supplied by this device varied inside of a range of approximately $\pm$ 20 $\mu V/K$, so this was taken to be the uncertainty of Seebeck coefficient measurements.

A.4 Carrier Concentration

Carrier concentration was determined using a technique very similar to that of the sheet resistance measurements, using the same structures and similar assumptions about film thickness. The electrical conductivity measurement was also used as part of this calculation. Therefore carrier concentration numbers are the result of two 25% uncertainties added in quadrature, or about 35%.

A.5 Thermoelectric Figure of Merit and Effective Lorenz Number

The thermoelectric figure of merit and Lorenz numbers provided here are combinations of the value discussed above, and have values that are added in quadrature. It was not uncommon for the uncertainty of a value to exceed the value itself, usually due to the high uncertainty in low-value Seebeck coefficient measurements with fixed uncertainty (instead of a percentage).

Appendix B

Publications

The data presented here has resulted in the following publications:

· M. G. McDowell, R. J. Sanderson, and I. G. Hill. Combinatorial study of zinc tin oxide thin-film transistors. Applied Physics Letters, 92:013502, 2008.

· M. G. McDowell and I. G. Hill. IEEE Transactions on Electron Devices, 56:343347, 2009.

· M. G. McDowell and I. G. Hill. Review of Scientific Instruments, 84:053906, 2013.

Appendix C

Copyright Permissions

AIP PUBLISHING LLC LICENSE
TERMS AND CONDITIONS

Sep 03, 2013

All payments must be made in full to CCC. For payment instructions, please see information listed at the bottom of this form.

License Number	3221651470280
Order Date	Sep 03, 2013
Publisher	AIP Publishing LLC
Publication	Applied Physics Letters
Article Title	Combinatorial study of zinc tin oxide thin-film transistors
Author	M. G. McDowell, R. J. Sanderson, I. G. Hill
Online Publication Date	Jan 2, 2008
Volume number	92
Issue number	1
Type of Use	Thesis/Dissertation
Requestor type	Author (original article)
Format	Print
Portion	Excerpt (> 800 words)
Will you be translating?	No
Title of your thesis / dissertation	A study of the semiconductor and thermoelectric properties of sputtered mixed metal-oxide thin films
Expected completion date	Dec 2013
Estimated size (number of pages)	200
Total	0.00 USD

Terms and Conditions

AIP Publishing LLC -- Terms and Conditions: Permissions Uses

AIP Publishing LLC ("AIPP"") hereby grants to you the non-exclusive right and license to use and/or distribute the Material according to the use specified in your order, on a one-time basis, for the specified term, with a maximum distribution equal to the number that you have ordered. Any links or other content accompanying the Material are not the subject of this license.

1. You agree to include the following copyright and permission notice with the reproduction of the Material:"Reprinted with permission from [FULL CITATION]. Copyright [PUBLICATION YEAR], AIP Publishing LLC." For an article, the copyright and permission notice must be printed on the first page of the article or book chapter. For photographs, covers, or tables, the copyright and permission notice may appear with the Material, in a footnote, or in the reference list.
2. If you have licensed reuse of a figure, photograph, cover, or table, it is your responsibility to ensure that the material is original to AIPP and does not contain the copyright of another entity, and that the copyright notice of the figure, photograph,

cover, or table does not indicate that it was reprinted by AIPP, with permission, from another source. Under no circumstances does AIPP, purport or intend to grant permission to reuse material to which it does not hold copyright.

3. You may not alter or modify the Material in any manner. You may translate the Material into another language only if you have licensed translation rights. You may not use the Material for promotional purposes. AIPP reserves all rights not specifically granted herein.
4. The foregoing license shall not take effect unless and until AIPP or its agent, Copyright Clearance Center, receives the Payment in accordance with Copyright Clearance Center Billing and Payment Terms and Conditions, which are incorporated herein by reference.
5. AIPP or the Copyright Clearance Center may, within two business days of granting this license, revoke the license for any reason whatsoever, with a full refund payable to you. Should you violate the terms of this license at any time, AIPP, AIP Publishing LLC, or Copyright Clearance Center may revoke the license with no refund to you. Notice of such revocation will be made using the contact information provided by you. Failure to receive such notice will not nullify the revocation.
6. AIPP makes no representations or warranties with respect to the Material. You agree to indemnify and hold harmless AIPP, AIP Publishing LLC, and their officers, directors, employees or agents from and against any and all claims arising out of your use of the Material other than as specifically authorized herein.
7. The permission granted herein is personal to you and is not transferable or assignable without the prior written permission of AIPP. This license may not be amended except in a writing signed by the party to be charged.
8. If purchase orders, acknowledgments or check endorsements are issued on any forms containing terms and conditions which are inconsistent with these provisions, such inconsistent terms and conditions shall be of no force and effect. This document, including the CCC Billing and Payment Terms and Conditions, shall be the entire agreement between the parties relating to the subject matter hereof.

This Agreement shall be governed by and construed in accordance with the laws of the State of New York. Both parties hereby submit to the jurisdiction of the courts of New York County for purposes of resolving any disputes that may arise hereunder.

Copyright Clearance Center RightsLink®

Home | Account Info | Help

Title: Influence of Channel Stoichiometry on Zinc Indium Oxide Thin-Film Transistor Performance

Author: McDowell, M.G.; Hill, Ian G.

Publication: Electron Devices, IEEE Transactions on

Publisher: IEEE

Date: Feb. 2009

Copyright © 2009, IEEE

Logged in as:
Matthew McDowell
Account #:
3000692158

LOGOUT

Thesis / Dissertation Reuse

The IEEE does not require individuals working on a thesis to obtain a formal reuse license, however, you may print out this statement to be used as a permission grant:

Requirements to be followed when using any portion (e.g., figure, graph, table, or textual material) of an IEEE copyrighted paper in a thesis:

1) In the case of textual material (e.g., using short quotes or referring to the work within these papers) users must give full credit to the original source (author, paper, publication) followed by the IEEE copyright line © 2011 IEEE.
2) In the case of illustrations or tabular material, we require that the copyright line © [Year of original publication] IEEE appear prominently with each reprinted figure and/or table.
3) If a substantial portion of the original paper is to be used, and if you are not the senior author, also obtain the senior author's approval.

Requirements to be followed when using an entire IEEE copyrighted paper in a thesis:

1) The following IEEE copyright/ credit notice should be placed prominently in the references: © [year of original publication] IEEE. Reprinted, with permission, from [author names, paper title, IEEE publication title, and month/year of publication]
2) Only the accepted version of an IEEE copyrighted paper can be used when posting the paper or your thesis on-line.
3) In placing the thesis on the author's university website, please display the following message in a prominent place on the website: In reference to IEEE copyrighted material which is used with permission in this thesis, the IEEE does not endorse any of [university/educational entity's name goes here]'s products or services. Internal or personal use of this material is permitted. If interested in reprinting/republishing IEEE copyrighted material for advertising or promotional purposes or for creating new collective works for resale or redistribution, please go to http://www.ieee.org/publications_standards/publications/rights/rights_link.html to learn how to obtain a License from RightsLink.

If applicable, University Microfilms and/or ProQuest Library, or the Archives of Canada may supply single copies of the dissertation.

BACK | CLOSE WINDOW

AIP PUBLISHING LLC LICENSE
TERMS AND CONDITIONS

Sep 03, 2013

All payments must be made in full to CCC. For payment instructions, please see information listed at the bottom of this form.

License Number	3221651470280
Order Date	Sep 03, 2013
Publisher	AIP Publishing LLC
Publication	Applied Physics Letters
Article Title	Combinatorial study of zinc tin oxide thin-film transistors
Author	M. G. McDowell, R. J. Sanderson, I. G. Hill
Online Publication Date	Jan 2, 2008
Volume number	92
Issue number	1
Type of Use	Thesis/Dissertation
Requestor type	Author (original article)
Format	Print
Portion	Excerpt (> 800 words)
Will you be translating?	No
Title of your thesis / dissertation	A study of the semiconductor and thermoelectric properties of sputtered mixed metal-oxide thin films
Expected completion date	Dec 2013
Estimated size (number of pages)	200
Total	0.00 USD
Terms and Conditions	

AIP Publishing LLC -- Terms and Conditions: Permissions Uses

AIP Publishing LLC ("AIPP"") hereby grants to you the non-exclusive right and license to use and/or distribute the Material according to the use specified in your order, on a one-time basis, for the specified term, with a maximum distribution equal to the number that you have ordered. Any links or other content accompanying the Material are not the subject of this license.

1. You agree to include the following copyright and permission notice with the reproduction of the Material:"Reprinted with permission from [FULL CITATION]. Copyright [PUBLICATION YEAR], AIP Publishing LLC." For an article, the copyright and permission notice must be printed on the first page of the article or book chapter. For photographs, covers, or tables, the copyright and permission notice may appear with the Material, in a footnote, or in the reference list.
2. If you have licensed reuse of a figure, photograph, cover, or table, it is your responsibility to ensure that the material is original to AIPP and does not contain the copyright of another entity, and that the copyright notice of the figure,

photograph, cover, or table does not indicate that it was reprinted by AIPP, with permission, from another source. Under no circumstances does AIPP, purport or intend to grant permission to reuse material to which it does not hold copyright.

3. You may not alter or modify the Material in any manner. You may translate the Material into another language only if you have licensed translation rights. You may not use the Material for promotional purposes. AIPP reserves all rights not specifically granted herein.
4. The foregoing license shall not take effect unless and until AIPP or its agent, Copyright Clearance Center, receives the Payment in accordance with Copyright Clearance Center Billing and Payment Terms and Conditions, which are incorporated herein by reference.
5. AIPP or the Copyright Clearance Center may, within two business days of granting this license, revoke the license for any reason whatsoever, with a full refund payable to you. Should you violate the terms of this license at any time, AIPP, AIP Publishing LLC, or Copyright Clearance Center may revoke the license with no refund to you. Notice of such revocation will be made using the contact information provided by you. Failure to receive such notice will not nullify the revocation.
6. AIPP makes no representations or warranties with respect to the Material. You agree to indemnify and hold harmless AIPP, AIP Publishing LLC, and their officers, directors, employees or agents from and against any and all claims arising out of your use of the Material other than as specifically authorized herein.
7. The permission granted herein is personal to you and is not transferable or assignable without the prior written permission of AIPP. This license may not be amended except in a writing signed by the party to be charged.
8. If purchase orders, acknowledgments or check endorsements are issued on any forms containing terms and conditions which are inconsistent with these provisions, such inconsistent terms and conditions shall be of no force and effect. This document, including the CCC Billing and Payment Terms and Conditions, shall be the entire agreement between the parties relating to the subject matter hereof.

This Agreement shall be governed by and construed in accordance with the laws of the State of New York. Both parties hereby submit to the jurisdiction of the courts of New York County for purposes of resolving any disputes that may arise hereunder.